

DISSERTATION

IMPROVING RADIATION DATA QUALITY OF USDA UV-B MONITORING AND
RESEARCH PROGRAM AND EVALUATING UV DECOMPOSITION IN DAYCENT AND
ITS ECOLOGICAL IMPACTS

Submitted by

Maosi Chen

Department of Graduate Degree Program in Ecology

In partial fulfillment of the requirements

For the Degree of Doctor of Philosophy

Colorado State University

Fort Collins, Colorado

Fall 2015

Doctoral Committee:

Advisor: Wei Gao

John Davis

John Moore

Rich Conant

Scott Denning

Copyright by Maosi Chen 2015

All Rights Reserved

ABSTRACT

IMPROVING RADIATION DATA QUALITY OF USDA UV-B MONITORING AND RESEARCH PROGRAM AND EVALUATING UV DECOMPOSITION IN DAYCENT AND ITS ECOLOGICAL IMPACTS

Solar radiation impacts many aspects of the Earth's atmosphere and biosphere. The total solar radiation impacts the atmospheric temperature profile and the Earth's surface radiative energy budget. The solar visible (VIS) radiation is the energy source of photosynthesis. The solar ultraviolet (UV) radiation impacts plant's physiology, microbial activities, and human and animal health. Recent studies found that solar UV significantly shifts the mass loss and nitrogen patterns of plant litter decomposition in semi-arid and arid ecosystems. The potential mechanisms include the production of labile materials from direct and indirect photolysis of complex organic matters, the facilitation of microbial decomposition with more labile materials, and the UV inhibition of microbes' population. However, the mechanisms behind UV decomposition and its ecological impacts are still uncertain.

Accurate and reliable ground solar radiation measurements help us better retrieve the atmosphere composition, validate satellite radiation products, and simulate ecosystem processes. Incorporating the UV decomposition into the DayCent biogeochemical model helps to better understand long-term ecological impacts. Improving the accuracy of UV irradiance data is the goal of the first part of this research and examining the importance of UV radiation in the biogeochemical model DayCent is the goal of the second part of the work. Thus, although the

dissertation is separated into two parts, accurate UV irradiance measurement links them in what follows.

In part one of this work the accuracy and reliability of the current operational calibration method for the (UV-) Multi-Filter Rotating Shadowband Radiometer (MFRSR), which is used by the U.S. Department of Agriculture UV-B Monitoring and Research Program (UVMRP), is improved. The UVMRP has monitored solar radiation in the 14 narrowband UV and VIS spectral channels at 37 sites across U.S. since 1992. The improvements in the quality of the data result from an improved cloud screening algorithm that utilizes an iterative rejection of cloudy points based on a decreasing tolerance of unstable optical depth behavior when calibration information is unknown. A MODTRAN radiative transfer model simulation showed the new cloud screening algorithm was capable of screening cloudy points while retaining clear-sky points. The comparison results showed that the cloud-free points determined by the new cloud screening algorithm generated significantly (56%) more and unbiased Langley offset voltages (V_{LOS}) for both partly cloudy days and sunny days at two testing sites, Hawaii and Florida. The V_{LOS} are proportional to the radiometric sensitivity.

The stability of the calibration is also improved by the development of a two-stage reference channel calibration method for collocated UV-MFRSR and MFRSR instruments. Special channels where aerosol is the only contributor to total optical depth (TOD) variation (e.g. 368-nm channel) were selected and the radiative transfer model (MODTRAN) used to calculate direct normal and diffuse horizontal ratios which were used to evaluate the stability of TOD in cloud-free points. The spectral dependence of atmospheric constituents' optical properties and previously calibrated channels were used to find stable TOD points and perform Langley calibration at spectrally adjacent channels. The test of this method on the UV-B program site at

Homestead, Florida (FL02) showed that the new method generated more clustered and abundant V_{LOS} at all (UV-) MFRSR channels and potentially improved the accuracy by 2-4% at most channels and over 10% at 300-nm and 305-nm channels.

In the second major part of this work, I calibrated the DayCent-UV model with ecosystem variables (e.g. soil water, live biomass), allowed maximum photodecay rate to vary with litter's initial lignin fraction in the model, and validated the optimized model with LIDET observation of remaining carbon and nitrogen at three semi-arid sites. I also explored the ecological impacts of UV decomposition with the optimized DayCent-UV model. The DayCent-UV model showed significant better performance compared to models without UV decomposition in simulating the observed linear carbon loss pattern and the persistent net nitrogen mineralization in the 10-year LIDET experiment at the three sites. The DayCent-UV equilibrium model runs showed that UV decomposition increased aboveground and belowground plant production, surface net nitrogen mineralization, and surface litter nitrogen pool, while decreased surface litter carbon, soil net nitrogen mineralization and mineral soil carbon and nitrogen. In addition, UV decomposition showed minimal impacts (i.e. less than 1% change) on trace gases emission and biotic decomposition rates.

Overall, my dissertation provided a comprehensive solution to improve the calibration accuracy and reliability of MFRSR and therefore the quality of radiation products. My dissertation also improved the understanding of UV decomposition and its long-term ecological impacts.

ACKNOWLEDGEMENTS

I would like to express my special appreciation to my advisor Dr. Wei Gao for his guidance and supports. He encourages me to grow as a research scientist. His advice on both research as well as life is invaluable.

I would like to thank Dr. John M. Davis. I consider him as my co-advisor. He introduced me to the field of radiation transfer and patiently helped me at every stage of my research.

I would like to thank Dr. John C. Moore, Dr. Richard Conant, and Dr. Scott Denning for serving as my committee members. I also want to thank them for their brilliant comments and suggestions.

I would like to thank Dr. William J. Parton and his group (Melannie, Cynthia, and Susan) for introducing me to the DayCent modeling world. He gave me tremendous help at the critical stage of my research.

I would like to thank my master advisor Dr. Zhiqiang Gao for encouraging me to pursue my Ph.D. at Colorado State University.

I would like to thank all UVB program staff, Rita, George, Michael, Zhibin, Becky, Shinichi, Jonathan, and Scott for their helps.

I would like to thank NREL and GDPE for their supports.

Finally, I would like to thank my parents, other family members, and friends for their supports and helps.

TABLE OF CONTENTS

ABSTRACT.....	ii
ACKNOWLEDGEMENTS.....	v
TABLE OF CONTENTS.....	vi
INTRODUCTION	1
CHAPTER 1 : THE CALIBRATION METHODS FOR MULTI-FILTER ROTATING SHADOWBAND RADIOMETER: A REVIEW	14
CHAPTER 2 : A NEW CLOUD SCREENING ALGORITHM FOR GROUND-BASED DIRECT-BEAM SOLAR RADIATION	51
CHAPTER 3 : TWO-STAGE REFERENCE CHANNEL CALIBRATION FOR COLLOCATED UV AND VIS MULTI-FILTER ROTATING SHADOWBAND RADIOMETERS	82
CHAPTER 4 : ASSESSING ECOLOGICAL IMPACTS OF UV LITTER DECOMPOSITION USING DAYCENT	114
CONCLUSIONS.....	183

INTRODUCTION

Solar radiation passing through the Earth's atmosphere is reflected, absorbed, and scattered by atmospheric constituents (such as clouds, aerosols, water vapor, trace gases, and other molecules) and the Earth's surface. Therefore, solar radiation impacts the atmospheric temperature profile as well as the Earth's and surface radiative energy budget (Ramanathan et al. 1989). Furthermore, solar radiation reaching the Earth's surface fuels many ecosystem processes. Solar visible (VIS) radiation, especially photosynthetically active radiation (PAR), is the energy source of plants' photosynthesis (Monteith and Unsworth 2008). Solar UV radiation inhibits microbial activities (Caldwell et al. 2007) and impacts live plants' leaf area, respiration, water-use efficiency, Nitrogen fixation, production (yield accumulation), morphogenesis, and secondary metabolites (Gehrke et al. 1995; Rozema et al. 1997; Zepp et al. 1998; Reddy et al. 2013; Kakani et al. 2003a, 2003b; Formánek et al. 2014). In addition, exposure to high solar UV radiation (especially in the UV-B region) has adverse impacts on human and animal health (Caldwell et al. 1986; Madronich 1993; Teramura et al. 1990).

Traditional litter decomposition models focus on the roles of microbes on decomposition. These models use climate variables (precipitation and temperature) and litter quality variables (carbon/nitrogen and lignin/nitrogen ratios) to predict litter mass loss rates (Parton et al. 2007; Gallo et al. 2009). However, many studies in dry and hot terrestrial ecosystems (Austin and Vivanco 2006; Day et al. 2007; Rutledge et al. 2010) and in aquatic ecosystems (Kieber et al. 1989; Miller and Zepp 1995; Anesio et al. 1999) found that the decomposition of plant litter or dissolved organic matter is faster than the expectation of traditional models. Furthermore, decomposing surface litter does not immobilize nitrogen and the decomposition rate is unrelated

to initial nitrogen contents in some arid ecosystems (Parton et al. 2007; Brandt et al. 2010). These patterns suggest that abiotic processes (such as UV decomposition) rather than microbial activity are the major drivers of decomposition in those ecosystems (Brandt et al. 2010). The mechanistic detail of photodegradation remains uncertain. It is reported that solar (UV) radiation may directly photolyze a molecule through fragmentation, intramolecular rearrangement, or electron transfer (King et al. 2012; Lee et al. 2012) and indirectly photolyze a non-light-absorbing molecule by promoting the production of reactive intermediates (George et al. 2005; Messenger et al. 2009; Cory et al. 2010; Feng et al. 2011; King et al. 2012). However, uncertainties exist on the specific carbon compounds that are affected by photodegradation, with some evidence for higher loss rates for either cellulosic or lignin pools (Rozema et al. 1997; King et al. 2012). It is also reported that solar UV radiation indirectly influences decomposition by providing microbes more labile material from photodegradation (Austin and Vivanco 2006; Gallo et al. 2006; Henry et al. 2008) and from leaching fats and lipids by breaking down cell walls (Vähätalo et al. 1998; Day et al. 2007; Lin and King 2014), inhibiting microbial population (Gehrke et al. 1995; Zepp et al. 1998; Moody et al. 1999), and altering microbial community composition (Moorhead and Callaghan, 1994; Gallo et al. 2006). Adair et al. (2015) developed and calibrated a three-C-pool decomposition model that simulates both biotic decomposition and photodegradation of litter. Their model selection results supported flows related to UV radiation induced direct photolysis, facilitation effects, and microbial inhibition effects. Since decomposition of plant litter and soil organic matter is a key process that influences the balance of carbon and nitrogen between the atmosphere and biosphere (Adair et al. 2008; Harmon et al. 2011) in arid and semi-arid areas which cover more than 30% of land surface and are expanding

(Brandt et al. 2009; Austin 2011), it is important to explore the mechanisms of UV decomposition, incorporate them into models, and assess their ecological impacts.

It is important that we get accurate and reliable ground solar radiation measurements because the accuracy of solar radiation measurement is critical for retrieving atmospheric constituents (Leontieva and Stamnes 1996; Kiedron et al. 1999; Michalsky et al. 2001; Alexandrov et al. 2002b, 2009; di Sarra et al., 2008; Mazzola et al. 2010; Kassianov et al. 2011; Yin et al. 2011), validating satellite radiation products (Wielicki et al. 1995), and evaluating ecosystem impacts caused by solar radiation.

The UV-B Monitoring and Research Program (the UV-B program) is a data collection and research program of the United States Department of Agriculture (USDA). The UV-B program is comprised of two unique components: 1) a ground-based solar (UV) radiation monitoring network; and 2) an integrated assessment system that studies interactions between climate stress factors (including UV radiation) and ecosystems (<http://uvb.nrel.colostate.edu>).

The UV-B program has been measuring solar ultraviolet (UV) and visible (VIS) radiation across U.S. since 1992 (Bigelow et al. 1998). It utilizes UV and VIS versions of the Multi-Filter Rotating Shadowband Radiometer (MFRSR) to observe direct normal, diffuse, and total hemispheric solar radiation at 7 UV channels (300, 305, 311, 317, 325, 332, 368 nm) with 2-nm full bandwidth at half maximum (FWHM) and at 7 VIS channels (unfiltered, 415, 500, 610, 665, 870, 940 nm) with 10-nm FWHM bandwidth (Bigelow et al. 1998). The measured voltages are converted to irradiances with the responsivity coefficients obtained via laboratory lamp calibration or in-situ calibration. Although routine lamp calibrations for the entire UV-B network are desirable, the annual comparison with National Institute of Standards and Technology radiation sources has become cost prohibitive. Therefore, the UV-B program currently uses the

Langley method as the main technique for calibration of the instruments while a more limited number still receive lamp calibrations at the Central UV Calibration Facility (CUCF) at NOAA in Boulder, CO. There are two major problems with the current Langley computer program (hereafter referred to as the Langley Analyzer.) The first problem is that the original cloud screening algorithm in the Langley Analyzer shows poor performance at some sites and no alternative algorithm is available. The original cloud screening module compares measurements' voltages in local windows. This strategy only works when there are extended clear-sky periods. For sites typified by periods of broken cloudiness, it will miss clear-sky points in short intervals as well as in transitional periods between cloudy and clear conditions. As a result, there may not be sufficient data to perform Langley calibration; or some cloud points are passed to calibration and result in severely biased calibration coefficients. Most cloud screening algorithms available are designed for calibrated radiation values (e.g. Long and Ackerman 2000; Augustine et al. 2003) and their derived products (such as aerosol optical depth) (Smirnov et al. 2000; Alexandrov et al. 2004; Mazzola et al. 2010). Some methods require collocated ancillary measurements, such as total-sky imagers (di Sarra et al. 2008) and aerosol optical depth such as provided by the AERONET program (Krotkov et al. 2005). Although some of them show good performance, they cannot be utilized by the UV-B program to screen voltage measurements before calibration. The second problem is that the stability assumption of total optical depth (TOD) is hard to meet at most UV-B program sites because aerosol optical depth (Augustine et al. 2003) or optical depth of other atmospheric constituents may have systematic variation of AOD over the course of a calibration period (Alexandrov et al. 2002). As a result, the Langley regression gives biased calibration coefficients. There have been some studies that recognized this issue and proposed alternative assumptions to mitigate the problem. For example, instead of

requiring the stable total optical depth, the general method (Forgan 1994) only requires that the aerosol extinction efficiency as well as the particle radius and the refraction index to be stable and allows the aerosol abundance to vary with time. These are less strict requirements, however, they are not always reliable especially when aerosol properties change. Besides, they only apply to the special channels where no gaseous absorption contributes significantly to TOD variation. The Ratio-Langley method (Forgan, 1986) assumes that the TOD difference between two channels where gaseous absorption is negligible are more likely to be stable. This assumption shows a similar problem as the original Langley assumption: the TOD difference may also have systematic variation over time leading to biased ratio of calibration coefficients.

Accurate UV irradiance data is the single entity linking the two topics of this dissertation—the product of one topic and the input of the other, but otherwise the methodologies of the two topics are entirely separable. Thus they are treated as such in the description of the work that follows. The dissertation is separated into two parts, each focusing on one topic mentioned above.

In the first part (Part I, Chapter 1-3), my objective is to improve the accuracy and reliability of the current operational calibration method for (UV)-MFRSR. The objective is fulfilled by following steps:

(1) developing a new cloud screening algorithm for voltage measurements that screens cloudy (high TOD) points but retains most clear-sky points in the transitional region and in short time windows; and

(2) Finding practical strategies that ensure the critical TOD stability assumption of the Langley method without additional measurements.

In the second part (Part II, Chapter 4), my objective is to modify and validate the UV decomposition module of the DayCent biogeochemical model and to explore the potential long-term impacts of UV decomposition on ecosystem processes in semi-arid ecosystems, such as plant production, carbon and nitrogen storage in litter and soil, and trace gas emissions.

REFERENCES

- Adair E C, Parton W J, King J Y, Brandt L, Harmon M E (2015), Accounting for photodegradation dramatically improves prediction of carbon and nitrogen losses in arid systems. (In prep.)
- Alexandrov M D, Lacis A A, Carlson B E, Cairns B (2002), Remote sensing of atmospheric aerosols and trace gases by means of multi-filter rotating shadowband radiometer. part I: retrieval algorithm. *J Atmos Sci*, 59(3): 524–543. doi:10.1175/1520-0469(2002)059<0524:RSOAAA>2.0.CO;2
- Alexandrov M D, Lacis A A, Carlson B E, Cairns B (2002b), Remote sensing of atmospheric aerosols and trace gases by means of multi-filter rotating shadowband radiometer. part II: climatological applications. *J Atmos Sci*, 59(3): 544–566. doi:10.1175/1520-0469(2002)059<0544:RSOAAA>2.0.CO;2
- Alexandrov M D, Marshak A, Cairns B, Lacis A A, Carlson B E (2004), Automated cloud screening algorithm for MFRSR data. *Geophys Res Lett*, 31(4): L04118. doi:10.1029/2003GL019105
- Alexandrov M D, Schmid B, Turner D D, Cairns B, Oinas V, Lacis A A, Gutman S I, Westwater E R, Smirnov A, Eilers J (2009), Columnar water vapor retrievals from multifilter rotating shadowband radiometer data. *J Geophys Res*, 114(D2): D02306. doi:10.1029/2008JD010543
- Anesio A M, Tranvik L J, Graneli W (1999), Production of inorganic carbon from aquatic macrophytes by solar radiation. *Ecology*, 80(6): 1852-1859. doi: 10.1890/0012-9658(1999)080[1852:POICFA]2.0.CO;2
- Augustine J A, Cornwall C R, Hodges G B, Long C N, Medina C I, DeLuisi J J (2003), An automated method of MFRSR calibration for aerosol optical depth analysis with application to an Asian dust outbreak over the United States. *J Appl Meteorol*, 42(2): 266–278. doi:10.1175/1520-0450(2003)042<0266:AAMOMC>2.0.CO;2
- Austin A T (2011), Has water limited our imagination for aridland biogeochemistry? *Trends in Ecology and Evolution*, 26(5): 229-235. doi: 10.1016/j.tree.2011.02.003
- Austin A T, Vivanco L (2006), Plant litter decomposition in a semi-arid ecosystem controlled by photodegradation. *Nature*, 442(7102): 555-558. doi: 10.1038/nature05038
- Bigelow D S, Slusser J R, Beaubien A F, Gibson J H (1998), The USDA Ultraviolet Radiation Monitoring Program. *Bulletin of the American Meteorological Society*, 79(4): 601-615. doi: 10.1175/1520-0477(1998)079<0601:TUURMP>2.0.CO;2

- Brandt L A, Bohnet C, King J Y (2009), Photochemically induced carbon dioxide production as a mechanism for carbon loss from plant litter in arid ecosystems. *Journal of Geophysical Research*, 114: G02004. doi: 10.1029/2008JG000772
- Brandt L A, King, J Y, Hobbie S E, Milchunas D G, Sinsabaugh R L (2010), The Role of Photodegradation in Surface Litter Decomposition Across a Grassland Ecosystem Precipitation Gradient. *Ecosystems*, 13(5): 765-781. doi: 10.1007/S10021-010-935
- Caldwell M M, Camp C W, Warner C W, Flint S D (1986), Action spectra and their role in assessing biological consequences of solar UV-B radiation change. In: Worrest R C, Caldwell M M, eds. *Stratospheric Ozone Reduction, Solar Ultraviolet Radiation and Plant Life*. Berlin: Springer-Verlag, 87–111
- Caldwell M M, Bornman J F, Ballare C L, Flint S D, Kulandaivelu G (2007), Terrestrial ecosystems, increased solar ultraviolet radiation, and interactions with both climate change factors. *Photochemical & Photobiological Sciences*, 6(3): 252-266. doi: 10.1039/b700019g
- Cory R M, McNeill K, Cotner J P, Amado A, Purcell J M, Marshall A G (2010), Singlet Oxygen in the Coupled Photochemical and Biochemical Oxidation of Dissolved Organic Matter. *Environmental Science & Technology*, 44(10): 3683-3689. DOI: 10.1021/es902989y
- Day T A, Zhang E T, Ruhland C T (2007), Exposure to solar UV-B radiation accelerates mass and lignin loss of *Larrea tridentata* litter in the Sonoran Desert. *Plant Ecology*, 193(2): 185-194. doi: 10.1007/s11258-006-9257-6
- di Sarra A, Fua D, Cacciani M, Di Iorio T, Disterhoft P, Meloni D, Monteleone F, Piacentino S, Sferlazzo D (2008), Determination of ultraviolet cosine-corrected irradiances and aerosol optical thickness by combined measurements with a Brewer spectrophotometer and a multifilter rotating shadowband radiometer. *Appl Opt*, 47(33): 6142–6150. doi:10.1364/AO.47.006142
- Feng X, Hills K M, Simpson A J, Whalen J K, Simpson M J (2011), the role of biodegradation and photo-oxidation in the transformation of terrigenous organic matter. *Organic Geochemistry*, 42(3): 262-274. doi: 10.1016/j.orggeochem.2011.01.002
- Forgan B W (1986), Sun photometer calibration by the ratio-Langley technique. In: Forgan B W, Fraser P J, eds. *Baseline Atmospheric Program*, Bureau of Meteorology, Melbourne, Australia, 22–26
- Forgan B W (1994), General method for calibrating Sun photometers. *Appl Opt*, 33(21): 4841–4850. doi:10.1364/AO.33.004841
- Formánek P, Rejšek K, Vranová V (2014), Effect of Elevated CO₂, O₃, and UV Radiation on Soils. *Scientific World Journal*, 2014: 730149. doi: 10.1155/2014/730149

- Gallo M E, Porras-Alfaro A, Odenbach K J, Sinsabaugh R L (2009), Photoacceleration of plant litter decomposition in an arid environment. *Soil Biology & Biochemistry*, 41(7): 1433-1441. doi: 10.1016/j.soilbio.2009.03.025
- Gallo M E, Sinsabaugh R L, Cabaniss S E (2006), The role of ultraviolet radiation in litter decomposition in arid ecosystems. *Applied Soil Ecology*, 34(1): 82-91. doi: 10.1016/j.apsoil.2005.12.006
- Gehrke C, Johanson U, Callaghan T V, Chadwick D, Robinson C H (1995), The Impact of Enhanced Ultraviolet-B Radiation on Litter Quality and Decomposition Processes in Vaccinium Leaves from the Subarctic. *Oikos*, 72(2): 213-222. doi: 10.2307/3546223
- George B, Suttie E, Merlin A, Deglise X (2005), Photodegradation and photostabilisation of wood – the state of the art. *Polymer Degradation and Stability*, 88(2): 268-274. doi: 10.1016/j.polymdegradstab.2004.10.018
- Harmon M E, Bond-Lamberty B, Tang J, Vargas R (2011), Heterotrophic respiration in disturbed forests: A review with examples from North America, *J. Geophys. Res.*, 116: G00K04. doi:10.1029/2010JG001495
- Henry H A L, Brizgys K, Field C B (2008), Litter decomposition in a california annual grassland: Interactions between photodegradation and litter layer thickness. *Ecosystems*, 11(4): 545-554. doi: 10.1007/s10021-008-9141-4
- Kakani V G, Reddy K R, Zhao D, Mohammed A R (2003b), Effects of ultraviolet-B radiation on cotton (*Gossypium hirsutum* L.) morphology and anatomy. *Ann Bot (Lond)*, 91(7): 817–826. doi:10.1093/aob/mcg086
- Kakani V G, Reddy K R, Zhao D, Sailaja K (2003a), Field crop responses to ultraviolet-B radiation: a review. *Agric Meteorol*, 120(1–4): 191–218. doi:10.1016/j.agrformet.2003.08.015
- Kassianov E, Barnard J C, Berg L K, Flynn C, Long C N (2011), Sky cover from MFRSR observations. *Atmos. Meas. Tech.*, 4: 1463–1470, doi:10.5194/amt-4-1463-2011.
- Kieber D J, McDaniel J, Mopper K (1989), Photochemical source of biological substrates in sea water: implications for carbon cycling. *Nature*, 341(6243): 637-639. doi: 10.1038/341637a0
- Kiedron P W, Michalsky J J, Berndt J L, Harrison L C (1999), Comparison of spectral irradiance standards used to calibrate shortwave radiometers and spectroradiometers. *Appl Opt*, 38(12): 2432–2439. doi:10.1364/AO.38.002432
- King J Y, Brandt L A, Adair E C (2012), Shedding light on plant litter decomposition: Advances, implications and new directions in understanding the role of photodegradation. *Biogeochemistry*, 111(1-3): 57-81. doi: 10.1007/s10533-012-9737-9

- Krotkov N, Bhartia P K, Herman J, Slusser J, Labow G, Scott G, Janson G, Eck T F, Holben B (2005), Aerosol ultraviolet absorption experiment (2002 to 2004), part 1: ultraviolet multifilter rotating shadowband radiometer calibration and intercomparison with CIMEL sunphotometers. *Opt Eng*, 44(4): 041004. doi:10.1117/1.1886818
- Lee H, Rahn T, Throop H (2012), An accounting of C-based trace gas release during abiotic plant litter degradation. *Global Change Biology*, 18(3): 1185–1195. doi: 10.1111/j.1365-2486.2011.02579.x
- Leontieva E, Stamnes K (1996), Remote Sensing of Cloud Optical Properties from Ground-Based Measurements of Transmittance: A Feasibility Study. *J Appl Meteor*, 35(11): 2011–2022
- Lin Y, King J Y (2014), Effects of UV Exposure and Litter Position on Decomposition in a California Grassland. *Ecosystems*, 17(1): 158-168. doi: 10.1007/s10021-013-9712-x
- Long C N, Ackerman T P (2000), Identification of clear skies from broadband pyranometer measurements and calculation of downwelling shortwave cloud effects. *J Geophys Res*, 105(D12): 15609–15626. doi:10.1029/2000JD900077
- Madronich S (1993), UV radiation in the natural and perturbed atmosphere. In: Tevini M, ed., *UV-B Radiation and Ozone Depletion: Effects on Humans, Animals, Plants, Microorganisms, and Materials*. Lewis Publishers, Boca Raton, Florida, 17-69
- Mazzola M, Lanconelli C, Lupi A, Busetto M, Vitale V, Tomasi C (2010), Columnar aerosol optical properties in the Po Valley, Italy, from MFRSR data. *J Geophys Res*, 115(D17): D17206. doi:10.1029/2009JD013310
- Messenger D J, Mcleod A R, Fry S C (2009), The role of ultraviolet radiation, photosensitizers, reactive oxygen species and ester groups in mechanisms of methane formation from pectin. *Plant, Cell & Environment*, 32(1): 1–9. doi: 10.1111/j.1365-3040.2008.01892.x
- Michalsky J J, Schlemmer F A, Berkheiser W E, Berndt J L, Harrison L C, Laulainen N S, Larson N R, Barnard J C (2001), Multi-year measurements of aerosol optical depth in the Atmospheric Radiation Measurement and Quantitative Links programs. *J Geophys Res*, 106(D11): 12099–12107. doi:10.1029/2001JD900096
- Miller W L, Zepp R G (1995), Photochemical production of dissolved inorganic carbon from terrestrial organic-matter - significance to the oceanic organic-carbon cycle. *GEOPHYSICAL RESEARCH LETTERS*, 22(4): 417-420. doi: 10.1029/94GL03344
- Monteith J L, Unsworth M H (2008), *Principles of environmental physics*, 3rd ed. Oxford: Academic
- Moody S A, Paul N D, Bjorn L O, Callaghan T V, Lee J A, Manetas Y, Rozema J, Gwynn-Jones D, Johanson U, Kyparissis A, Oudejans A M C (2001), The direct effects of UV-B radiation on *Betula pubescens* litter decomposing at four European field sites. *Plant Ecology*, 154,(1-2): 27-36. doi: 10.1023/A:1012965610170

- Moorhead D L, Callaghan T (1994), Effects of increasing ultraviolet B radiation on decomposition and soil organic matter dynamics: a synthesis and modelling study. *Biology and Fertility of Soils*, 18(1): 19-26. doi: 10.1007/BF00336439
- Parton W, Silver W L, Burke I C, Grassens L, Harmon M E, Currie W S, King J Y, Adair E C, Brandt L A, Hart S C, Fash B (2007), Global-Scale Similarities in Nitrogen Release Patterns During Long-Term Decomposition. *Science*, 315(5810): 361–364. doi: 10.1126/science.1134853
- Ramanathan V, Cess R D, Harrison E F, Minnis P, Barkstrom B R, Ahmad E, Hartmann D (1989), Cloud-radiative forcing and climate: results from the Earth radiation budget experiment. *Science*, 243(4887): 57–63. doi:10.1126/science.243.4887.57
- Reddy K R, Singh S K, Koti S, Kakani V G, Zhao D, Gao W, Reddy V R (2013), Quantifying the Effects of Corn Growth and Physiological Responses to Ultraviolet-B Radiation for Modeling. *Agronomy journal*, 105(5): 1367-1377. doi: 10.2134/agronj2013.0113
- Rozema J, Tosserams M, Nelissen H, van Heerwaarden L, Broekman R A, Flierman N (1997), Stratospheric ozone reduction and ecosystem processes: Enhanced UV-B radiation affects chemical quality and decomposition of leaves of the dune grassland species *calamagrostis epigeios*. *Plant Ecology*, 128(1-2): 285-294. doi: 10.1023/A:1009723210062
- Rutledge S, Campbell D I, Baldocchi D, Schipper L A (2010), Photodegradation leads to increased carbon dioxide losses from terrestrial organic matter. *Global Change Biology*, 16(11): 3065–3074. doi: 10.1111/j.1365-2486.2009.02149.x
- Smirnov A, Holben B N, Eck T F, Dubovik O, Slutsker I (2000), Cloud screening and quality control algorithms for the AERONET database. *Remote Sens. Environ.*, 73(3): 337-349. doi: 10.1016/S0034-4257(00)00109-7
- Teramura A H, Sullivan J H, Ziska L H (1990), Interaction of Elevated Ultraviolet-B Radiation and CO₂ on Productivity and Photosynthetic Characteristics in Wheat, Rice, and Soybean. *Plant Physiol*, 94(2): 470–475. doi:10.1104/pp.94.2.470
- Vähätalo A, Søndergaard M, Schlüter L, Markager S (1998), Impact of solar radiation on the decomposition of detrital leaves of eelgrass *Zostera marina*. *Marine Ecology Progress Series*, 170: 107-117. doi: 10.3354/meps170107
- Wielicki B A, Cess R D, King M D, Randall D A, Harrison E F (1995), Mission to Planet Earth: role of clouds and radiation in climate. *Bull Am Meteorol Soc*, 76: 2125–2153
- Yin B, Min Q, Duan M, Bartholomew M J, Vogelmann A M, Turner D D (2011), Retrievals of cloud optical depth and effective radius from Thin-Cloud Rotating Shadowband Radiometer measurements. *J Geophys Res*, 116(D23): D23208. doi:10.1029/2011JD016192

Zepp R G, Callaghan T V, Erickson D J (1998), Effects of enhanced solar ultraviolet radiation on biogeochemical cycles. *Journal of Photochemistry and Photobiology B: Biology*, 46(1–3): 69-82. doi: 10.1016/S1011-1344(98)00186-9

Part I: Improving in-situ calibration accuracy and reliability of (UV) Multi-Filter Rotating
Shadowband Radiometer measurements

CHAPTER 1: THE CALIBRATION METHODS FOR MULTI-FILTER ROTATING SHADOWBAND RADIOMETER: A REVIEW¹

Introduction

Climate change has received more and more concern in the last few decades. The amount and distribution variation of gaseous and particle components in the Earth's atmosphere that alter the radiative forcing balance are believed to be the main cause of such change. In the Intergovernmental Panel on Climate Change (IPCC) report (AR4), water vapor is considered the most important greenhouse gas (positive radiative forcing), and carbon dioxide (CO₂) is the second-most important one. Trace gases such as methane, nitrous oxide, ozone, and several others also contribute to the greenhouse effect. Although water vapor has positive radiative forcing, Ramanathan et al. (1989) found that clouds had a net global cooling effect on the earth based on the radiative forcing data from the spaceborne Earth Radiation Budget Experiment (ERBE). The contribution of aerosols to overall radiative forcing is significant as well, although the effect is highly variable due to high uncertainty of the mean aerosol radiative forcing (Feister et al. 2007). Charlson et al. (1992) showed that aerosol particles can scatter short wavelength solar radiation and modify the shortwave reflective properties of clouds, which lead to increased planetary albedo and have cooling effects on the planet. The magnitude of the global average of

¹ This chapter includes the complete published manuscript (minimal modifications were made to meet formatting requirements):

Chen M, Davis J, Tang H, Ownby C, Gao W (2013), The calibration methods for Multi-Filter Rotating Shadowband Radiometer: A review. *Frontiers of Earth Science*, 7(3): 257–270.

doi:10.1007/s11707-013-0368-9.

The link to the published article is <http://link.springer.com/article/10.1007/s11707-013-0368-9>.

The final publication is available at link.springer.com

the aerosol radiative forcing is comparable to that of anthropogenic greenhouse gas forcing but opposite in sign. However, the different geographical and temporal distribution of these forcings precludes any simple compensation. Ramanathan et al. (2001) concluded that increased albedo caused by aerosols leads to large reductions of solar irradiance reaching the Earth's surface, changing the atmospheric temperature profile and the pattern of rainfall.

In addition to the changing temperature profile effect of climate change, the change in shortwave solar irradiance reaching the Earth's surface because of variation in clouds, gases, and aerosols in the atmosphere is also significant. Surface radiative energy budget studies must know the effect of clouds and other interference on shortwave irradiance (Long and Ackerman 2000). Solar radiation in the visible region is the driving force for photosynthesis (Monteith and Unsworth 2008), while that in the ultraviolet region (especially in the UV-B section) is considered an adverse condition for vegetation growth and crop yield accumulation (Kakani et al. 2003a, 2003b) and human and animal health (Caldwell et al. 1986; Madronich 1993; Teramura et al. 1990). Both solar irradiance and aerosols have direct impact on human health (Lighty et al. 2000). Aerosols also impact surface visibility conditions, as radiation reflected from aerosol particulates contributes to direct irradiance (Chow et al. 1994).

In the annual report of the Atmospheric Radiation Measurement (ARM) Climate Research Facility (FY 2011, <http://www.arm.gov/publications/annual-reports/docs/doe-sc-arm-11-024.pdf?id=94>), it is concluded that global climate models (GCMs) are one of the primary tools for simulating climate change. These models require knowledge of clouds and aerosols, and their effects on the Earth's energy balance. Remote sensing of solar radiation (ground-based, airborne, or satellite-based) is widely used for retrieving properties of these parameters. The validation of satellite retrieval algorithms for surface irradiance requires accurate surface

measurement (Wielicki et al. 1995). Ground based sun photometric measurement can also be used to produce aerosol, ozone, UV radiation, precipitable water vapor, and cloud climatology (Leontieva and Stamnes 1996; Kiedron et al. 1999; Michalsky et al. 2001a; Alexandrov et al. 2002b, 2009; di Sarra et al. 2008; Mazzola et al. 2010; Kassianov et al. 2011; Yin et al. 2011). There are various types of instruments that provide sun photometric measurements, for example: (i) CIMEL sun radiometers, which are the key instruments at Aerosol Robotic Network (AERONET) (Holben et al. 1998) sites; and (ii) Multi-Filter Rotating Shadowband Radiometers (MFRSR) (Alexandrov et al. 2008). An advantage of the MFRSR is that it can be operated automatically and its cost is relatively low, making the construction of networks for distributed data collection feasible. The growing international deployment of the MFRSR makes it a potentially important tool for climate research (Alexandrov et al. 2002).

Except for the direct/diffuse and total/diffuse MFRSR component ratios which cancel out the dependency on absolute calibration (Kaskaoutis et al. 2008), the successful application of MFRSR measurements relies on stable and accurate calibration, which converts the instrument reading to actual radiation, and gives the angular correction and spectral response function. The calibration parameters determined before deployment can shift dramatically and quickly in the field, which requires frequent recalibration (laboratory or in situ) to produce reliable radiation measurements.

In this paper, we present a description of the ultraviolet and visible versions of MFRSR instrument, its data collection, and issues related to the challenge of calibration. We review the published calibration efforts, including both laboratory lamp and in situ calibration methods.

The UV- and VIS- MFRSR

The VIS-MFRSR (Figure 1.1) is the visible version of the MFRSR. It is environmentally sealed and thermally stabilized at around 40°C, and uses state-of-the-art interference filter photodiode detectors (http://uvb.nrel.colostate.edu/UVB/ins_vismfrsr.jsf). It contains six narrowband channels (415, 500, 615, 673, 870, and 940 nm), each with a 10 nm full-width at half maximum (FWHM) bandwidth (http://uvb.nrel.colostate.edu/UVB/ins_vismfrsr.jsf). The seventh channel is an unfiltered silicon (Si) photodiode responsive to 300–1040 nm (http://uvb.nrel.colostate.edu/UVB/ins_vismfrsr.jsf).

The UV-MFRSR is the ultraviolet version of the MFRSR. It is environmentally sealed and thermally stabilized at around 42°C, and uses seven state-of-the-art interference filter photodiode detectors (center wavelengths at 300, 305, 311, 317, 325, 332, and 368 nm), each with a 2 nm FWHM bandwidth (Bigelow et al. 1998; http://uvb.nrel.colostate.edu/UVB/ins_uvmfrsr.jsf). The 300 and 305 channels use silicon-carbide (SiC) photodiodes, and the 311 through 368 channels use silicon (Si) photodiodes (http://uvb.nrel.colostate.edu/UVB/ins_uvmfrsr.jsf).

According to Alexandrov et al. (2008), the programs that are running MFRSR networks in the United States include the USDA UV-B Monitoring and Research Program (UVMRP) (Bigelow et al. 1998), the DOE Atmospheric Radiation Measurement (ARM) Program (Ackerman and Stokes 2003), the NOAA Surface Radiation (SURFRAD) Network (Augustine et al. 2005), and the NASA Solar Irradiance Research Network (SIRN).

The basic geometry of the MFRSR can be seen in Figure 1.1 and Figure 1.2.

The shadow-band is an arched metal strip that blocks a strip of sky with an umbral angle (Z_p) of 3.27°, which is more than sufficient to block the solar disk (Harrison et al. 1994b). A

self-contained microprocessor calculates the solar position by using an approximation for the solar ephemeris, which controls the rotation of the shadow-band to certain positions. The stepping precision and error may limit accuracy to $\pm 0.3^\circ$. After the instrument is installed at a site, a onetime adjustment for latitude and azimuth alignment to the Earth's pole is performed.

Unlike a sun photometer, the MFRSR doesn't measure the direct beam irradiance directly. Instead, the MFRSR derives the direct beam from its principal measurements. To collect one data record, a set of four measurements are taken (Hodges and Michalsky 2011):

(1) The initial measurement (total horizontal, t_{hor}) is taken when the shadow-band is in the home position (Figure 1.1 Nadir/home position);

(2) The first of two side-band measurements (first side band, fsb) is taken when the shadow-band is 9° off the sun blocking direction (Figure 1.1: Two additional measurements compensate for sky blocked during shaded measurement);

(3) The sun-blocked measurement (blk) is taken (Figure 1.1: Blocked measurement made with band shading diffuser);

(4) The second of two side-band measurements (second side band, ssb) is taken when the shadow-band is 9° off the sun blocking direction (the other side of the step (2), Figure 1.1: Two additional measurements compensate for sky blocked during shaded measurement).

These four measurements are made every 20 s (15 s for UV-MFRSR) and averaged into 3-min intervals for the USDA UVMRP, and 2-min intervals for the SURFRAD network.

Dark current bias removal (offset correction)

Extraneous voltages that are not the result of radiation incidence but the inherent noise of the instrument should be removed (Bigelow et al. 1998; Hodges and Michalsky 2011). Under

normal operations, the nighttime data (voltages measured one hour prior to and one hour after the time of minimum solar elevation over a three-day period preceding the current data processing day) are averaged to estimate this offset, which is subtracted from all the measurements in the daytime before any further calculation.

The measurements of steps (2) and (4) permit a first-order correction for the excess sky blocked by the shadow-band for the step (3) measurement. The diffuse horizontal (*dif_hor*) is expressed as

$$dif_hor = blk + [t_hor - (fsb + ssb) / 2] \quad (1.1)$$

The direct horizontal (*dir_hor*) is expressed as

$$dir_hor = t_hor - dif_hor \quad (1.2)$$

Cosine response correction

Radiation incident on a flat horizontal surface originating from a point source with a defined zenith position will have an intensity value proportional to the cosine of the zenith angle of incidence. When the sun is directly overhead, the theoretical cosine correction is one. This is called the cosine-response. Ideally, spectroradiometers are designed to have a directional response which is exactly the same as the cosine-response. However, the actual instruments rarely match this ideal (Feister et al. 1997; Michalsky et al. 1995; Seckmeyer and Bernhard, 1993). The magnitude of this discrepancy (known as cosine error) can vary from a few percent to 10% or 20%, depending on the atmospheric conditions (i.e. cloudiness and aerosol optical depth (Feister et al. 1997)) and the characteristics of the system (Blumthaler and Bais 1996; Bais 1997; Bais et al. 1998). The cosine correction table, which considers errors regarding both the azimuth angle and zenith angle of incidence, is provided for each MFRSR by the manufacturer or the

calibration laboratory. With this table, one obtains the cosine corrected direct (*cor_dir_hor*) and diffuse (*cor_dif_hor*) horizontals:

$$\begin{aligned} cor_dif_hor &= dif_hor / (diffuse\ cosine\ correction) \\ cor_dir_hor &= dir_hor / (direct\ cosine\ correction) \end{aligned} \quad (1.3)$$

The cosine corrected total horizontal (*cor_t_hor*) is the sum of these two values:

$$cor_t_hor = cor_dif_hor + cor_dir_hor \quad (1.4)$$

Now, the direct normal (*dir_norm*) is calculated as:

$$dir_norm = cor_dir_hor / \cos \theta \quad (1.5)$$

where, the θ is the zenith angle of incidence or solar zenith angle.

The measurements or derived quantities in Eqs. (1.1) to (1.5) are voltages. The conversion of voltage to irradiance requires a calibration factor (*c*):

$$I_\lambda = V_\lambda / c_\lambda \quad (1.6)$$

where, λ represents the MFRSR channel or effective wavelength.

Laboratory lamp calibration

Major tasks of laboratory lamp calibration

There are many facilities that provide laboratory calibration, such as the Central UV Calibration Facility (CUCF), NOAA, Boulder, Colorado; Yankee Environmental Systems (YES), Inc.; and the Atmospheric Radiation Measurement Program (ARM) Southern Great Plains (SGP) Central Facility (CF). Generally, laboratory calibration includes three important tasks:

(1) Standard lamp calibration, which determines the calibration factor c_λ for each channel;

(2) Angular response determination, which generates angular correction tables; and
(3) Spectral Response Function (SRF) of each filter detector (channel) determination, which is also known as the filter function.

The second and third tasks can only be determined via lamp calibration, while the first part can also be determined via in situ calibration methods or via calibration of a reference instrument, which is the method AERONET uses to routinely calibrate its sun photometers.

Limitations of laboratory calibration

Hickey (1970) and Booth et al. (1994) found that the difference between the solar and lamp spectra is not negligible when working with moderate bandwidth radiometers (i.e. UV-MFRSR). A solution to this problem is introducing a calibration constant that references both the lamps and solar spectra (Booth et al. 1994). However, applying this method for routine network calibration requires the circulation of the field instrument to be collocated with the reference spectroradiometer for an adequate period while the gaps in the monitoring record at each site are minimized, which is hard to sustain (Bigelow et al. 1998). Alexandrov et al. (2009) emphasizes that MFRSR filters may experience rapid sensitivity loss; i.e. Alexandrov et al. (2002) reported the loss of filter transmittance approximately by a factor of 3 for two MFRSR channels during the first 200 days of instrument operation, followed by gradual stabilization.

Augustine et al. (2003) pointed out that periodic calibration throughout the year is necessary because the extraterrestrial signal will slowly change due to filter drift.

In situ calibration

Langley method

The attenuation of the Sun's direct beam irradiance through the Earth's atmosphere can be described by the Bouguer-Lambert law (Beer's law, Slusser et al. 2000):

$$I_{\lambda} = R^2 I_{0,\lambda} \exp(-\tau_{Total,\lambda} \cdot m) \quad (1.7)$$

where I_{λ} is the band-pass direct normal irradiance reaching surface at channel λ . R is the ratio of the mean and instantaneous distances of the earth from the sun.

$I_{0,\lambda} = \int I_{0,\lambda_t} F_{\lambda_t} d\lambda_t / \int F_{\lambda_t} d\lambda_t$ is the normalized band-pass extraterrestrial solar irradiance at channel λ , where F_{λ_t} is the filter function, or SRF, of the channel λ at wavelength λ_t and I_{0,λ_t} is the corresponding extraterrestrial solar irradiance (Slusser et al. 2000).

There are many sources that provide I_{0,λ_t} of various spectral resolutions; one of them is the Atmospheric Laboratory for Applications and Science (ATLAS) mission with the Solar Spectral Irradiance Measurements (SOLSPEC) spectrometer (Thuillier et al. 1998). Molling et al. (2010) pointed out that $I_{0,\lambda}$ can change by as much as 0.2% over a few days, depending on sunspot activity. From 1978 to 2002, solar input at the top of atmosphere increased at a rate of 0.05% per decade (Willson and Mordvinov 2003). Schmid et al. (1998) compared the uncertainty of several $I_{0,\lambda}$ and determined that since the uncertainty due to atmospheric conditions is at least one magnitude larger, it is acceptable that one considers $I_{0,\lambda}$ as a constant and known value for calibration.

The band-pass total optical depth at channel λ is $\tau_{Total,\lambda}$, and m is the airmass. In Slusser et al. (2000), Wilson and Forgan (1995), and Schmid and Wehrli (1995), the term $(\tau_{Total,\lambda})(m)$ is

described as the sum of the optical depth of each scatterer or absorber and the corresponding airmass: $\sum_i (\tau_{i,\lambda})(m_i)$, where i indicates the i th scatterer or absorber. It is noted that m_i can vary slightly for different scatterers and absorbers (i.e. ozone, air molecules, and aerosols) due to their different altitude concentration profiles (Thomason et al. 1983). The airmass m is defined as the ratio of the path length of solar radiation incident at zenith angle z and the zenith path length. For solar zenith angles up to 75° , $m \approx 1 / \cos(z)$ is accurate enough. For higher solar zenith angles, more accurate approximation equations should be used (Kasten and Young 1989).

For each MFRSR channel λ , the calibration factor can also be expressed as (Bigelow et al. 1998):

$$c_\lambda = V_{0,\lambda} / I_{0,\lambda} \quad (1.8)$$

where, $V_{0,\lambda}$ is the corresponding voltage measured by the MFRSR as if it is deployed at the top of the atmosphere (airmass = 0). Applying Eqs. (1.8) and (1.6) to Eq. (1.7), they get

$$V_\lambda = R^2 V_{0,\lambda} \exp(-\tau_{Total,\lambda} \cdot m) \quad (1.9)$$

Taking the natural logarithm on both sides of Eq. (1.9),

$$\ln(V_\lambda / R^2) = \ln V_{0,\lambda} - \tau_{Total,\lambda} \cdot m \quad (1.10)$$

For each direct beam measurement at channel λ , there are two unknown terms: $\ln V_{0,\lambda}$ and $\tau_{Total,\lambda}$. Generally, one equation with two unknowns does not have a definite solution. The Langley method introduces an additional constraint to solve these two unknown variables: the total optical depth is stable during the morning or afternoon calibration period (Bigelow et al. 1998). With this additional constraint, $\ln V_{0,\lambda}$ and $\tau_{Total,\lambda}$ may be solved simultaneously with a linear regression where $\ln V_{0,\lambda}$ is the intercept and $\tau_{Total,\lambda}$ is the negative of the slope (Bigelow et

al. 1998). Note that cloudy measurements should be removed before one performs this linear regression. The subsection below will discuss the cloud screening methods.

Two corrections for UV Langley regression (Slusser et al. 2000)

For the visible channels, only the variation of aerosol optical depth may significantly affect the performance of the Langley regression (Slusser et al. 2000). In UV channels, especially channels under 320 nm, the ozone cross section changes rapidly with wavelength. The finite band-pass correction factor is defined as the ratio of the surface direct beam irradiance at the wavelength of the peak of the filter function and the band-pass surface direct beam irradiance (Slusser et al. 2000). Slusser et al. (2000) used the Tropospheric Ultraviolet & Visible Radiation Model (TUV, <https://www2.acom.ucar.edu/modeling/tropospheric-ultraviolet-and-visible-tuv-radiation-model>) to calculate the irradiances for the finite band-pass correction factor. The TUV model uses parameters airmass range [1.2, 2.2] and total column ozone, 300 DU.

The other correction factor accounts for the difference between ozone airmass and the molecular airmass (Slusser et al. 2000). Komhyr (1980) described the calculation details of ozone and molecular airmass. Instead of the correction factor, one can do the Langley regression using the reduced or weighted airmass, $m_{red} = \sum m_i \cdot \tau_i / \sum \tau_i$, described by Forgan (1988) to eliminate the airmass effects (Slusser et al. 2000).

Janson and Slusser (2003) reported that the mean annual drifts in sensitivity for the seven nominal wavelengths of the UV-MFRSR instrument are: 300nm – 0.9%, 305nm – 3.5%, 311nm – 3.5%, 317nm – 4.3%, 325nm – 3.8%, 332nm – 3.7%, 368nm – 3.5%.

The choice of airmass range

The reasons for limiting of airmass to a certain range include: (i) The uncertainty of the cosine angle correction and the shadow-band correction of MFRSR at high incident angles is increased (Mazzola et al. 2010; Alexandrov et al. 2004); (ii) High solar zenith angles have higher chances of cloud contamination due to a decreased probability gap for vertically developed clouds (Smirnov et al. 2000); (iii) Airmass near 1 usually indicates a higher probability of turbulent atmospheric conditions, which is not optimal for the AOD stability assumption of the Langley method.

This choice of airmass range is not unique. Mazzola et al. (2010) and Alexandrov et al. (2004) selected the 2.0 to 5.0 range; Harrison and Michalsky (1994) chose the 2.0 to 6.0 range; and Forgan (1994) used the 2.5 to 5.5 range.

Cloud screening

Beer's law requires that no clouds are in the path of the direct solar beam. Clouds can attenuate the direct solar irradiance, or, if near the solar disk, contribute to more diffuse solar radiation.

di Sarra et al. (2008) identified cloud-free periods using images from the Total Sky Imager, visual observations of the sky, and data from the broadband channel of the MFRSR.

It is possible for one to perform manual selection of data points presenting the clear sky and radiatively stable conditions (Augustine et al. 2003). Mazzola et al. (2010) pointed out that screening the cloudy points using the visual examination is time-consuming and cannot be applied routinely. Alexandrov et al. (2004) commented that the results of manual screening depended on the skill of the examiner.

The cloud screening module of the Langley Analyzer (LA) is a set of filters on the series of $\ln V$ – airmass points. The following description is based on the interpolation of the C source code of the LA program. In the UVMRP version of LA, points with voltage less than $0.02V$ are discarded. The user can specify the points that fall into permissible airmass ranges (i.e. [2.0, 6.0]). The rest points in the desired airmass ranges are referred to as the permissible points hereafter. The permissible points within a morning/afternoon are first sorted by airmass in ascending order. The detection of cloud periods is implemented by searching for segments with the beginning points where $\ln V$ starts to increase and the ending points where $\ln V$ starts to decrease again in that series. Additionally, concavity in the series is checked by setting thresholds on the slope of $\ln V$. To test this algorithm for more than a half day, the algorithm should be applied to the data of each half day and the returned clear sky points combined into one vector.

The cloud screening algorithm developed by Long and Ackerman (2000) is originally designed for irradiance series provided by calibrated pyranometers, which are broadband radiometers with an effective 160° field of view centered on the zenith. The screening process is iterative, with each step involving four tests. The first test sets maximum and minimum limits of the airmass normalized downwelling total shortwave irradiance to eliminate obvious cloudy points. The second test sets maximum limits of the airmass normalized downwelling diffuse irradiance to eliminate haze or thin cloud points. The third test eliminates points that have a change of irradiance in a given time outside of a certain range. The fourth test checks the variation in the measurements by using a normalized diffuse ratio. The points that pass these four tests are tentatively clear-sky points and are used to adjust the threshold values for the next

iteration. When two consecutive iteration steps return the same set of points, the iteration stops and those points are the final clear-sky points.

Augustine et al. (2003) applied the cloud screening algorithm of Long and Ackerman (2000) to the SURFRAD broadband solar data in a two month period. They used the determined clear-sky periods for Langley calibration of the 500 nm channel of the collocated MFRSR because they believed that the noise was reduced and a confident extrapolation to $\ln V_0$ by simple linear regression was feasible. The example (Fig. 3 in (Augustine et al. 2003)) shows that the regression line passes the majority of the screened points. Many MFRSR networks do not have broadband solar data to do the cloud screening, which limits its application to automatic calibration of MFRSR in those programs.

The cloud screening method of Mazzola et al. (2010) “renormalizes” AODs to a common range by: (i) 10 min AOD average is subtracted from each instantaneous AOD value; (ii) add the typical value of AOD (namely 0.2) to step 1 results; (iii) calculate the relative standard deviation of step 2 results over each 10 min period; (iv) label the points from step 3 with a value greater than 0.08 as cloudy points.

Smirnov et al. (2000) developed an automatic cloud screening algorithm on the time series of aerosol optical depth derived from calibrated sunphotometers of AERONET. First, the data quality is checked. The points with negative values of AOD (< -0.01) or values lower than the stratospheric background AOD (Shaw 1982) (varying with wavelength) are identified as cloudy or poor quality. Second, the triplet stability criterion is applied. The three measurements, each made 30 s apart, constitute a triplet. The points with AOD range in a triplet exceeding $\text{Max}\{0.02, 0.03 \cdot \text{AOD}\}$ are identified as cloudy. The empirical threshold value for any wavelength is 0.02 when AOD is lower than 0.7. When the AOD level is high (> 0.7 , indicating

biomass burning or extremely hazy conditions, etc.), the threshold value is relaxed to be $0.03 \times \text{AOD}$. Third, the diurnal stability is checked. The points with a standard deviation of AOD at 500 nm (or 440 nm) for the entire day that is larger than 0.015 are identified as cloudy. Fourth, the smoothness criteria are applied. It is assumed that the second derivative of the time series of optical depth is very sensitive to that caused by nearby cloudy points. To ensure a coherent threshold value, they designed the logarithmic second derivative (D) of optical depth:

$$D = \sqrt{\frac{1}{(n-2)} \sum \left[\frac{\ln \tau_i - \ln \tau_{i+1}}{t_i - t_{i+1}} - \frac{\ln \tau_{i+1} - \ln \tau_{i+2}}{t_{i+1} - t_{i+2}} \right]^2} \quad (1.11)$$

They recursively removed the points with maximum optical depth until $D \leq 16$. Then they applied the diurnal stability check again and repeated the third and fourth steps until no elimination occurred. Fifth, the $3\text{-}\sigma$ criterion is applied. Any points that are outside of the $3\text{-}\sigma$ range of the mean AOD at 500 nm or Angstrom coefficient α (440–870 nm) are identified as cloudy.

Based on the variability analysis of derived optical depth, Alexandrov et al. (2004) developed an automated cloud screening algorithm using single channel direct beam measurements of a VIS-MFRSR. Their algorithm is based on the inhomogeneity parameter (ε) (Cahalan 1994; Cairns et al. 2000):

$$\varepsilon = 1 - \frac{\exp(\overline{\ln \tau})}{\bar{\tau}} \quad (1.12)$$

where the over-line refers to averaging over time. The inhomogeneity parameter, ε , can vary from 0 for completely homogeneous to 1 for extremely inhomogeneous air conditions (Alexandrov et al. 2004). To better separate aerosols and some types of clouds [thin cirrus, marine boundary layer clouds (Alexandrov et al. 2004)], ε is modified as:

$$\varepsilon' = 1 - \frac{\exp(\overline{\ln \tau'})}{\overline{\tau'}} \quad (1.13)$$

where $\tau' = \tau - \bar{\tau} + \tau_{const}$ is the renormalized optical depth. The statistical distribution of values of the inhomogeneity parameter ε' over a month shows two distinctive maxima that correspond to the aerosol and cloud modes respectively (Alexandrov et al. 2004). Aerosols have a lower ε' than clouds. The threshold value of ε' between the two modes is $2 \cdot 10^{-4}$, below which are considered clear and above which are considered cloudy. It is noted that this approach can misidentify a very short clear sky interval between clouds as being cloudy (Alexandrov et al. 2004), although the probability of this situation is small.

Reasons for the failure of the Langley method [summarized by (Augustine et al. 2003)]

(1) A change in aerosol optical depth over the course of a calibration period (Augustine et al. 2003). The assumption of AOD stability is critical to the Langley method, for which Forgan (1986) made a sensitivity analysis: A change in aerosol optical depth of 0.003 will produce an error of about 1 percent in the calibration coefficient (Augustine et al. 2003). For a 368 nm channel, a change of absolute aerosol optical depth at 0.003 represents less than 0.6% change in optical depth. But the observed percent change of a typical sea-level station is between 3% and 10% (Augustine et al. 2003). Wilson and Forgan (1995) mentioned methods to overcome the limitations that are due to atmospheric variability; all involve information that is not commonly available for a long-term operational MFRSR such as deployment of another calibrated instrument or knowing calibration information in a certain channel (Augustine et al. 2003).

(2) Effects of atmospheric noise such as that from subvisual cirrus (Shaw 1976, Augustine et al. 2003). Thin clouds may have optical depth as low as aerosols. However, Beer's

law is not valid for cloudy conditions, which means including such points in a Langley regression may significantly bias the regression intercept ($\ln V_0$) (Augustine et al. 2003).

(3) Instrument errors. This covers some complicated situations. For example, the internal temperature of the MFRSR is supposed to be maintained constantly at around 40°C or 42°C; however, in summer at some southern sites, the actual internal temperature can be 10°C higher than the defined constant near noon (Augustine et al. 2003). The diurnal variation of voltages due to this factor can result in a biased intercept ($\ln V_0$) (Augustine et al. 2003). Alexandrov et al. (2007) mentioned that the precision of instrument alignment should be considered. The AOD errors induced by a 1° tilt are on the order of 0.01.

(4) Harrison et al. (1994b) report that the relatively large field of view of an MFRSR makes it vulnerable to the adverse effects of enhanced forward scattering by aerosols or thin cirrus cloud particles whose dimensions are large compared to the wavelength of the measurement (Augustine et al. 2003).

Two variants of Langley method

On-site calibration technique: Krotkov et al. (2005) calculate V_0 (325, 332, and 368 nm channels) of UV-MFRSR using Beer's law with all components of optical depth prepared before calibration. Total column ozone is obtained from climatological mean ozone values, aerosol optical depth is extrapolated / interpolated in both wavelength and temporal dimensions from AERONET-CIMEL measurements, and Rayleigh optical depth is calculated using the method by Bodhaine et al. (1999). Extraterrestrial spectral solar irradiance is taken from SUSIM AtLAS-3 measurements. There is only one unknown variable in Eq. (1.10): V_0 , which can be calculated for each time point. The daily mean V_0 is calculated by iteratively removing points outside of three

times the standard deviation. The stability of this method is about $\pm 2\%$ in summer and larger in fall-winter seasons. This method requires accurate aerosol optical depth availability before calibration, which limits its application in most MFRSR sites.

The main modification Lee et al. (2010) proposed to the standard Langley method involves the acquisition of the maximum value composite (MVC) of the largest irradiance (voltage) values during a several day window in each small airmass interval. The abnormal values are eliminated by applying a threshold on the standard deviation of relative difference in each bin. The window sizes vary from 5 to 30 days. The comparison of the derived AOD using this method to the interpolated AOD of AERONET showed that the relative error of AOD for 5, 7, and 10 days are about 20% and equal to 7.5% for 30 days.

Ratio-Langley method (Forgan 1986)

Forgan (1986) pointed out that the variation of aerosol optical depth by changes of particle number, the aerosol size distribution, or both, affects all channels at different degrees depending on the optical efficiency as a function of particle size and wavelength.

In the two channels (λ_1 and λ_2) where gaseous absorption is negligible or constant with time, they found that the difference of total optical depth between them ($\tau_1(t) - \tau_2(t)$) is the combination of a constant (dominated by molecular scattering and absorption) and a varying term caused by aerosols (Forgan 1986). Dividing the Beer's Law equations at λ_1 and λ_2 , and taking a logarithm on both sides, they got the following equation:

$$\ln\left(\frac{V_1(t)}{V_2(t)}\right) = \ln\left(\frac{V_{01}}{V_{02}}\right) - (\tau_1(t) - \tau_2(t)) \cdot m(t) \quad (1.14)$$

Their sensitivity analysis on the Angstrom exponential formula showed that for aerosol distributions dominated by large particles (i.e. marine environments), $|\tau_{a1}(t) - \tau_{a2}(t)| \rightarrow 0$, which suggests that a Langley-like regression on Eq. (1.14) will give a more accurate and stable intercept term V_{01} / V_{02} (Forgan 1986).

Strictly speaking, the ratio-Langley method alone cannot provide calibration coefficients for any individual channel. Instead, it provides the ratio of calibration coefficients at two channels (V_{01} / V_{02}). If the calibration coefficient at one channel is determined by other means, all calibration coefficients can be calculated using the ratio results (Forgan 1986).

General method (Forgan 1994)

The fundamental assumptions of the general method are that the relative size distribution f is dependent only on particle radius r and the multiplier A is only a function of time t (Forgan 1994). With these assumptions, the aerosol size distribution can be expressed as $\partial N(t) / \partial \ln r = A(t) f(r)$ (Forgan 1994). The aerosol optical depth (τ_a) for this distribution at time t and wavelength λ is given by (Forgan 1994)

$$\tau_a(t, \lambda) = \pi A(t) \int Q_{ext}(r, \lambda) r^2 f(r) d \ln r \quad (1.15)$$

where Q_{ext} is the extinction efficiency, which is a function of the wavelength and the particle radius. It is seen that the only term in this expression that is dependent on time is the multiplier A . Therefore, the optical depth at any time t can be related to that at the reference time t_0 , $\tau_a(t, \lambda) = \tau_a(t_0, \lambda) A(t) / A(t_0)$ (Forgan 1994). The ratio of optical depths at any time t between two wavelengths (λ_0 and λ_1) is a constant (defined as ψ_{01} , Forgan 1994):

$$\begin{aligned}\frac{\tau_a(t, \lambda_1)}{\tau_a(t, \lambda_0)} &= \frac{\tau_a(t_0, \lambda_1)A(t) / A(t_0)}{\tau_a(t_0, \lambda_0)A(t) / A(t_0)} \\ &= \frac{\tau_a(t_0, \lambda_1)}{\tau_a(t_0, \lambda_0)} = \text{const} \tan t = \psi_{01}\end{aligned}\quad (1.16)$$

for all t .

If the Beer-Lambert's law is valid on both wavelengths, one can derive the logarithm of the calibration factor of the target wavelength ($-\ln V_{0-1}$) and the constant (ψ_{01}) through a least squares regression on the following expression (Forgan 1994):

$$\begin{aligned}\left\{ -\left[\ln V_1(t) + m_m(t)\tau_m(t, \lambda_1) + m_g\tau_g(t, \lambda_1) \right] \right\} = \\ \psi_{01} \left[m_a(t)\tau_a(t, \lambda_0) \right] + \left\{ -\ln V_{0-1} \right\}\end{aligned}\quad (1.17)$$

The three terms on the left side of the equal sign are measurements ($V_1(t)$) or calculable values (airmass, molecular scattering, and absorption optical depths). There are two ways of providing the aerosol optical depth at the other wavelength $[m_a(t)\tau_a(t, \lambda_0)]$: (i) using a well-calibrated sun photometer; or (ii) using solar Aureole Measurements (Forgan 1987; Forgan 1994).

Comprehensive calibration with atmospheric quantities retrieval (Alexandrov et al. 2002)

This method provides for the simultaneous determination of the instrument's calibration coefficients together with the retrieval of physical quantities (Alexandrov et al. 2002). This method is designed for 5 channels (415–870 nm) of VIS-MFRSR. The basic equation used is Beer's law. The major improvement of this method is that it relaxes the strong assumption of stability of aerosol optical depth to that of aerosol spectral extinction properties during the calibration period (determined by composition and particle size distribution) (Alexandrov et al.

2002). This method does not require any additional measurements from other instruments. Depending on the wavelength, the significant components of the total optical depth may include Rayleigh, aerosol, nitrogen dioxide, and ozone. There are several methods for approximating the Rayleigh optical depth with comparable results (Hansen and Travis 1974; Bucholtz 1995; Bodhaine et al. 1999). They remove it to get the adjusted total optical depth. They manually select clear-sky points. There are four main steps of this method:

(1) The first step of the retrieval algorithm is the determination of the 870 nm optical depth and calibration coefficient.

The reason for the choice of 870 nm channel is that diffuse flux is only affected by aerosols, which means the vertical distribution of gaseous absorbers (nitrogen dioxide and ozone) can be unknown (Alexandrov et al. 2002).

The direct to diffuse irradiance ratio from the same MFRSR is independent of instrumental calibration. The retrieval of optical depth from direct-diffuse ratio relies on the simplified analytical relationship (Alexandrov et al. 2002):

$$A = \frac{1}{R} \left(\frac{1 - (\Phi / \Phi_0)}{1 + \Phi \cdot \cos \theta} \right) \quad (1.18)$$

where A is the surface albedo; $\Phi = I_{dir} / I_{dif} = V_{dir} / V_{dif}$ is the corresponding direct-diffuse ratio; and Φ_0 is the zero surface reflectivity. The scattering angle integrated reflection function, R , can be seen as an implicit function of optical depth (Alexandrov et al. 2002). The retrieved aerosol optical depth depends only weakly on surface albedo, so although the surface albedo is an unknown quantity, a reasonable assumption of low surface albedo ($< 50\%$) results in the uncertainty of ± 0.01 in the optical depth inverted from Eq. (1.18) (Alexandrov et al. 2002). This

calibration procedure works well even for days with highly variable optical depth (Alexandrov et al. 2002).

(2) The second step is an analytical solution of a set of linear equations to retrieve aerosol optical properties.

The assumption is that the aerosol spectral extinction Q_{ext}^i is more stable while the aerosol optical depth is changing systematically during the day (Alexandrov et al. 2002). Starting from Beer's law, Alexandrov et al. (2002) defined the un-calibrated optical depth for the i th channel as

$$\tau_i = -\mu \cdot \ln \frac{V_i}{V_0} = \tau_i + s_i \cdot \mu \quad (1.19)$$

where $s_i = -\ln c_i$ and c_i is the calibration coefficient for channel i ; $\tau_i = q_i \tau_a + \beta_i x_{NO_2} + \gamma_i x_{O_3}$ is the total optical depth for channel i ; $q_i = Q_{ext}^i / Q_{ext}^5$ is the Mie-scattering extinction ratio normalized to the fifth (870 nm) channel (Alexandrov et al. 2002). q_5 is equal to 1, all other q_i are unknown but assumed to be invariant over the calibration period; τ_a is the aerosol optical depth of channel 5; β_i and γ_i are the effective spectral absorption coefficients for nitrogen dioxide and ozone, respectively, for channel i : $\gamma_1 = 0, \gamma_5 = 0, \beta_5 = 0$, all others are measured values from previous studies; x_{NO_2} and x_{O_3} are the column nitrogen dioxide and column ozone in Dobson units, respectively; and μ is the cosine of the solar zenith angle (Alexandrov et al. 2002). From step (1), one already has s_5 and τ_a . Substituting them into Eq. (1.19), they obtain the following equations:

$$\begin{aligned} F_3 &= B_3(x - s_5) + A_3 \\ F_4 &= B_4(x - s_5) + A_4 \end{aligned} \quad (1.20)$$

where,

$$x = \mu^{-1} \cdot \tau_5 \quad (1.21)$$

$$F_i = \mu^{-1} \left[\tau_i - b_{i1} \tau_1 - g_{i2} (\tau_2 - b_{21} \tau_1) \right] \quad (1.22)$$

$$B_i = q_i - b_{i1} q_1 - g_{i2} (q_2 - b_{21} q_1) \quad (1.23)$$

$$A_i = s_i - b_{i1} s_1 - g_{i2} (s_2 - b_{21} s_1) \quad (1.24)$$

where, $i \in [3, 4]$; $b_{ij} = \beta_i / \beta_j$ and $g_{ij} = \gamma_i / \gamma_j$ are the spectrally weighted nitrogen dioxide and ozone absorption coefficient ratios, which can be treated as known values, respectively (Alexandrov et al. 2002). In Eq. (1.20), the calculation of the left-hand side, Eq. (1.22), at each time step only involves measurements and known values (Alexandrov et al. 2002). On the right-hand side, x and s_5 are measurements and retrieved value; both B_i and A_i are unknown but constant over the calibration period since the calibration factors s_i and the aerosol extinction ratios q_i are expected to be constant over the period (Alexandrov et al. 2002). Therefore, one can retrieve the unknowns (B_3 , B_4 , A_3 , and A_4) in Eq. (1.20) with a linear regression similar to Langley regression.

The two aerosol size distribution parameters, the effective radius r_{eff} and the effective variance ν_{eff} , are used to build a look-up table for B_3 and B_4 via Eq. (1.23) and Mie theory (Alexandrov et al. 2002). The combination of r_{eff} and ν_{eff} that matches the regression results of B_3 and B_4 are the solutions. To reduce the influence of error in measurements and calibrations, they limit ν_{eff} to a small value to average out the oscillations and the corresponding r_{eff} is referred to as “monodistribution radius” (Alexandrov et al. 2002). Now only B_3 is needed to

retrieve r_{eff} , which is considered to generate more stable result than B_4 . Once r_{eff} is determined, the aerosol optical depth, at any wavelength, can be calculated from the Mie spectral extinction parameter and τ_a (Alexandrov et al. 2002).

(3) The third step is the retrieval of the nitrogen dioxide and ozone column amounts, as well as the first two channel calibration coefficients.

The aerosol optical depths retrieved from step (2) are removed from Eq. (1.19). Since $\gamma_1 = 0$, the unknown optical depth left for channel 1 (415 nm) is due to nitrogen dioxide.

Assuming the stability of nitrogen dioxide over the calibration period, one can solve s_1 and the average column nitrogen dioxide (x_{NO_2}) together with regression (Alexandrov et al. 2002).

By removing the aerosol and nitrogen dioxide optical depth from Eq. (1.19), one can solve s_2 and the column ozone (x_{O_3}) together with regression on channel 2 (Alexandrov et al. 2002).

(4) The fourth step is the determination of the calibration coefficients for the rest of the channels.

The last two calibration coefficients, s_3 and s_4 , can be calculated using Eq. (1.24); s_1 and s_2 are retrieved in step (3) (Alexandrov et al. 2002).

Nonlinear optimization with Bi-channel Langley and Angstrom law constraints

The calibration method of Chen et al. (2012) relies on two essential constraints: (i) the AOD difference between channels is constant over time, which is fulfilled by the bi-channel Langley method; and (ii) the AOD ratio between channels is constant over time, which is implemented by the Angstrom law. The technique “bi-channel Langley method” is similar to the

“ratio-Langley method” described in the previous section. These constraints are applied in two consecutive optimization steps to solve the calibration factors (V_0) and AOD in the target channels using the trust region based nonlinear optimization module called CONDOR (Vanden Berghen and Bersini 2005). Two channels are the minimum requirement for this method, while multiple channels in the 368 to 870 nm range can be solved simultaneously with this method. The example shows better agreement of AOD derived from this method than that of the standard Langley method to the collocated AERONET AOD, which implies improvement in the retrieved calibration factors. Note that Angstrom law is empirical and may not be suitable for some cases, which limits its application.

Water vapor channel calibration

Alexandrov et al. (2009) reviewed the papers that describe the retrieval of precipitable water vapor (and determination of calibration factors in some papers) using ground based radiometers at 940 nm channel: Fowle (1912, 1915), Reagan et al. (1987b, 1995), Thome et al. (1992, 1994), Michalsky et al. (1995b, 2001b), Schmid et al. (1996, 2001, 2003), Shiobara et al. (1996), Halthore et al. (1997), Cachorro et al. (1998), Plana-Fattori et al. (1998, 2004), Ingold et al. (2000), Kiedron et al. (2003), Livingston et al. (2007).

The calibration methods for the 940 nm channel can be characterized by the “Modified Langley plot” fitting technique (Reagan et al. 1987a; Bruegge et al. 1992; Alexandrov et al. 2009).

The transmission of water vapor (T_{water}) is modeled as a function of the water vapor column (u) (Michalsky et al. 1995b, 2001b),

$$T_{water} = \exp\left(-k \cdot (m \cdot u)^b\right) \quad (1.25)$$

where k and b are constants for a particular filter. For the purpose of determining k and b , m is set to 1. Rearranging the terms (Michalsky et al. 1995b, 2001b),

$$\ln\left(\ln\left(1/T_{water}\right)\right) = \ln k + b \cdot \ln(u) \quad (1.26)$$

One can calculate the effective transmission of water vapor (convolution of the normalized SRF and the atmospheric transmission of water vapor over wavelength of the filter pass-band) as a function of u using a radiative transfer model (Michalsky et al. 1995b). Once the expected range of u is covered, one can perform a least squares fit to Eq. (1.26) to obtain k and b for the particular filter/instrument (Michalsky et al. 1995b).

Beer's law for the 940 nm channel considers the water vapor absorption,

$$V_{940} = R^2 V_{0,940} \exp\left(-\left(\tau_{aerosol,940} + \tau_{Rayleigh,940}\right) \cdot m\right) \cdot T_{water} \quad (1.27)$$

Taking the natural logarithm of Eq. (1.27) and rearranging it (Michalsky et al. 1995b),

$$\ln\left(V_{940}/R^2\right) + \left(\tau_{aerosol,940} + \tau_{Rayleigh,940}\right) \cdot m = \ln\left(V_{0,940}\right) - \left(k \cdot m^b\right) \cdot u^b \quad (1.28)$$

The calculation of $\tau_{Rayleigh}$ at any given wavelength has been discussed (Bodhaine et al. 1999). The value of $\tau_{aerosol,940}$ may be estimated by extrapolating on the $\log \tau_{aerosol} - \log \lambda$ plot (Krotkov et al. 2005). Similar to the Langley method, assuming the water vapor column remains constant in the calibration period, one can perform a linear regression on Eq. (1.28) to determine the intercept, $\ln\left(V_{0,940}\right)$, and the slope, u^b , simultaneously (Michalsky et al. 1995b).

Alexandrov et al. (2009) found that the fundamental assumption of this technique: the stability of the precipitable water vapor (PWV) column, which is similar to that of the standard Langley method, rarely occurs in reality, except for very dry sites like the Arctic (Kiedron et al. 2001) or high mountains (Schmid et al. 1998). In other cases this technique cannot provide accurate calibration factors or PWV with low uncertainty (Michalsky et al. 2001b). Because of

this, research that involves a 940 nm channel usually uses lamp calibration instead of this technique (Alexandrov et al. 2009; Hodges and Michalsky 2011).

Conclusions

The MFRSR, both the visible and ultraviolet versions, is a widely deployed radiometer that has measured surface shortwave radiation with high sampling rate for about two decades. It has been used for validating satellite observation and retrievals and for monitoring important properties of gases, aerosols, and clouds in the atmosphere. Except for the parameters that can be derived from the ratio of its measured components, which are not impacted by calibration error, most applications require accurate calibration factors, angular correction, and spectral response functions provided by calibration. Although the laboratory lamp, or reference, calibration can provide all the information needed to convert the readings to actual radiation, in situ calibration methods are implemented routinely to fill the gaps between lamp calibrations. In situ calibration with collocated AOD measurements can provide accurate calibration factors. However, information of AOD is not available for most deployed MFRSR units, which limits its application. In situ calibration methods based on Beer's law with no ancillary AOD measurements are fundamentally underdetermined problems. They assume some properties, such as AOD, TOD, precipitable water vapor, effective size of aerosol particles, and angstrom coefficient, are invariant over time in order to create equations solvable by linear regression or nonlinear optimization. Since these artificial assumptions are not universal and some of them rarely happen, there is no single in situ calibration method that is suitable for all sites at all times. In practice, daily calibration factors derived from these methods should be time-smoothed with or without lamp calibration information to restrain error.

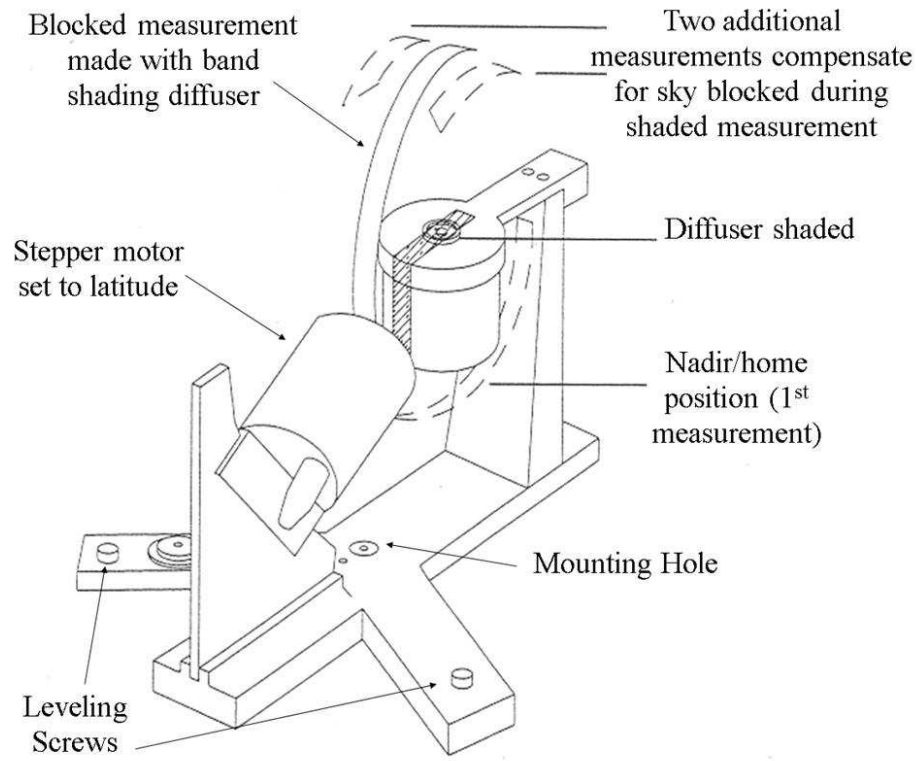


Figure 1.1 Basic geometry of a MFRSR (Hodges and Michalsky, 2011)

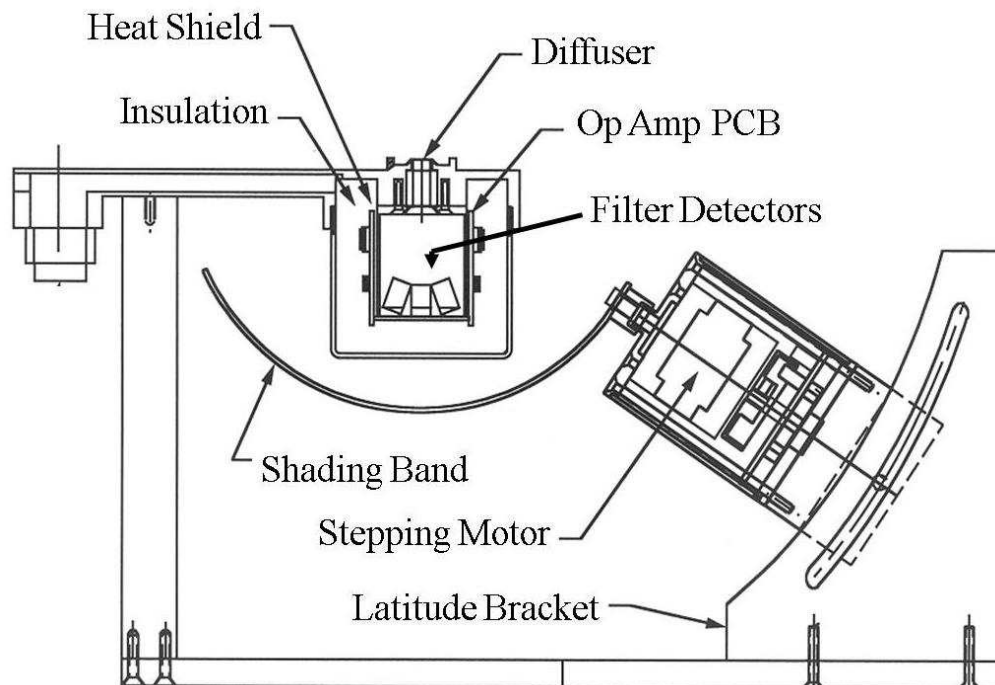


Figure 1.2 Cut-out view of a MFRSR (Hodges and Michalsky, 2011)

REFERENCES

- Ackerman T P, Stokes G (2003), The atmospheric radiation measurement program. *Phys Today*, 56(1): 38–45. doi:10.1063/1.1554135
- Alexandrov, D, Kiedron P, Michalsky J J, Godges G, Flynn C J, Lacis A A (2007), Optical depth measurements by shadow-band radiometers and their uncertainties. *Appl Opt*, 46(33): 8027–8038
- Alexandrov M D, Lacis A A, Carlson B E, Cairns B (2002), Remote sensing of atmospheric aerosols and trace gases by means of multi-filter rotating shadowband radiometer. part I: retrieval algorithm. *J Atmos Sci*, 59(3): 524–543. doi:10.1175/1520-0469(2002)059<0524:RSOAAA>2.0.CO;2
- Alexandrov M D, Lacis A A, Carlson B E, Cairns B (2002b), Remote sensing of atmospheric aerosols and trace gases by means of multi-filter rotating shadowband radiometer. part II: climatological applications. *J Atmos Sci*, 59(3): 544–566. doi:10.1175/1520-0469(2002)059<0544:RSOAAA>2.0.CO;2
- Alexandrov M D, Lacis A A, Carlson B E, Cairns B (2008), Characterization of atmospheric aerosols using MFRSR measurements. *J Geophys Res*, 113(D8): D08204. doi:10.1029/2007JD009388
- Alexandrov M D, Marshak A, Cairns B, Lacis A A, Carlson B E (2004), Automated cloud screening algorithm for MFRSR data. *Geophys Res Lett*, 31(4): L04118. doi:10.1029/2003GL019105
- Alexandrov M D, Schmid B, Turner D D, Cairns B, Oinas V, Lacis A A, Gutman S I, Westwater E R, Smirnov A, Eilers J (2009), Columnar water vapor retrievals from multifilter rotating shadowband radiometer data. *J Geophys Res*, 114(D2): D02306. doi:10.1029/2008JD010543
- Augustine J A, Cornwall C R, Hodges G B, Long C N, Medina C I, DeLuisi J J (2003), An automated method of MFRSR calibration for aerosol optical depth analysis with application to an Asian dust outbreak over the United States. *J Appl Meteorol*, 42(2): 266–278. doi:10.1175/1520-0450(2003)042<0266:AAMOMC>2.0.CO;2
- Augustine J A, Hodges G B, Cornwall C R, Michalsky J J, Medina C I (2005), An update on SURFRAD —The GCOS Surface Radiation budget network for the continental United States. *J Atmos Ocean Technol*, 22(10): 1460–1472. doi:10.1175/JTECH1806.1
- Bais A F (1997), Spectrometers: operational errors and uncertainties, Solar Ultraviolet Radiation Modeling, Measurements and Effects. In: Zerefos C S, Bais A F, eds .Vol. 52 of NATO ASI Series I, Global Environmental Change. Berlin: Springer-Verlag, 163–173

- Bais A F, Kazadzis S, Balis D, Zerefos C S, Blumthaler M (1998), Correcting global solar ultraviolet spectra recorded by a Brewer spectroradiometer for its angular response error. *Appl Opt*, 37(27): 6339–6344
- Bigelow D S, Slusser J R, Beaubien A F, Gibson J H (1998), The USDA ultraviolet radiation monitoring program. *Bull Am Meteorol Soc*, 79(4): 601–615. doi:10.1175/1520-0477(1998)079<0601:TUURMP>2.0.CO;2
- Blumthaler M, Bais A F (1996), Cosine corrections of global sky measurements, In: Kjeldstad B, Johnsen B, Koskela T, eds. *The Nordic Intercomparison of Ultraviolet and Total Ozone Instruments at Izana October 1996*. Helsinki: Finnish Meteorological Institute, 161–172
- Bodhaine B A, Wood N B, Dutton E G, Slusser J R (1999), On Rayleigh optical depth calculations. *J Atmos Oceanic Technol.*, 16: 1854–1861
- Booth C R, Mestechkina T, Morrow J H (1994), Errors in the reporting of solar spectral irradiance using moderate bandwidth radiometers: an experimental investigation. In: *Ocean Optics XII, Proc SPIE Int Soc Opt Eng*, 2258, 654–663
- Bruegge C J, Conel J E, Green R O, Margolis J S, Holm R G, Toon G (1992), Water vapor column abundance retrievals during FTFE. *J Geophys Res*, 97(D17): 18759–18768. doi:10.1029/92JD01050
- Bucholtz A (1995), Rayleigh-scattering calculations for the terrestrial atmosphere. *Appl Opt*, 34(15): 6339–6344
- Cachorro V E, Utrillas P, Vergaz R, Duran P, de Frutos A M, Martinez-Lozano J A (1998), Determination of the atmospheric water-vapor content in the 940-nm absorption band by use of moderate spectral-resolution measurements of direct solar irradiance. *Appl Opt*, 37(21): 4678–4689
- Cahalan R F (1994), Bounded cascade clouds: Albedo and effective thickness. *Nonlinear Process Geophys*, 1(2/3): 156–167. doi:10.5194/npg-1-156-1994
- Cairns B, Lacis A A, Carlson B E (2000), Absorption within inhomogeneous clouds and its parameterization in general circulation models. *J Atmos Sci*, 57(5): 700–714. doi:10.1175/1520-0469(2000)057<0700:AWICAI>2.0.CO;2
- Caldwell M M, Camp C W, Warner C W, Flint S D (1986), Action spectra and their role in assessing biological consequences of solar UV-B radiation change. In: Worrest R C, Caldwell M M, eds. *Stratospheric Ozone Reduction, Solar Ultraviolet Radiation and Plant Life*. Berlin: Springer-Verlag, 87–111
- Charlson R J, Schwartz S E, Hales J M, Cess R D, Coakley J A Jr, Hansen J E, Hofmann D J (1992), Climate forcing by anthropogenic aerosols. *Science. New Series*, 255(5043): 423–430

- Chen M, Davis J, Tang H, Gao Z, Gao W (2012), A multi-channel calibration method for multi-filter rotating shadow-band radiometer. Proc SPIE 8513. Remote Sensing and Modeling of Ecosystems for Sustainability, IX: 851305 doi:10.1117/12.929454
- Chow J C, Watson J G, Fujita E M, Lu Z, Lawson D R (1994), Temporal and spatial variations of PM_{2.5} and PM₁₀ aerosol in the Southern California air quality study. Atmospheric Environment, 28(12): 2061–2080
- di Sarra A, Fua D, Cacciani M, Di Iorio T, Disterhoft P, Meloni D, Monteleone F, Piacentino S, Sferlazzo D (2008), Determination of ultraviolet cosine-corrected irradiances and aerosol optical thickness by combined measurements with a Brewer spectrophotometer and a multifilter rotating shadowband radiometer. Appl Opt, 47(33): 6142–6150. doi:10.1364/AO.47.006142
- Feister U, Grewe R, Gericke K (1997), A method for correction of cosine errors in measurements of spectral UV irradiance. Sol Energy, 60(6): 313–332. doi:10.1016/S0038-092X(97)00030-3
- Forgan B W (1986), Sun photometer calibration by the ratio-Langley technique. In: Forgan B W, Fraser P J, eds. Baseline Atmospheric Program, Bureau of Meteorology, Melbourne, Australia, 22–26
- Forgan B W (1987), A technique for calibrating sunphotometers using solar aureole measurements. In: Forgan B W, Ayers G P, eds. Baseline, Bureau of Meteorology, Melbourne, Australia, 1989, 15–20
- Forgan B W (1988), Bias in solar constant determination by the Langley method due to structured aerosol: Comment. Appl Opt, 27(12): 2546–2548
- Forgan B W (1994), General method for calibrating Sun photometers. Appl Opt, 33(21): 4841–4850. doi:10.1364/AO.33.004841
- Fowle F E (1912), The spectroscopic determination of aqueous vapor. Astrophys J, 35(3): 149–162. doi:10.1086/141923
- Fowle F E (1915), The transparency of aqueous vapor. Astrophys J, 42(5): 394–411. doi:10.1086/142220
- Halthore R N, Eck T F, Holben B N, Markham B L (1997), Sun photometric measurements of atmospheric water vapor column abundance in the 940-nm band. J Geophys Res, 102(D4): 4343–4352. doi:10.1029/96JD03247
- Hansen J E, Travis L D (1974), Light scattering in planetary atmospheres. Space Sci Rev, 16(4): 527–610. doi:10.1007/BF00168069
- Harrison L, Michalsky J (1994), Objective algorithms for the retrieval of optical depths from ground-based measurements. Appl Opt, 33(22): 5126–5132

- Harrison L, Michalsky J, Berndt J (1994b), Automated multifilter rotating shadow-band radiometer: an instrument for optical depth and radiation measurements. *Appl Opt*, 33(22): 5118–5125
- Hickey J R (1970), Laboratory Methods of Experimental Radiometry Including Data Analysis, In: Landsberg H E, Van Mieghem J, eds., *Adv Geophys*, 14: 227-267. doi:10.1016/S0065-2687(08)60158-2
- Hodges G B, Michalsky J J (2011), Multifilter Rotating Shadowband Radiometer (MFRSR) Handbook with Subsections for the Following Derivative Instruments: Multifilter Radiometer (MFR) Normal Incidence Multifilter Radiometer (NIMFR), U.S. Department of Energy, Office of Science, Office of Biological and Environmental Research, DOE/SC-ARM/TR-059
- Holben B N, Eck T F, Slutsker I, Tanré D, Buis J P, Setzer A, Vermote E, Reagan J A, Kaufman Y J, Nakajima T, Lavenu F, Jankowiak I, Smirnov A (1998), AERONET—A federated instrument network and data archive for aerosol characterization. *Remote Sens Environ*, 66(1): 1–16. doi:10.1016/S0034-4257(98)00031-5
- Ingold T, Schmid B, Matzler C, Demoulin P, Kampfer N (2000), Modeled and empirical approaches for retrieving columnar water vapor from solar transmittance measurements in the 0.72, 0.82, and 0.94 mm absorption bands. *J Geophys Res*, 105(D19): 24327–24343. doi:10.1029/2000JD900392
- Janson G T, Slusser J R (2003), Long-term stability of UV multifilter rotating shadowband radiometers. Ultraviolet ground- and space-based measurements. *Models and Effects Iii Book Series: Proceedings of the Society of Photo-Optical Instrumentation Engineers*, 5156: 94–100 (SPIE) doi:10.1117/12.508195
- Kakani V G, Reddy K R, Zhao D, Mohammed A R (2003b), Effects of ultraviolet-B radiation on cotton (*Gossypium hirsutum* L.) morphology and anatomy. *Ann Bot (Lond)*, 91(7): 817–826. doi:10.1093/aob/mcg086
- Kakani V G, Reddy K R, Zhao D, Sailaja K (2003a), Field crop responses to ultraviolet-B radiation: a review. *Agric Meteorol*, 120(1–4): 191–218. doi:10.1016/j.agrformet.2003.08.015
- Kaskaoutis D G, Kambezidis H D, Kharol S K, Badarinath K V S (2008), The diffuse-to-global spectral irradiance ratio as a cloud-screening technique for radiometric data. *J Atmos Solar-Terrestrial Phys*, 70(13): 1597–1606
- Kassianov E, Barnard J C, Berg L K, Flynn C, Long C N (2011), Sky cover from MFRSR observations. *Atmos. Meas. Tech.*, 4: 1463–1470, doi:10.5194/amt-4-1463-2011.
- Kasten F, Young A T (1989), Revised optical air mass tables and approximation formula. *Appl Opt*, 28(22): 4735–4738. doi:10.1364/AO.28.004735

- Kiedron P, Berndt J, Michalsky J, Harrison L (2003), Column water vapor from diffuse irradiance. *Geophys Res Lett*, 30(11): 1565-1568. doi:10.1029/2003GL016874
- Kiedron P, Michalsky J, Schmid B, Slater D, Berndt J, Harrison L, Racette P, Westwater E, Han Y (2001), A robust retrieval of water vapor column in dry Arctic conditions using the rotating shadowband spectroradiometer. *J Geophys Res*, 106(D20): 24007–24016. doi:10.1029/2000JD000130
- Kiedron P W, Michalsky J J, Berndt J L, Harrison L C (1999), Comparison of spectral irradiance standards used to calibrate shortwave radiometers and spectroradiometers. *Appl Opt*, 38(12): 2432–2439. doi:10.1364/AO.38.002432
- Komhyr W D (1980), Operations Handbook—Ozone Observations with a Dobson Spectrophotometer, WMO Global Ozone Res. Monit. Proj. Report 6, World Meteorol. Organ. Geneva
- Krotkov N, Bhartia P K, Herman J, Slusser J, Labow G, Scott G, Janson G, Eck T F, Holben B (2005), Aerosol ultraviolet absorption experiment (2002 to 2004), part 1: ultraviolet multifilter rotating shadowband radiometer calibration and intercomparison with CIMEL sunphotometers. *Opt Eng*, 44(4): 041004. doi:10.1117/1.1886818
- Lee K H, Li Z, Cribb M C, Liu J, Wang L, Zheng Y, Xia X, Chen H, Li B (2010), Aerosol optical depth measurements in eastern China and a new calibration method. *J Geophys Res*, 115: D00K11. doi:10.1029/2009JD012812
- Leontieva E, Stamnes K (1996), Remote Sensing of Cloud Optical Properties from Ground-Based Measurements of Transmittance: A Feasibility Study. *J Appl Meteor*, 35(11): 2011–2022
- Lighty J S, Veranth J M, Sarofim A F (2000), Combustion aerosols: factors governing their size and composition and implications to human health. *J Air Waste Manag Assoc*, 50(9): 1565–1618. doi:10.1080/10473289.2000.10464197
- Livingston J, Schmid B, Redemann J, Russell P B, Ramirez S A, Eilers J, Gore W, Howard S, Pommier J, Fetzer E J, Seemann S W, Borbas E, Wolfe D E, Thompson A M (2007), Comparison of water vapor measurements by airborne Sun photometer and near-coincident in situ and satellite sensors during INTEX/ITCT 2004. *J Geophys Res*, 112(D12): D12S16. doi:10.1029/2006JD007733
- Long C N, Ackerman T P (2000), Identification of clear skies from broadband pyranometer measurements and calculation of downwelling shortwave cloud effects. *J Geophys Res*, 105(D12): 15609–15626. doi:10.1029/2000JD900077
- Madronich S (1993), UV radiation in the natural and perturbed atmosphere. In: Tevini M, ed., *UV-B Radiation and Ozone Depletion: Effects on Humans, Animals, Plants, Microorganisms, and Materials*. Lewis Publishers, Boca Raton, Florida, 17-69

- Mazzola M, Lanconelli C, Lupi A, Busetto M, Vitale V, Tomasi C (2010), Columnar aerosol optical properties in the Po Valley, Italy, from MFRSR data. *J Geophys Res*, 115(D17): D17206. doi:10.1029/2009JD013310
- Michalsky J J, Harrison L C, Berkheiser W E III (1995), Cosine response characteristics of some radiometric and photometric sensors. *Sol Energy*, 54(6): 397–402. doi:10.1016/0038-092X(95)00017-L
- Michalsky J J, Liljegren J C, Harrison L C (1995b), A comparison of Sun photometer derivations of total column water vapor and ozone to standard measures of same at the Southern Great Plains Atmospheric Radiation Measurement site. *J Geophys Res*, 100(D12): 25,995–26,003. doi:10.1029/95JD02706
- Michalsky J J, Min Q, Kiedron P W, Slater D W, Barnard J C (2001b), A differential technique to retrieve column water vapor using sun radiometry. *J Geophys Res*, 106(D15): 17,433–17,442. doi:10.1029/2000JD900527
- Michalsky J J, Schlemmer F A, Berkheiser W E, Berndt J L, Harrison L C, Laulainen N S, Larson N R, Barnard J C (2001a), Multi-year measurements of aerosol optical depth in the Atmospheric Radiation Measurement and Quantitative Links programs. *J Geophys Res*, 106(D11): 12099–12107. doi:10.1029/2001JD900096
- Molling C C, Heidinger A K, Straka W C III and Wu X (2010), Calibrations for AVHRR channels 1 and 2: review and path towards consensus. *International Journal of Remote Sensing*, 31(24): 6519–6540
- Monteith J L, Unsworth M H (2008), *Principles of environmental physics*, 3rd ed. Oxford: Academic
- Plana-Fattori A, Dubuisson P, Fomin B A, de Paula Corrêa M (2004), Estimating the atmospheric water vapor content from multi-filter rotating shadow-band radiometry at Sao Paulo, Brazil. *Atmos Res*, 71(3): 171–192. doi:10.1016/j.atmosres.2004.02.002
- Plana-Fattori A, Legrand M, Tanre D, Devaux C, Vermeulen A, Dubuisson P (1998), Estimating the atmospheric water vapor content from Sun photometer measurements. *J Appl Meteorol*, 37(8): 790–804. doi:10.1175/1520-0450(1998)037<0790:ETAWVC>2.0.CO;2
- Ramanathan V, Cess R D, Harrison E F, Minnis P, Barkstrom B R, Ahmad E, Hartmann D (1989), Cloud-radiative forcing and climate: results from the Earth radiation budget experiment. *Science*, 243(4887): 57–63. doi:10.1126/science.243.4887.57
- Ramanathan V, Crutzen P J, Kiehl J T, Rosenfeld D (2001), Aerosols, climate, and the hydrological cycle. *Science*, 294(5549): 2119–2124. doi:10.1126/science.1064034
- Reagan J, Thome K, Herman B, Stone R, Deluisi J, Snider J (1995), A comparison of columnar water-vapor retrievals obtained with near-IR solar radiometer and microwave radiometer measurements. *J Appl Meteorol*, 34(6): 1384–1391

- Reagan J, Pilewskie P, Herman B, Ben-David A (1987b), Extrapolation of Earth-based solar irradiance measurements to exoatmospheric levels for broad-band and selected absorption-band observations. *IEEE Trans Geosci Rem Sens*, GE-25(6): 647–653. doi:10.1109/TGRS.1987.289733
- Reagan J A, Thome K, Herman B, Gall R (1987a), Water vapor measurements in the 0.94 micron absorption band: Calibration, measurements, and data applications. In: *Proceedings, International Geoscience and Remote Sensing Symposium, '87 Symposium*, Ann Arbor, Mich. IEEE, 63–67
- Schmid B, Hegg D A, Wang J, Bates D, Redemann J, Russell P B, Livingston J M, Jonsson H H, Welton E J, Seinfeld J H, Flagan R C, Covert D S, Dubovik O, Jefferson A (2003), Column closure studies of lower tropospheric aerosol and water vapor during ACE-Asia using airborne Sun photometer and airborne in situ and ship-based lidar measurements. *J Geophys Res*, 108(D23): 8656-8677. doi:10.1029/2002JD003361
- Schmid B, Michalsky J J, Slater D W, Barnard J C, Halthore R N, Liljegren J C, Holben B N, Eck T F, Livingston J M, Russell P B, Ingold T, Slutsker I (2001), Comparison of columnar water-vapor measurements from solar transmittance methods. *Appl Opt*, 40(12): 1886–1896
- Schmid B, Spyak P R, Biggar S F, Wehrli C, Sekler J, Ingold T, Matzler C, Kampfer N (1998), Evaluation of the applicability of solar and lamp radiometric calibrations of a precision Sun photometer operating between 300 and 1025 nm. *Appl Opt*, 37(18): 3923–3941
- Schmid B, Thome K J, Demoulin P, Peter R, Matzler C, Sekler J (1996), Comparison of modeled and empirical approaches for retrieving columnar water vapor from solar transmittance measurements in the 0.94 mm region. *J Geophys Res*, 101(9): 345–349, 358
- Schmid B, Wehrli C (1995), Comparison of Sun photometer calibration by use of the Langley technique and the standard lamp. *Appl Opt*, 34(21): 4500–4512. doi:10.1364/AO.34.004500
- Seckmeyer G, Bernhard G (1993), Cosine error correction of spectral UV irradiances. In: *Stamnes K H, ed. Atmospheric Radiation, Proc. SPIE*, 2049: 140–151
- Shaw G E (1976), Error analysis of multi-wavelength sun photometry. *Pure Appl Geophys*, 114(1): 1–14. doi:10.1007/BF00875487
- Shaw G E (1982), Solar spectral irradiance and atmospheric transmission at Mauna Loa Observatory. *Appl Opt*, 21(11): 2007–2011
- Shiobara M, Spinhirne J D, Uchiyama A, Asano S (1996), Optical depth measurements of aerosol, cloud, and water vapor using Sun photometers during FIRE Cirrus IFO II. *J Appl Meteorol*, 35(1): 36–46. doi:10.1175/1520-0450(1996)035<0036:ODMOAC>2.0.CO;2

- Slusser J, Gibson J, Bigelow D, Kolinski D, Disterhoft P, Lantz K, Beaubien A (2000), Langley method of calibrating UV filter radiometers. *J Geophys Res*, 105(D4): 4841–4849. doi:10.1029/1999JD900451
- Smirnov A, Holben B N, Eck T F, Dubovik O, Slutsker I (2000), Cloud screening and quality control algorithms for the AERONET database. *Remote Sens Environ*, 73(3): 337–349. doi:10.1016/S0034-4257(00)00109-7
- Teramura A H, Sullivan J H, Ziska L H (1990), Interaction of Elevated Ultraviolet-B Radiation and CO₂ on Productivity and Photosynthetic Characteristics in Wheat, Rice, and Soybean. *Plant Physiol*, 94(2): 470–475. doi:10.1104/pp.94.2.470
- Thomason L W, Herman B M, Reagan J A (1983), The effect of atmospheric attenuators with structured vertical distributions on air mass determinations and Langley plot analysis. *J Atmos Sci*, 40(7): 1851–1854
- Thome K J, Herman B, Reagan J (1992), Determination of precipitable water from solar transmission. *J Appl Meteorol*, 31(2): 157–165. doi:10.1175/1520-0450(1992)031<0157:DOPWFS>2.0.CO;2
- Thome K J, Smith M W, Palmer J M, Reagan J A (1994), Three-channel solar radiometer for the determination of atmospheric columnar water vapor. *Appl Opt*, 33(24): 5811–5819. doi:10.1364/AO.33.005811
- Thuillier G, Hers M, Simon P C, Labs D, Mandel H, Gillotay D (1998), Observation of the solar spectral irradiance from 200 to 870 nm during the ATLAS 1 and ATLAS 2 mission by the SOLSPEC spectrometer. *Metrologia*, 35(4): 689–695. doi:10.1088/0026-1394/35/4/79
- Vanden Berghen F, Bersini H (2005), CONDOR, a new parallel, constrained extension of Powell's UOBYQA algorithm: experimental results and comparison with the DFO algorithm. *Journal of Computational and Applied Mathematics*, 181(1): 157–175. doi:10.1016/j.cam.2004.11.029
- Wielicki B A, Cess R D, King M D, Randall D A, Harrison E F (1995), Mission to Planet Earth: role of clouds and radiation in climate. *Bull Am Meteorol Soc*, 76: 2125–2153
- Willson R C, Mordvinov A V (2003), Secular total solar irradiance trend during solar cycles 21–23. *Geophys Res Lett*, 30(5): 1199–1202. doi:10.1029/2002GL016038
- Wilson S R, Forgan B W (1995), In situ calibration technique for UV spectral radiometers. *Appl Opt*, 34: 5475–5484
- Yin B, Min Q, Duan M, Bartholomew M J, Vogelmann A M, Turner D D (2011), Retrievals of cloud optical depth and effective radius from Thin-Cloud Rotating Shadowband Radiometer measurements. *J Geophys Res*, 116(D23): D23208. doi:10.1029/2011JD016192

CHAPTER 2: A NEW CLOUD SCREENING ALGORITHM FOR GROUND-BASED DIRECT-BEAM SOLAR RADIATION²

Introduction

Ground-based solar radiation measurement systems are generally considered simple, reliable, and necessary to validate satellite measurements and retrievals (Smirnov et al. 2000; Krotkov et al. 2005). Separation of clear-sky and cloudy portions in measurements is an essential requirement that all these ground systems have to fulfill during in-situ calibration and while producing retrievals of atmospheric properties [e.g. aerosol optical depth (AOD)]. One of the most common in-situ calibration methods for direct-beam-measuring instruments [e.g. sunphotometer and Multi-Filter Rotating Shadow-band Radiometer (MFRSR)] is Langley regression (Stephens 1994), which can only be applied on cloud-screened data.

The U.S. Department of Agriculture (USDA) UV-B Monitoring and Research Program (UVMRP) has been observing solar UV radiation at 37 sites across United States for over a decade. The primary instrument it uses is the Ultraviolet version of MFRSR (UV-MFRSR). The UV-MFRSR receives the direct normal, diffuse horizontal, and total horizontal solar radiation at seven UV channels characterized by 2-nm full width at half maximum (FWHM) bandpasses and are nominally centered at wavelengths of 300, 305, 311, 317, 325, 332, and 368 nm (Slusser et al. 2000).

² This chapter includes the complete published manuscript (minimal modifications were made to meet formatting requirements):

Chen M, Davis J, Gao W (2014), A New Cloud Screening Algorithm for Ground-Based Direct-Beam Solar Radiation. *Journal of Atmospheric and Oceanic Technology*, 31(12): 2591-2605. doi: 10.1175/JTECH-D-14-00095.1. ©American Meteorological Society. Used with permission.

Chen et al. (2013) reviewed ground-based cloud screening methods published over the last two decades. There are four common types of cloud screening. In the first type, cloud screening is performed on uncalibrated voltage data—the standard Langley analysis or its variants fall into this category. In the second type, cloud screening is performed on calibrated irradiance data. In the third type, cloud screening is performed on derived AOD data. In the fourth type, cloud screening is performed using collocated auxiliary equipment/data, such as a Total Sky Imager (TSI). Here we briefly review some common algorithms.

If the cloud screening method is based on ratios of measured voltages or irradiances rather than their absolute quantities, then this cloud screening method can apply to both the first and second types because the uncalibrated voltage data and the calibrated irradiance data have a constant ratio. Most type 2 cloud screening algorithms are not designed for the purpose of calibration. It is desirable to have a cloud screening algorithm suitable for both applications.

The current cloud screening module used by the UVMRP is the Langley Analyzer (LA), which was developed at the Atmospheric Solar Radiation Group at SUNY-Albany NY. This technique, which uses the methodology described in Harrison and Michalsky (1994), is a two-step filter on a series of log transformed voltage ($\ln V$) and airmass points. In the first step, points are sorted by airmass in ascending order and segments beginning at the point where $\ln V$ starts to increase and ending at the point where $\ln V$ starts to decrease are classified as cloudy (Chen et al. 2013). In the second step, the concavity test, the points with the slope of $\ln V$ exceeding a given threshold are cloudy. One of the LA variants developed by Lee et al. (2010) uses the maximum value composite (MVC) technique to acquire the largest voltage values in narrow airmass intervals. Those composite values are considered to be close to voltages measured under clear-sky conditions.

Long and Ackerman (2000) developed a cloud screening algorithm for irradiance data from pyranometers. The downwelling irradiances—the total and the diffuse components are normalized by airmass. Applying thresholds on these two airmass-normalized components eliminates scenes containing optically thick clouds or haze, as well as high thin clouds, such as cirrus. Applying thresholds on irradiance variation over time and in comparison to a normalized diffuse ratio may eliminate some other cloudy points. When new cloudy points are detected in these processes, threshold values mentioned above will be adjusted and a new iteration of screening is triggered. Otherwise, the surviving points are the final clear-sky points.

Alexandrov et al. (2004) proposed an automated cloud screening algorithm for the time series of AOD derived from a single MFRSR channel. The method renormalizes the AOD time series by removing the local AOD average and calculates the corresponding inhomogeneity index (ϵ') for each point. The statistical distribution of ϵ' over a long period will show two distinctive maxima that correspond to the aerosol and cloud modes respectively. Applying a threshold between the two maxima, the method separates the clear-sky points and cloudy points.

Smirnov et al. (2000) developed an automatic cloud screening algorithm on the time series of AOD derived from calibrated sunphotometers of the Aerosol Robotic Network (AERONET). Essentially, this algorithm requires that clear-sky points 1) are within a certain AOD range, 2) have stable and smooth AOD in nearby points, and 3) do not exceed a certain standard deviation of AODs from the daily AOD average.

The limitations of the existing cloud screening algorithms include:

1) being able to perform only on the time series of optical depth (e.g. the index of inhomogeneity algorithm; Alexandrov et al. 2004), which requires accurate calibration that may not be available at current step;

2) requiring consideration of the variation of nearby points or points in a relatively short window (e.g. in Index of Inhomogeneity algorithm, the measurements taken within 5 minutes (or 17 points) are used to determine the cloudiness of the center point); or

3) missing some clear intervals due to their short duration or contamination by slight noise. For example, in LA, the slope between nearby points cannot exceed a certain threshold.

This paper proposes a new method that examines the surface-measured direct-beam irradiance (voltage) with the purpose of identifying the clear-sky points in the data. The main improvements of the proposed method include the following: 1) cloudy points can be compared to all points within a time (airmass) window of any length; 2) clear-sky transitional points and short clear-sky segments can survive the screening; and 3) the method does not require the Langley offset voltage and provides more clear points, which may be missed by the other methods.

The following sections will describe the new TOD pairing cloud screening algorithm, show its advantages mentioned above compared to other methods (especially the LA method), and its ability to obtain more Langley offsets on the cloud-screened data.

The algorithm description

The basis

Beer's Law tells us that

$$V_t = V_{LO} \exp(-\tau_{Total,t} \cdot m_t) \quad (2.1)$$

Where, m_t is the airmass at time t ; V_t is the cosine corrected voltage of the direct beam at time t at one channel; V_{LO} is the corresponding voltage as if measured at the top of the

atmosphere (airmass=0; also known as the Langley voltage offset); $\tau_{Total,t}$ (TOD_t) is the total optical depth (TOD in the nadir direction) at t .

Taking the natural logarithm and rearranging, Eq. (2.1) can be recast as:

$$TOD_t = m_t^{-1} \ln V_{LO} - m_t^{-1} \ln V_t \quad (2.2)$$

It is noted that the Beer's Law is based on the single scattering assumption, which cloudy measurements do not obey. However, the purpose of this work is to distinguish cloudy points from clear points rather than to give an accurate optical depth at each point. The value of cloud plus aerosol optical depth value can be derived from the signal of a well-calibrated radiometer after subtraction of the Rayleigh scattering and gaseous absorption. By definition, cloudy points have higher total optical depth values than clear points. Therefore, clear points tend to distribute around the upper envelope in the $(m_t, \ln V_t)$ coordinate system, while the cloudy points scattered lower than the envelope. This is one of the few assumptions on which the current cloud screening algorithm depends.

The transformed coordinate system

Instead of the original measurement pair (m_t, V_t) , we use the transformed pair $(m_t^{-1}, m_t^{-1} \ln V_t)$ in the following discussion. The benefit of this transformation is that the TOD_t can be examined at any time t directly because the slant paths have already been corrected or normalized by moving the m_t term to the right-hand side of the Eq. (2.2).

Figure 2.1 illustrates the transformed coordinate system. The mathematical basis for the whole figure is given by Eq. (2.2). In the normal Langley calibration method V_{LO} is used with the extraterrestrial irradiance to determine the responsivity of the instrument and it is assumed here

that V_{LO} or its natural logarithm $\ln V_{LO}$ is constant during a short time range (e.g. one day). If the TODs were zeroes, the ground measurements (V_i) would be close to the extraterrestrial counterpart (V_{LO}), which is constant by our assumption. The pair of ($m_i^{-1}, m_i^{-1} \ln V_{LO}$) would be on a straight line (the blue dash line) approaching the origin. According to Eq. (2.2), any measurement with TOD greater than zero would have a V_i less than V_{LO} . Therefore, the blue dashed line is the upper limit for ground measurements because the real TODs are greater than zero, because of the Rayleigh scattering and gaseous absorptions. When measurements are taken on a clear day, the TODs would be stable and Eq. (2.2) applied to these measurements could be treated as a linear regression problem, where m_i^{-1} is the independent variable, $m_i^{-1} \ln V_i$ is the dependent variable, $-TOD_{LR}$ is the intercept of the regression line, and $\ln V_{LO}$ is the slope of the regression line. The green dash line (the linear regression line) on black solid circles (clear-day measurements) gives an example of such a regression. Note that the TOD at any time is given as the vertical difference between the extraterrestrial line and the clear-sky line.

The coordinate transformed measurements are sorted by m_i^{-1} in ascending order. When applying the algorithm to more than half of a day, it is possible that multiple points have the same m_i^{-1} . In our procedure, the first occurrence of such points is kept while the rest are removed. Since more than one-half day may be considered, the usage of the word “time” refers to the corresponding m_i^{-1} .

The outline of the algorithm

At the beginning, the algorithm treats every measurement as an indeterminate point, which means the cloudiness of this measurement has not been determined. The methodology of

the procedure is to start by comparing the TOD of this point with other points to determine whether it is cloudy; and if it is not definitely cloudy, then to use it in determining whether other points are cloudy. The point whose cloudiness is to be determined is called the target point. All indeterminate points within a certain “time” range surrounding but excluding the target point constitute the local window for that target point.

The procedure pairs an indeterminate point in the local window with all other indeterminate points in the same local window. For a pair of such points, a particular type of weighted average TOD is calculated. If the two points of a pair represent nearly clear-sky points, then the TOD difference between the target and the weighted average of such a pair is an indicator of the target point’s cloudiness. The sections below mathematically explain why the algorithm uses the weighted TOD average rather than the standard average in comparing with the target’s TOD. Then a description is given of how to calculate the TOD difference between the target and a paired points’ weighted averages without knowing the value of V_{LO} .

Figure 2.2 gives an example of a target (the purple pentagon) and one pair of points in its local window (green triangles).

In practice, comparing the target’s TOD to the average of only one pair may not be determinate due to the possibility of including cloudy points in the pair. Therefore, an assumption is made that there are many pairs of clear-sky points in the local window and the differences between the target’s TOD and those pairs’ weighted TOD averages would cluster at one value. Then, we calculate the TOD differences between the target and all pairs’ weighted averages in the local window. With the assumption above, outliers of the TOD differences are removed and the mean TOD difference of the remaining pairs is considered as a more robust

indicator of the target's cloudiness. If the mean TOD difference is positive and greater than a reasonable threshold, then the target is definitely cloudy.

When applying the screening routine described above on every indeterminate point, the examining order does not matter and doing so completes one iteration. Cloudy points will retain the cloudy status and be excluded in the future operations. A new iteration is triggered if any new cloudy points are found in the last iteration. If there were no new cloudy points found in the last iteration, the cloud screening finishes. The surviving indeterminate points are considered clear points.

Following the algorithm design, the points with higher TODs are more likely to be labeled cloudy in the early iterations, while the points with TODs close to the baseline are more likely to survive the screening as would be anticipated.

Algorithm Implementation

Pairing and TOD differences

The explicit expressions for the total optical depth at each point in the local window are:

$$\begin{aligned}
 TOD_0 &= m_0^{-1} \ln V_{LO} - m_0^{-1} \ln V_0 \\
 &\dots \\
 TOD_k &= m_k^{-1} \ln V_{LO} - m_k^{-1} \ln V_k \\
 &\dots \\
 TOD_{Np-1} &= m_{Np-1}^{-1} \ln V_{LO} - m_{Np-1}^{-1} \ln V_{Np-1}
 \end{aligned} \tag{2.3}$$

Where, Np is the number of indeterminate points in the local window of the target (Tgt). Since there should be at least one pair in the local window, the minimum value for Np is 2. There is no maximum limitation for Np . In practice, the window size for UVMRP data is set to 256,

which is large enough to include all points in a day (UVMRP data are measured every 20 seconds and the average recorded every three minutes).

The explicit expression for the total optical depth at the target Tgt is:

$$TOD_{Tgt} = m_{Tgt}^{-1} \ln V_{LO} - m_{Tgt}^{-1} \ln V_{Tgt} \quad (2.4)$$

Defining Δm_k^{-1} as the difference between the reciprocal of airmass at the k th point (m_k^{-1}) and that at the target (m_{Tgt}^{-1}):

$$\Delta m_k^{-1} = m_k^{-1} - m_{Tgt}^{-1} \quad (2.5)$$

With Eq. (2.5) and Eq. (2.4), Eq. (2.3) can be rewritten as

$$\begin{aligned} TOD_0 &= (m_{Tgt}^{-1} + \Delta m_0^{-1}) \ln V_{LO} - (m_{Tgt}^{-1} + \Delta m_0^{-1}) \ln V_0 \\ &\dots \\ TOD_k &= (m_{Tgt}^{-1} + \Delta m_k^{-1}) \ln V_{LO} - (m_{Tgt}^{-1} + \Delta m_k^{-1}) \ln V_k \\ &\dots \\ TOD_{Np-1} &= (m_{Tgt}^{-1} + \Delta m_{Np-1}^{-1}) \ln V_{LO} - (m_{Tgt}^{-1} + \Delta m_{Np-1}^{-1}) \ln V_{Np-1} \end{aligned} \quad (2.6)$$

Since no two points have the same airmass, direct TOD comparison between the target and any local window point is impossible when V_{LO} is unknown (see APPENDIX 2.A). For the same reason, it is also almost impossible to compare target's TOD with a standard TOD average of two local window points (see APPENDIX 2.B).

The standard average is a special case of a linear combination. Fortunately, for our purpose—comparing the target's TOD to a pair of local window points (A and B)—any linear combination of TOD_A and TOD_B fulfills the requirement. The derivation of Eq. (2.7) to Eq. (2.11) shows how to calculate the TOD difference between the target and a pair points' weighted average without knowing the calibration term.

Defining $wTOD_{AB}$ as the weighted TOD average of points A and B,

$$wTOD_{AB} = \frac{(M_A \cdot TOD_A + M_B \cdot TOD_B)}{M_T} \quad (2.7)$$

where, M_A , M_B , and M_T are three nonzero real value multipliers. We are free to define the relationship between the three multipliers as:

$$M_T = M_A + M_B \quad (2.8)$$

Since M_A and M_B can be any nonzero real values, we can set $M_A = \Delta m_B^{-1}$, $M_B = -\Delta m_A^{-1}$ and get the following equation:

$$M_A \cdot \Delta m_A^{-1} + M_B \cdot \Delta m_B^{-1} = 0 \quad (2.9)$$

Replacing TOD_A and TOD_B with Eq. (2.6) and applying Eq. (2.8) and (2.9), Eq. (2.7) can be recast as

$$wTOD_{AB} = m_{Tgt}^{-1} \cdot \ln V_{LO} - \frac{M_A \cdot m_A^{-1} \cdot \ln V_A + M_B \cdot m_B^{-1} \cdot \ln V_B}{M_T} \quad (2.10)$$

Using Eq. (2.4) and Eq. (2.10), we define ΔTOD_p as the difference between the target's TOD (TOD_{Tgt}) and the weighted TOD average of points A and B ($wTOD_{AB}$):

$$\begin{aligned} \Delta TOD_p &= TOD_{Tgt} - wTOD_{AB} \\ &= -m_{Tgt}^{-1} \ln V_{Tgt} + \frac{M_A \cdot m_A^{-1} \cdot \ln V_A + M_B \cdot m_B^{-1} \cdot \ln V_B}{M_T} \end{aligned} \quad (2.11)$$

It is noted that all V_{LO} terms cancel out in Eq. (2.11), which means that the calculation of ΔTOD_p does not depend on the Langley voltage offset. Since points A and B represent any two local window points, this advantage applies for all other pairs.

Outliers

In practice, examining the difference between the target's TOD and a single pair's average TOD in the window may not be conclusive because of the possibility of including cloudy points in the pair. Figure 2.3 shows an example of the histogram of ΔTOD_p . The x axis is ΔTOD_p with the bin size of 0.05. The y axis is the frequency (number of cases) of the target's pairs' ΔTOD_p falling into the bins. It is seen that the histogram of ΔTOD_p has an obvious cluster center and long tails on both sides. Since there are ample clear-sky-point pairs in this example, the cluster center represents clear-sky-point pairs' ΔTOD_p and the tails represent pairs containing cloudy points. Figure 2.4 illustrates the effect of pair points' cloudiness in calculating ΔTOD_p . Figure 2.4a shows the case when both pair points (A and B) are clear. In this case, no matter where target's location—left, right, or between—relative to the A–B pair, all ΔTOD_p values are the same. Figure 2.4b shows the case when pair point A (left) is cloudy and pair point B (right) is clear. In this case, targets on the left side of point B will have ΔTOD_p lower than ΔTOD_p compared to Figure 2.4a, while the target on the right side of point B will have ΔTOD_p higher than ΔTOD_p compared to Figure 2.4a. Figure 2.4c shows the case when pair point A (left) is clear and pair point B (right) is cloudy. In this case, targets on the left side of point A will have ΔTOD_p higher than ΔTOD_p compared to Figure 2.4a, while the target on the right side of point A will have ΔTOD_p lower than ΔTOD_p compared to Figure 2.4a. Since the assumption has been made that there are many pairs of clear-sky points in the local window, it will result in ΔTOD_p clustering to one value—the peak in Figure 2.3—near ΔTOD_p for Figure 2.4a, and ΔTOD_p for other cases will deviate from the clustered value and appear less

frequently—the tails in Figure 2.3. Therefore, the algorithm can remove the ΔTOD_p outliers (points outside of two standard deviations from the mean ΔTOD_p value) from all pairs in the local window (the tails in Figure 2.3) to limit the influence of potential cloudy points. The process is repeated two to five times varying by sites.

In Eq. (2.12), P_R are the sets of remaining pairs (near the peak in Figure 2.3), which are also considered as clear-sky pairs and ΔTOD_{Tgt} is the mean difference between the TOD of the target and the weighted TOD of the remaining clear-sky pairs, which is the simple average of ΔTOD_p on the remaining pairs (P_R):

$$\Delta TOD_{Tgt} = \frac{\sum_{AB \in P_R} \Delta TOD_p}{size(P_R)} \quad (2.12)$$

Threshold

Since cloudy points have higher total optical depth values than clear points, we can set a threshold value $T_{\Delta TOD}$, above which the target's TOD is too high compared to the weighted TODs of clear-sky pairs in the local window. Therefore, the condition of $\Delta TOD_{Tgt} > T_{\Delta TOD}$ suffices to determine the target to be cloudy.

If the purpose of using this cloud screening algorithm is to identify the clearest points in a period and to obtain the Langley offset from those points, a lower value of $T_{\Delta TOD}$ (e.g. 0.008) is preferred. If the purpose is to identify points that are not contaminated by thick clouds and to study the other constituents in the atmosphere (e.g. aerosols and trace gases), a higher value of $T_{\Delta TOD}$ is preferred.

The flowchart of the whole cloud screening algorithm is presented in Figure 2.5.

Accuracy Assessment

Although it has been assumed that there are adequate clear-sky points to obtain a cluster of AODs near the clear-sky value, nevertheless it is useful to confirm that the points identified as clear actually are. As an example of how this can be achieved, the measured diffuse to direct ratio (DDR) can be compared to the modeled value for a clear sky. The UV-MFRSR provides both the direct normal and diffuse horizontal irradiance measurements simultaneously. Before calibration, these irradiances are measured in units of millivolts. However, the direct normal and diffuse horizontal irradiance ratio (DDR) of the calibrated irradiances and uncalibrated voltages are the same because the same responsivity is used to convert both voltage measurements to their respective irradiance values. If the AOD, the Rayleigh optical depth (ROD), the ozone optical depth, solar geometry, and site location are known, then a radiative transfer routine such as the moderate spectral resolution radiative transport model (MODTRAN, <http://modtran5.com/>, Anderson et al. 2009; Berk et al. 2006) for UV and visible channels or the tropospheric UV model (Madronich, 1993) for UV channels are capable of simulating DDR. Solar geometry and site location are measured and known properties. ROD is a function of ground pressure and site location (Bodhaine et al. 1999) and is relatively stable over a day. Ozone optical depths are negligible at 368-nm channel. When it is important, the total column ozone amount data are available from satellite. By elimination, AOD is the main unknown source that affects the DDR simulation. Therefore, AODs can be estimated by matching the MODTRAN modeled and UV-MFRSR-measured DDRs on points indicated as clear. Using the retrieved mean AOD value, the direct normal irradiances at the clear-sky points are simulated by MODTRAN. The Langley regression can be applied to the measurements indicated as clear and the V_{LO} obtained, which is used to calibrate the direct normal voltage data. The closer the direct normal irradiances from the

Langley calibration and MODTRAN simulation, the more accurate the V_{LO} . An accurate V_{LO} suggests that the points selected by the cloud screening algorithm are clear-sky points. Figure 2.6 summarizes the accuracy assessment procedure described above.

Results

The HI02 site at Mauna Loa, Hawaii is a climatology site operated by USDA UV-B Monitoring and Research Program (UVMRP). Because of its high altitude (3409 m) and great distance from any continents, its atmosphere is less affected by varying aerosol loading and is relatively stable, which makes HI02 a good site for applying Langley regression. The original Langley analysis at HI02 gives more V_{LO} hits with lower fluctuation compared to other UVMRP sites. To demonstrate that the new cloud screening method has the ability of selecting good points for calibration, the V_{LO} s from linear regression on clear points given by the new cloud screening method and those from the original Langley analysis at HI02 in 2013 are compared. Figure 2.7 shows a comparison of the relative differences of V_{LO} (sun-earth distance factor normalized) between values derived from linear regression of Eq.(2.2) on the points passing the new cloud screening algorithm and those from the original Langley analysis. The circles represent the sunny-day cases when almost all points are measured with no cloud contamination and the squares represent the partly-cloudy cases. Except for some sporadic outliers, the relative difference is about -2% to 0%. On sunny days, the points remaining after applying the new cloud screening algorithm are usually the same as those passing the internal cloud screening module in the Langley analysis. The relative difference of V_{LO} at around -1% in a such case is believed to

result from the fact that the coordinate system of $(m_t^{-1}, m_t^{-1} \ln V_t)$ used in this paper gives relatively balanced weights to both points with high and low airmass in the linear regression. It is also evident that the relative differences of V_{LO} between the sunny-day cases and the partly cloudy cases compare well, which suggests that the new cloud screening algorithm gives points that generate unbiased V_{LO} in partly-cloudy cases as compared to the sunny-day cases.

The stable atmosphere at HI02 site is optimal for Langley calibration; however, for many sites where air pollution, clouds and the combination of both are frequent, the Langley method is not as reliable as a means of calibration. In contrast, the FL02 site at Homestead, Florida is characterized by frequent and fast-moving stratocumulus clouds. The internal cloud screening module of the original Langley analysis often misses short periods of clear points. As a result, there may not be sufficient clear points to calculate V_{LO} . Figure 2.8 shows the FL02 368-nm channel's V_{LO} s (sun-earth distance factor normalized) in 2013 from the original Langley analysis and those from the linear regression of the points passing the new cloud screening algorithm. The latter gives about 56% more V_{LO} s than the original LA in 2013. The mean value of V_{LO} s using the new cloud screening algorithm is about 2.8% lower than that of the original LA and the standard deviation is about 4% higher.

Figure 2.9 shows an example of the cloud screening performance of the original Langley analysis (upper) and the new method (lower) at FL02 site on 26 September 2013. The point sets for the two methods are the same: morning points with an airmass range between 1.5 and 3.0. For the Langley analysis 12 points survived from its cloud screening procedure and 5 clear points (3 in transition between clear and cloudy and 2 in short clear periods) are missed in comparison to the new method. After the removal of regression outliers, the Langley analysis

allows 9 points, which is less than its minimum requirement (12 points), and therefore the original Langley analysis does not generate V_{LO} on that day. The new cloud screening method picks up all five clear points missed by the original Langley analysis and has 17 points for the further linear regression process. Although 2 of them are the regression outliers, there are still 15 points left to generate V_{LO} on that day. The V_{LO} (raw, without sun-earth distance normalization) generated using the clear points that survived the new cloud screening algorithm is 1576.40. One can calculate the corresponding V_{LO} (norm, sun-earth distance normalized) as 1584.29, which is in the middle of all V_{LO} (norm) in 2013 at FL02. This example shows the new cloud screening algorithm's ability of picking up clear points in transitional regions and in short clear-sky periods. It also shows that the calibration based on Langley regression can benefit from including those clear points.

To demonstrate the performance of V_{LO} generated in the last example (FL02, 368nm, 26 September 2013), the simulation of direct normal irradiance using the radiative transfer model MODTRAN is conducted. The AOD is determined by matching the MODTRAN modeled and UV-MFRSR measured DDRs on clear-sky points. The mean AOD value for this case is 0.103 at 550nm (or 0.154 at 368nm channel). The values of important input parameters to the MODTRAN model are listed in APPENDIX 2.C. Figure 2.10 displays the MODTRAN-simulated and the new-method-calibrated direct normal irradiance at FL02 on 26 September 2013. The clear-sky points' irradiances are plotted with dark blue circles and the cloudy points' irradiances are plotted with light blue circles. The MODTRAN simulations are the small red points. It is seen that all clear-sky points' irradiances are close to the MODTRAN results, including the five points saved by the new cloud screening method but missed by the LA cloud

screening module. The five points are indicated by the arrows in Figure 2.10. The mean square error (MSE) for this case is $2.87e-5$ while the MSE value for a day inappropriate for Langley analysis may be two to three magnitudes higher. It suggests that the clear-sky points have nearly equal AOD values. It is also evident that cloudy points determined by the new cloud screening algorithm have much lower irradiances than clear-sky points (Figure 2.10).

Table 2.1 lists the statistics of V_{LO} s before and after applying the new cloud screening algorithm to measurements of 368-nm irradiances at five UVMRP sites in 2013. For the relatively clearer sites, HI02 and NM02, the number of V_{LO} s increased slightly and the annual mean value of V_{LO} s decreased by 1% after substituting the cloud screening module in the original Langley analysis. For sites where cloudy measurements are more frequent—that is FL02, OK02, and CO02—the number of V_{LO} s increased between 33.8% to 56.7% and the annual mean value of V_{LO} s decreased between 2.51% to 3.41%. The increased number of V_{LO} s suggests that the new TOD pairing cloud screening algorithm picks up significantly more V_{LO} s at cloudy sites. The larger decrease in the annual mean value of V_{LO} at cloudy sites suggests the potential for improving calibration accuracy at those sites.

Summary

A new cloud screening algorithm for narrowband direct-beam measurements is developed. The mathematical basis of this algorithm is Beer's law. Measurements are reorganized to a converted coordinate system that emphasizes the relative magnitude of measurements' total optical depth (TOD). Instead of examining the fluctuation of a target

measurement with nearby points, this algorithm calculates the TOD difference between a target and pairs of all indeterminate points and considers the target a cloudy point if the TOD difference exceeds a certain threshold value. All points are in indeterminate status at the beginning of cloud screening. Each point is examined with all other indeterminate points. If new cloudy points are found, a new iteration of examination is triggered. The cloud screening finishes when no new cloudy points are found in the last iteration. The surviving indeterminate points are considered clear points. The new cloud screening method is verified by comparing the Langley voltage offsets (V_{LO} s) determined from the clear-sky intervals to values generated by linear regression in the original calibration program LA. The results at the relatively clear site at Mauna Loa Observatory, HI shows that values of V_{LO} s from partly cloudy days are not biased in comparison to those from sunny days. The results at the more cloudy site at Homestead, FL shows that 56% more V_{LO} s are identified with the new cloud screening method than with the original Langley analysis, while the differences in means and standard deviations between the two methods are less than 3% and 4%, respectively. The new TOD pairing cloud screening algorithm picks up significantly more V_{LO} s at cloudy sites. The larger decrease of the annual mean value of V_{LO} s at relatively cloudy sites than at relatively clear sites suggests the potential for improving calibration accuracy at cloudy sites. The result also shows that the new cloud screening method is capable of picking up clear points in short clear windows and in transitional regions.

Table 2.1 The statistics of V_{LO} s (normalized by a sun-earth distance factor) before and after applying the new cloud screening algorithm at 368 nm channel at five UVRMP sites in 2013.

	V_{LO} Source*	Num. (V_{LO})	Mean(V_{LO})	Percent difference (V_{LO})
HI02	oLA	274	1748.64	-1.11%
	CSLA	289	1729.28	
FL02	oLA	83	1631.45	-2.85%
	CSLA	130	1585.60	
NM02	oLA	242	1388.49	-1.03%
	CSLA	250	1374.13	
OK02	oLA	106	1565.01	-3.41%
	CSLA	152	1511.72	
CO02	oLA	148	1946.82	-2.51%
	CSLA	198	1897.92	

* oLA: Original Langley Analysis; CSLA: Langley Analysis with the new cloud screening.

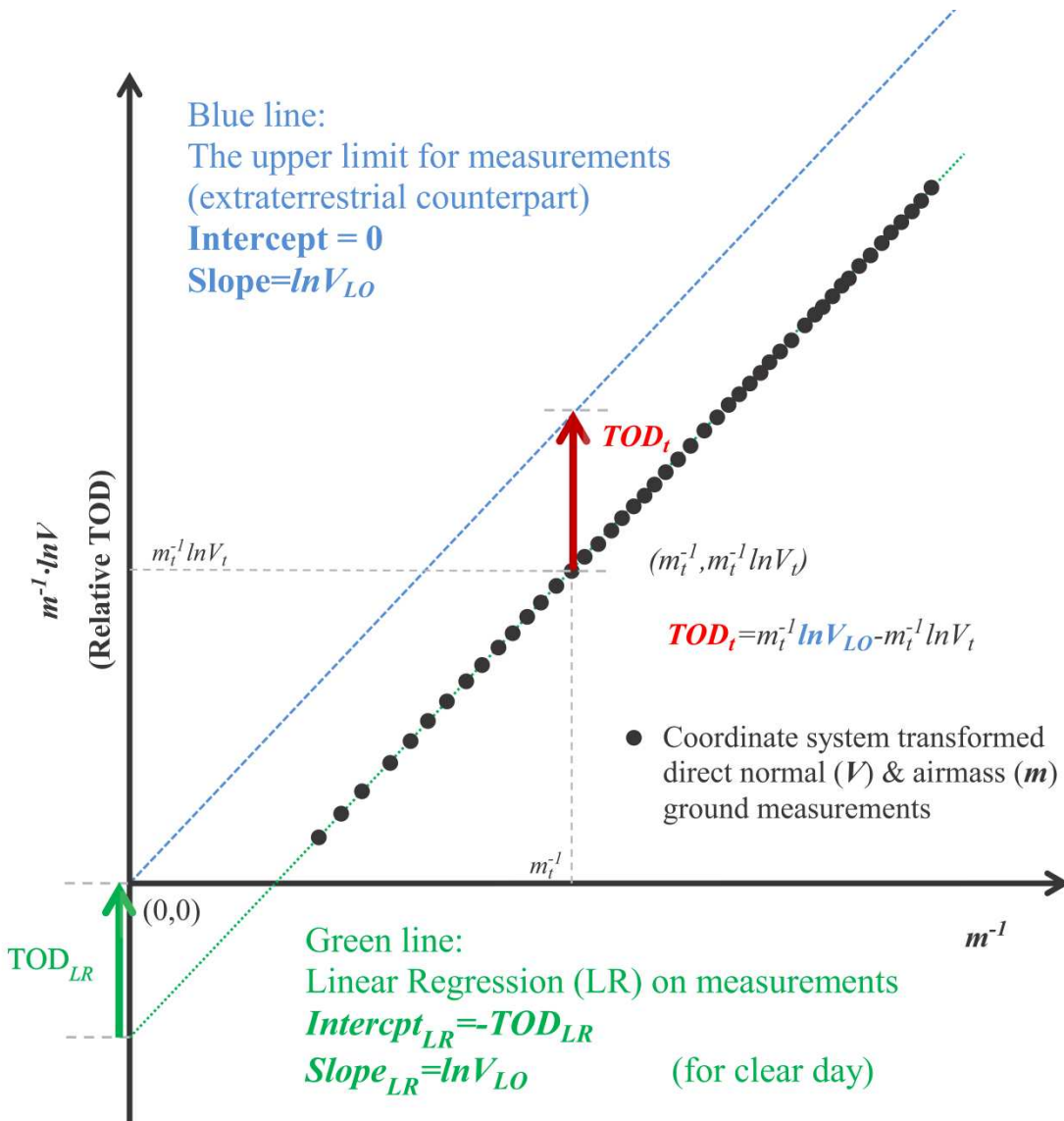


Figure 2.1 Illustration of the transformed coordinate system. The blue line can only approach the origin in the first quadrant. The black solid circles represent ground measurements under stable atmosphere.

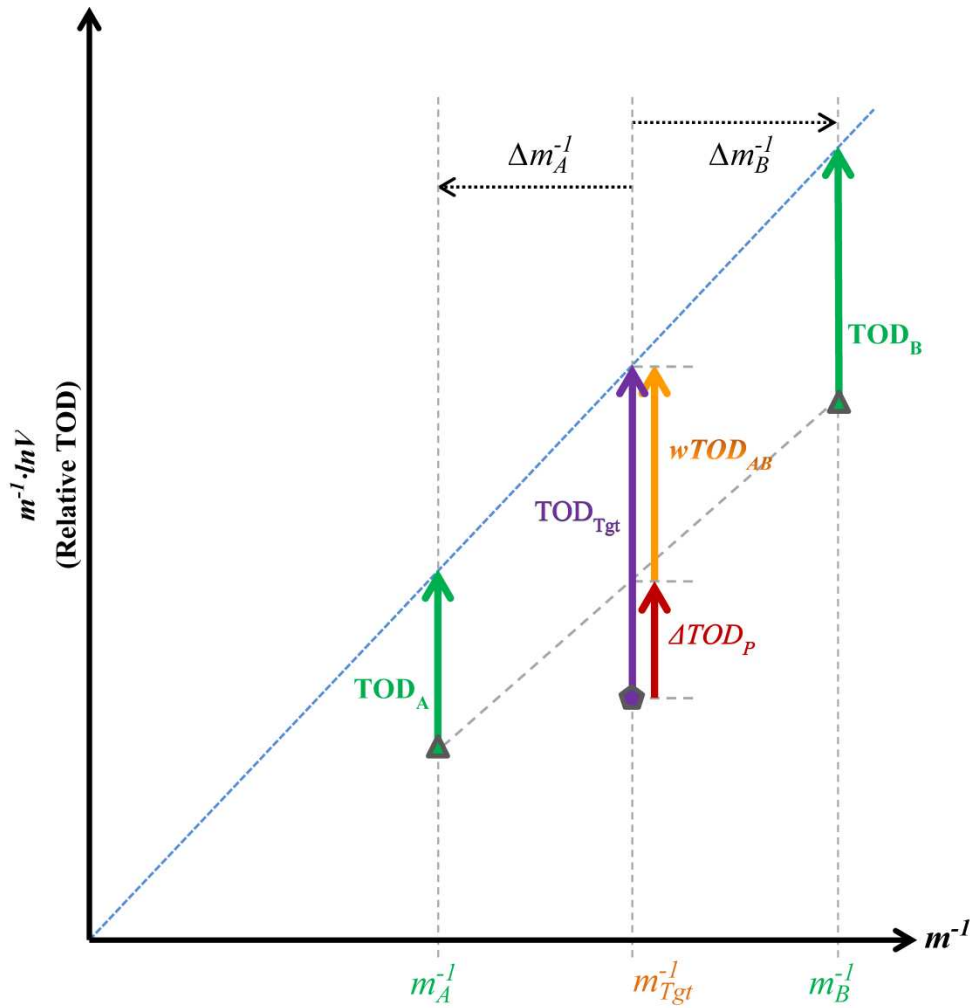


Figure 2.2 Illustration of a target point (Tgt, the purple pentagon) and one of its pair (points A and B, green triangles) in the transformed coordinate system. The blue line approaching the origin has the same meaning as the blue line in Figure 2.1.

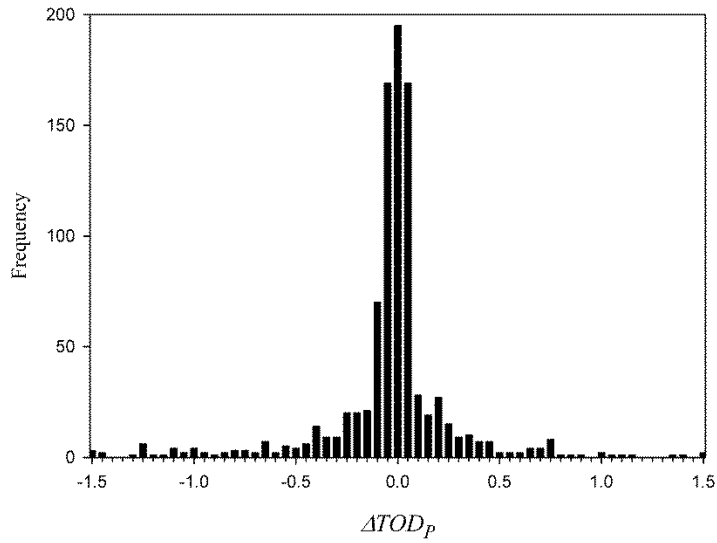


Figure 2.3 An example of the histogram of ΔTOD_p for a certain target point at a certain iteration step. The x axis is ΔTOD_p with the bin size of 0.05. The y axis is the frequency (number of cases) of the target's pairs' ΔTOD_p falling into the bins.

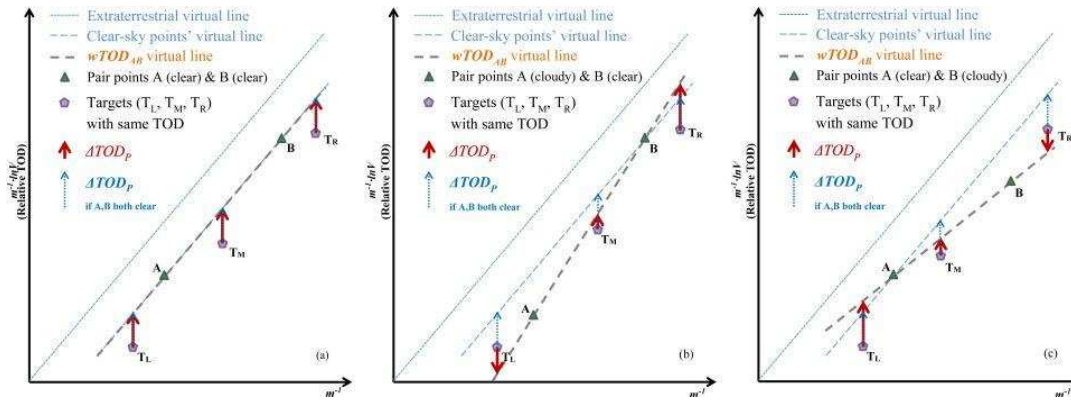


Figure 2.4 Illustrates of the effect of pair points' cloudiness in calculating ΔTOD_p . The subplot (a) represents the case when both pair points (A and B) are clear. The subplot (b) represents the case when pair point A (left) is cloudy and pair point B (right) is clear. The subplot (c) represents the case when pair point A (left) is clear and pair point B (right) is cloudy.

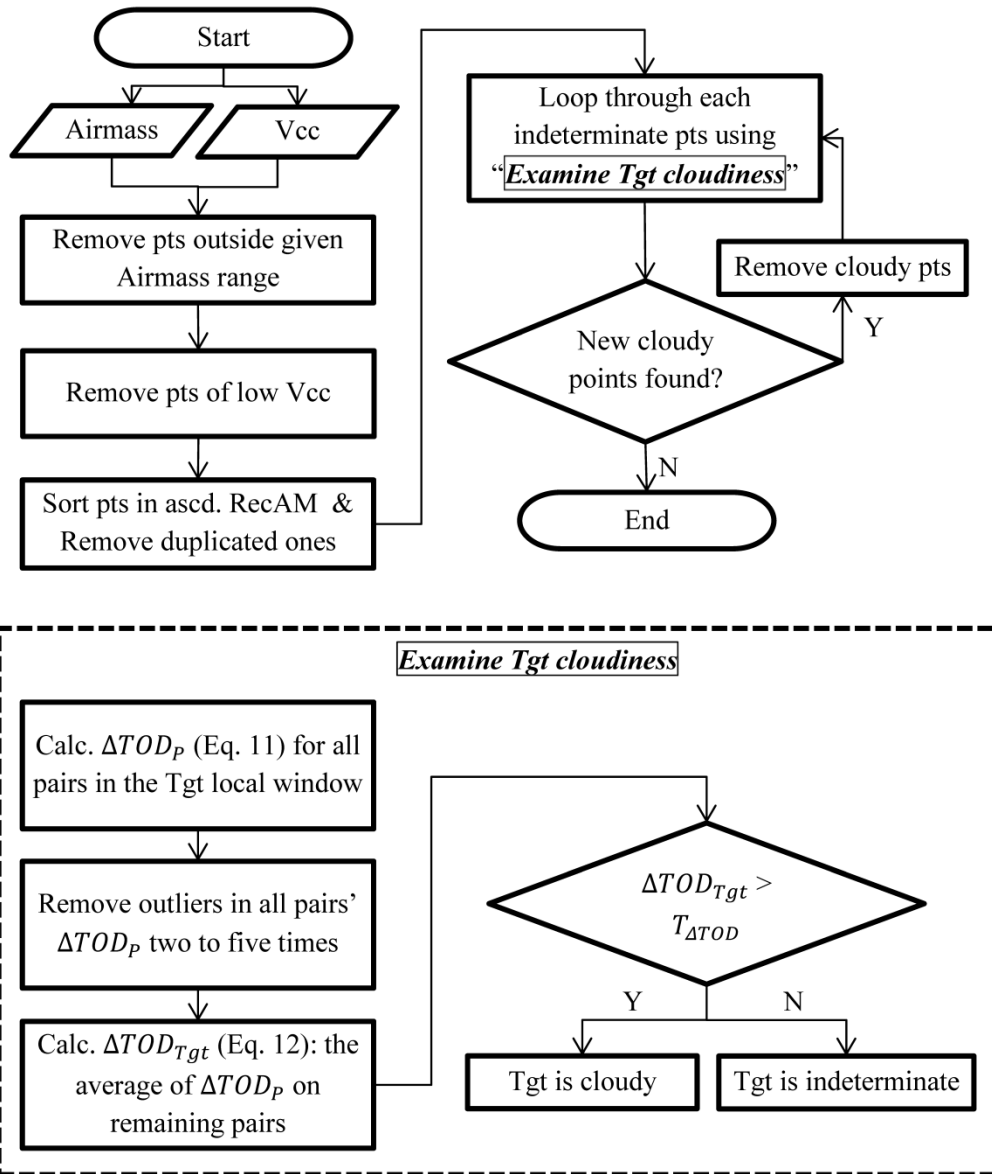


Figure 2.5 The flowchart of the new TOD pairing cloud screening algorithm. The details of the process “Examine Tgt Cloudiness” is presented separately in the box below with a dashed outline. “Vcc” stands for the cosine corrected voltage. “ascd.” stands for ascending. “RecAM” stands for the reciprocal of airmass.

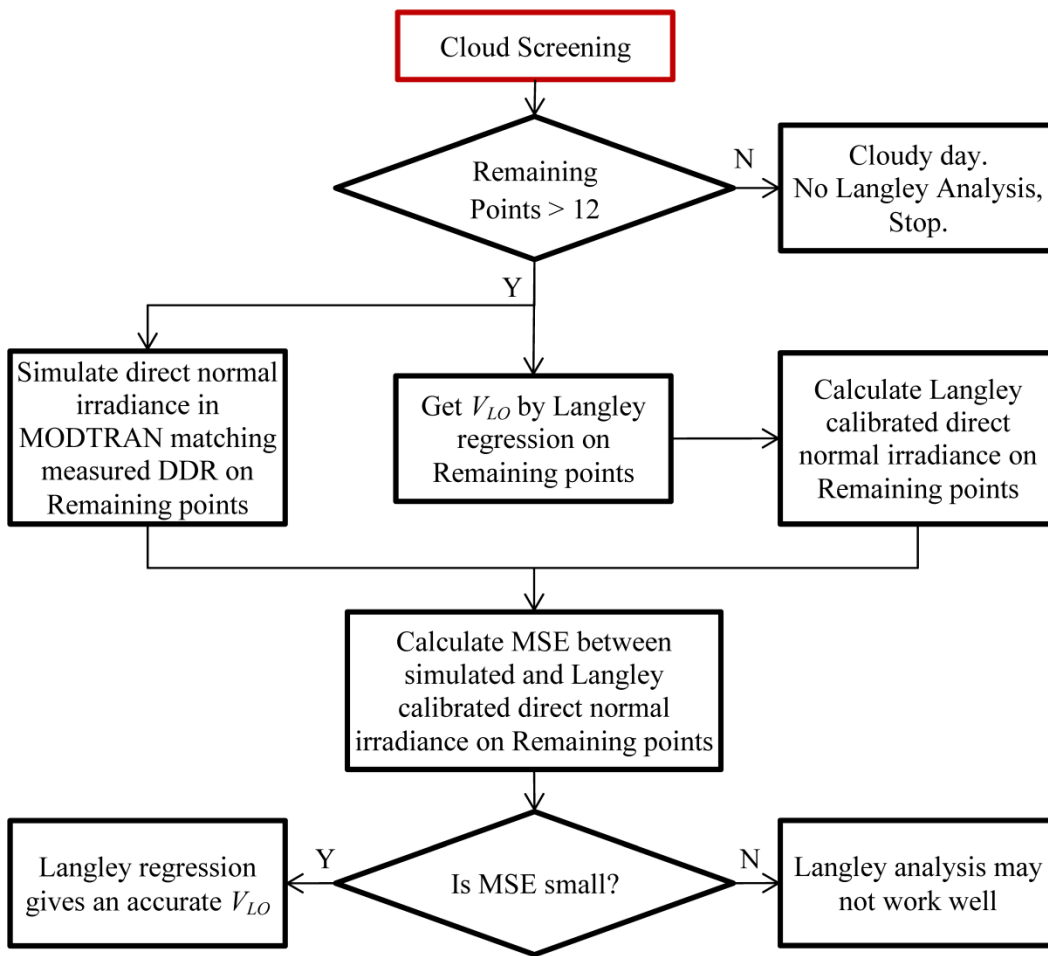


Figure 2.6 Schematic diagram of validation of cloud screening performance via comparing direct normal irradiances from Langley analysis and the radiative transfer model (MODTRAN).

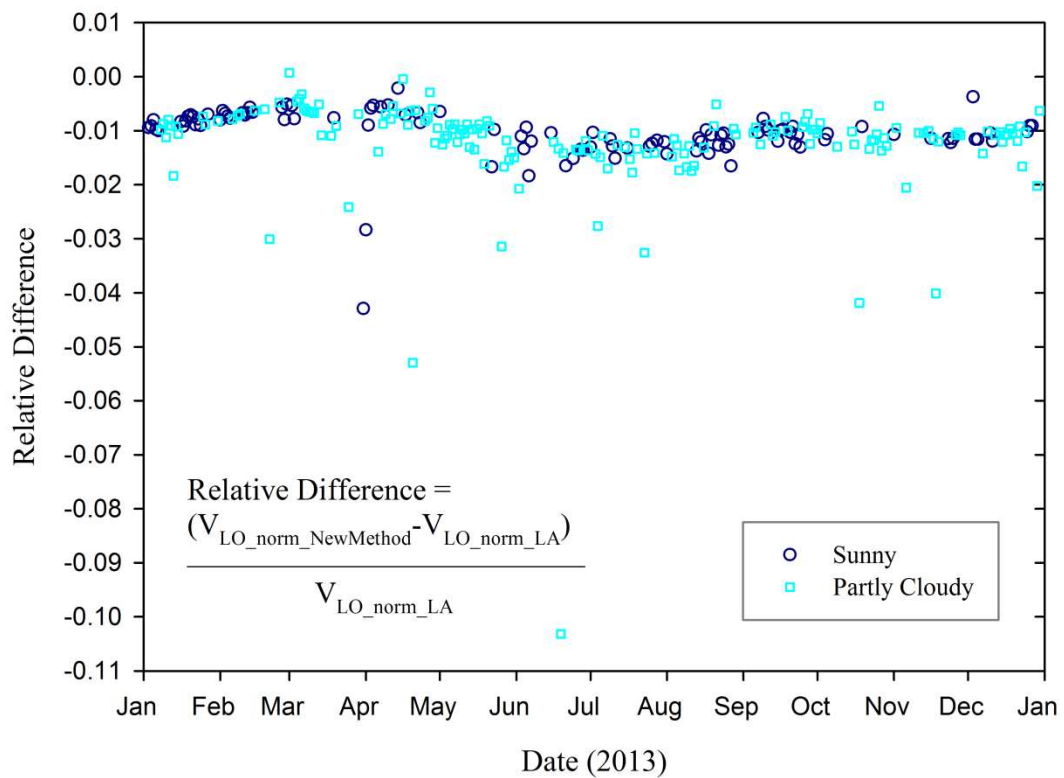


Figure 2.7 The relative differences of daily V_{LO} (sun-earth distance factor normalized) between values derived from linear regression of Eq.(2.2) on the points passing the new cloud screening algorithm and those from the original Langley analysis at 368nm channel at Mauna Loa, HI in 2013.

FL02 368nm V_{o_norm} (LA vs New method)

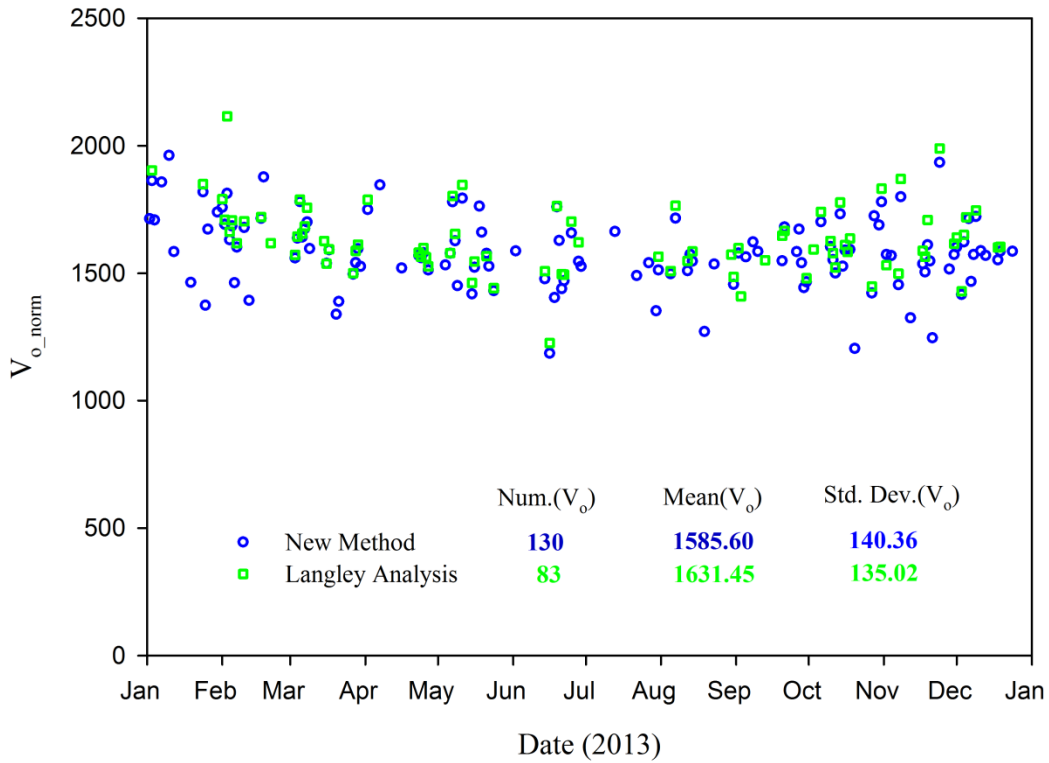


Figure 2.8 V_{o_norm} s (defined as V_{LO} normalized by a sun-earth distance factor) from the original Langley analysis (green squares) and those from the linear regression of the points passing the new cloud screening algorithm (blue circles) at 368nm channel at Homestead, FL (FL02) in 2013.

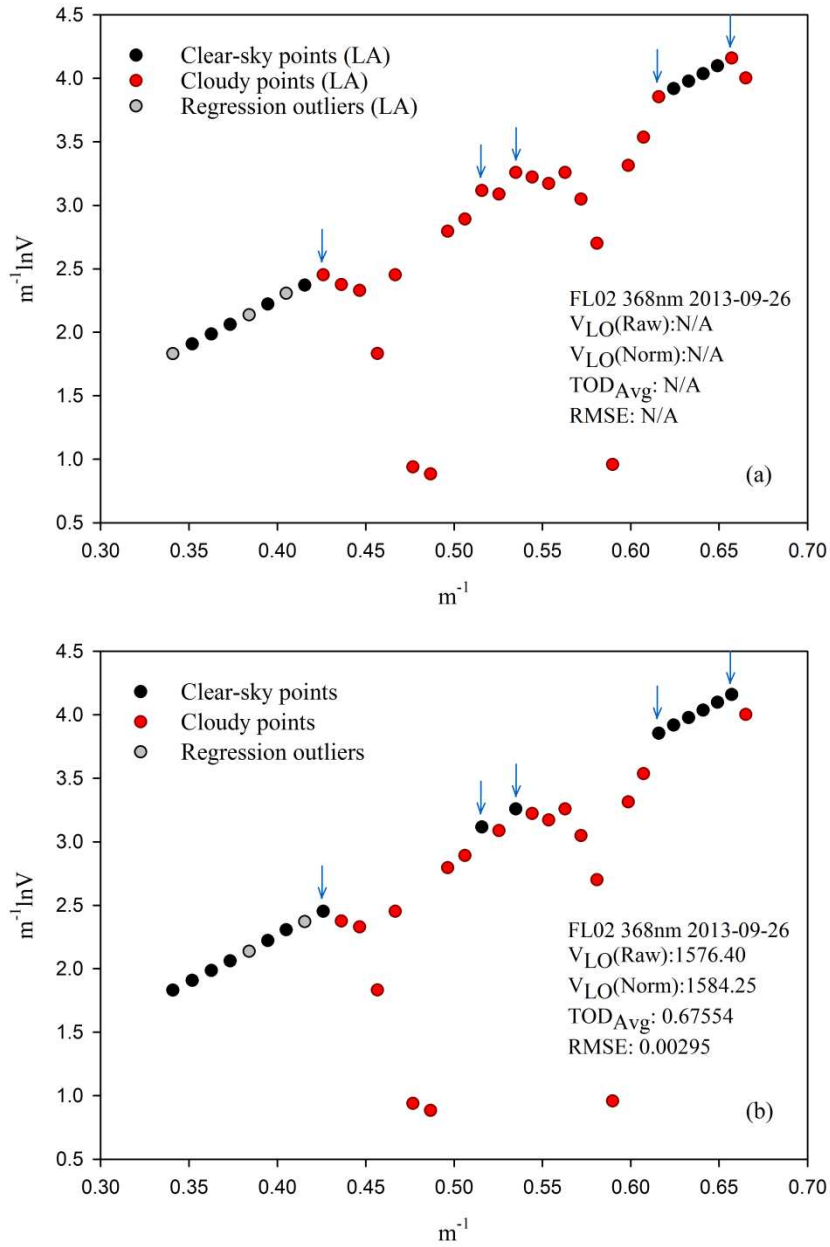


Figure 2.9 An example of the cloud screening performance of the original Langley analysis (subplot a) and the new method (subplot b) at FL02 site on Sep 26, 2013.

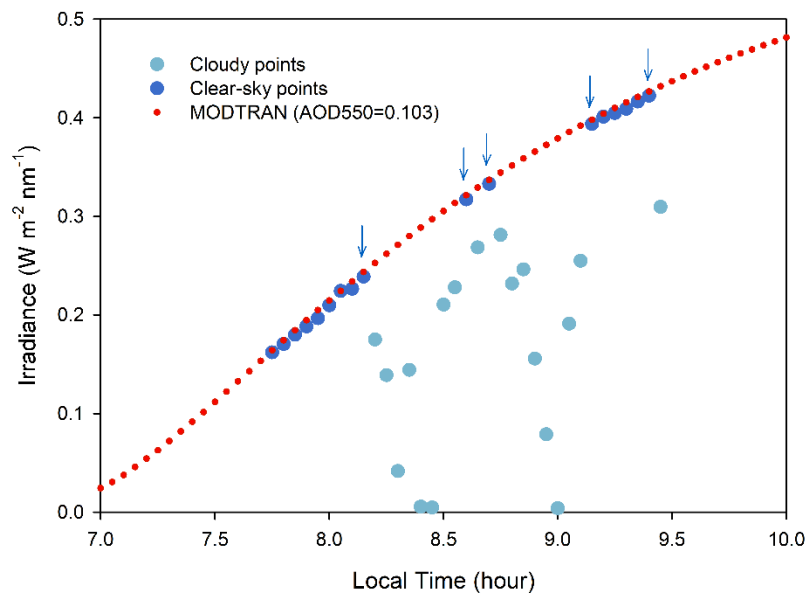


Figure 2.10 MODTRAN simulated and the new method calibrated direct normal irradiance at FL02 on 26 September 2013. Points indicated by the arrows are the additional points characterized as clear by the new algorithm.

REFERENCES

- Alexandrov M D, Marshak A, Cairns B, Lacis A A, Carlson B E (2004), Automated cloud screening algorithm for MFRSR data. *Geophys. Res. Lett.*, 31: L04118. doi:10.1029/2003GL019105
- Anderson G P, Berk A, Acharya P K, Bernstein L S, Adler-Golden S M, Lee J, Muratov L (2009), Reformulated Atmospheric Band Model Method for Modeling Atmospheric Propagation at Arbitrarily Fine Spectral Resolution and Expanded Capabilities. U.S. Patent #7593835
- Berk A, Anderson G P, Acharya P K, Bernstein L S, Muratov L, Lee J, Fox M, Adler-Golden S M, Chetwynd J H, Hoke M L, Lockwood R B, Gardner J A, Cooley T W, Borel C C, Lewis P E, Shettle E P (2006), MODTRAN5: 2006 Update. *Proceeding SPIE, Algorithms and Technologies for Multispectral, Hyperspectral, and Ultraspectral Imagery XII*: 6233, 62331F. doi: 10.1117/12.665077
- Bodhaine B A., Wood N B, Dutton E G, Slusser J R (1999), On Rayleigh optical depth calculations. *J Atmos. Oceanic Technol.*, 16: 1854–1861. doi:10.1175/1520-0426(1999)016<1854:ORODC.2.0.CO;2
- Chen M, Davis J, Tang H, Ownby C, Gao W (2013), The calibration methods for Multi-Filter Rotating Shadowband Radiometer: a review. *Frontiers of Earth Science*, 7(3): 257-270. doi: 10.1007/s11707-013-0368-9
- Harrison L, Michalsky J (1994), Objective algorithms for the retrieval of optical depths from ground-based measurements. *Appl. Opt.*, 33(22): 5126-5132
- Krotkov N, Bhartia P K, Herman J, Slusser J, Labow G, Scott G, Janson G, Eck T F, Holben B (2005), Aerosol ultraviolet absorption experiment (2002 to 2004), part 1: ultraviolet multifilter rotating shadowband radiometer calibration and intercomparison with CIMEL sunphotometers. *Optical Engineering*, 44(4): 041004. doi:10.1117/1.1886818
- Lee K H, Li Z, Cribb M C, Liu J, Wang L, Zheng Y, Xia X, Chen H, Li B (2010), Aerosol optical depth measurements in eastern China and a new calibration method. *J. Geophys. Res.*, 115(D7): D00K11. doi:10.1029/2009JD012812.
- Long C N, Ackerman T P (2000), Identification of clear skies from broadband pyranometer measurements and calculation of downwelling shortwave cloud effects. *J. Geophys. Res.*, 105(D12): 15609-15626. doi: 10.1029/2000JD900077
- Madronich S (1993), The atmosphere and UV-B radiation at ground level. *Environmental UV Photobiology* (pp. 1-39). Plenum Press

Slusser J, Gibson J, Bigelow D, Kolinski D, Disterhoft P, Lantz K, Beaubien A (2000), Langley method of calibrating UV filter radiometers. *J. Geophys. Res.*, 105(D4): 4841-4849. doi: 10.1029/1999JD900451

Smirnov A, Holben B N, Eck T F, Dubovik O, Slutsker I (2000), Cloud screening and quality control algorithms for the AERONET database. *Remote Sens. Environ.*, 73(3): 337-349. doi: 10.1016/S0034-4257(00)00109-7

Stephens G (1994), *Remote Sensing of the Lower Atmosphere: An Introduction* (pp. 261-270). New York: Oxford University Press

CHAPTER 3: TWO-STAGE REFERENCE CHANNEL CALIBRATION FOR COLLOCATED UV AND VIS MULTI-FILTER ROTATING SHADOWBAND RADIOMETERS³

Introduction

Solar radiation fuels many ecosystem processes and is measured for studies of ecosystems, models used in regional and national assessments. Solar visible (VIS) radiation, especially photosynthetically active radiation (PAR), is the energy source of plants' photosynthesis. Solar UV radiation impacts live plants' photosynthesis, production, morphogenesis, and secondary metabolites (Gehrke et al. 1995; Rozema et al. 1997; Reddy et al. 2013). UV is also considered as an important abiotic factor that accelerates litter and soil organic matter decomposition in arid and semi-arid ecosystems (Parton et al. 2007; Mayer et al. 2012) and therefore has potential influence on global carbon balance (Foereid et al. 2011). It is clear that accurate measurements of solar radiation in VIS and UV regions are important for studies of terrestrial ecosystems.

The U.S. Department of Agriculture (USDA) UV-B Monitoring and Research Program (UVMRP, or the UV-B program) has been measuring solar UV and VIS radiation at 37 sites across United States for over a decade (Chen et al. 2014). The UV-B program uses both UV and VIS versions of Multi-Filter Rotating Shadowband Radiometer (MFRSR) to observe direct normal, diffuse, and total solar radiation at 7 UV channels with 2-nm full width at half maximum

³ This chapter includes the complete published manuscript (minimal modifications were made to meet formatting requirements):

Chen M, Davis J, Sun Z, Gao W (2015), Two-stage reference channel calibration for collocated UV and VIS Multi-Filter Rotating Shadowband Radiometers. Proceeding SPIE, Remote Sensing and Modeling of Ecosystems for Sustainability XII: 96100L. doi:10.1117/12.2185500.

(FWHM) (i.e. 300, 305, 311, 317, 325, 332, 368 nm) and at 7 VIS channels with 10-nm FWHM (i.e. unfiltered, 415, 500, 610, 665, 870, 940 nm) (Bigelow et al. 1998). The measurements (voltages) are made every 12 seconds and the 3-minute average values are stored in the UV-B program database (Bigelow et al. 1998).

To calibrate two MFRSRs in-situ, the UV-B program uses the Langley method as set forth in an algorithm described in Langley Analysis (LA) (Bigelow et al. 1998; Harrison and Michalsky 1994). Langley Analysis is based on Beer's Law:

$$V_t = V_{LO} \exp(-\tau_{Total,t} \cdot m_t) \quad (3.1)$$

where, m_t is the airmass at time t, v_t is the cosine corrected voltage of the direct beam at time t at one channel, V_{LO} is the corresponding voltage as if measured at the top of the atmosphere (airmass=0) and is also known as the (raw) Langley voltage offset, and $\tau_{Total,t}$ (TOD_t) is the total optical depth (TOD in nadir direction) at time t. For N measured (m_t, V_t) pairs, there are N equations [a set of Eq. (3.1)] and $N+1$ unknown variables in the equation set, namely N of time variables TOD_t and one V_{LO} . Without additional information or simplification, it is an underdetermined linear system with no solution. LA assumes that all measurement pairs not eliminated by cloud screening have the same total optical depth (TOD). If the assumption holds and the N pairs survive the cloud screening, the number of unknown variables is reduced from $N+1$ to two and the system has an approximate solution by linear regression when $N > 2$.

To avoid violating this assumption, cloudy measurements are excluded in LA because they usually have higher and more variable TOD values than clear-sky measurements. The measured (m_t, V_t) pairs are screened with two types of cloud screening algorithms. Both types determine a point's cloudiness by examining the magnitude of its signal drop (or the TOD

increase), but the first type compares the target point to the local reference points (Chen et al. 2013), while the second type compares the target point to the global reference points (Chen et al. 2014).

Cloud-free conditions contain the clear-sky condition and the hazy condition. Under the hazy condition, TOD values may change significantly and may not be detected especially if the change is monotonic. Therefore, successful screening of cloudy points does not guarantee the validity of the same TOD assumption in LA.

TOD is the sum of atmospheric constituents' optical depths including Rayleigh optical depth (ROD), aerosol optical depth (AOD), ozone optical depth (OZOD), and water vapor optical depth (WVOD). Alexandrov et al. (2002) found that the conventional Langley technique does not yield accurate results when AOD is changing systematically during the calibration period. The variation of other atmospheric components may also contribute significantly to TOD instability (e.g. OZOD in the UVB channels and WVOD in the 940 nm channel). Because the components of optical depth may change, cloud-free points may still have systematic variation in TOD while they are aligned to a line in the Langley plot. Changing TOD significantly affects LA (Figure 3.1). The figure shows the results of the LA on two adjacent days at the Pawnee, Colorado site (the UV-B program site code: CO02) giving contrasting V_{LO} results at 368 nm channel: 3025.7 mV on 18 August and 1950.2 mV on 19 August (both in 2012). If the radiometer functions normally, it is expected that the long term trend of V_{LO} is relatively stable (Figure 3.2) and the valid Langley Analysis in the deployment period gives close V_{LO} . The contrasting V_{LO} suggests that the points for LA have monotonic variation in TOD values in at least one of these two days. It is also observed that the same MFRSR deployed at the site of high

latitude and extensive clear sky shows much more stable time series of V_{LO} than when it is deployed at the site of low latitude (data not presented).

To avoid violating the Langley Analysis assumption and to improve the accuracy of V_{LO} in all (UV-) MFRSR channels, a two-stage calibration algorithm for a pair of collocated UV-MFRSR and VIS-MFRSR is tested. In the first stage, the calibration of a special channel is performed using both the direct normal and diffuse horizontal measurements using a radiative transfer model. In the second stage, the calibration modifies the original Langley Analysis by selecting its participating points with stable TOD values in the adjacent calibrated channel(s).

Method

The 368 nm channel

In all UV and VIS MFRSR channels, the 368 nm and 870 nm channels are special in that OZOD and WVOD are negligible and aerosol is the only main source of optical depth variation in these two channels. Alexandrov et al. (2002) uses the direct-diffuse ratio and Mie theory to retrieve aerosol optical depths and the calibration coefficient at 870 nm channel. In this study, the UV-MFRSR 368 nm channel is chosen because its effective wavelength is in the middle of all channels and the error propagation from such channel to the most distant channel in UVB region may be smaller.

For a given day, the cloud screening algorithm described by Chen et al. (2014) is applied on the 368 nm channel. If the number of remaining points is less than 12, it is very likely that there are not enough clear sky points as reference points for a reliable cloud screening result. In such case, the entire day is considered as cloudy and no Langley Analysis on that day is

performed. Otherwise, applying Langley Analysis on the cloud-free points gives the $V_{LO,368,d}$ (i.e. the estimated V_{LO} at 368 nm channel in the day d).

The next step is to evaluate how the assumption of LA, the participating points having the same total optical depth, is met in the dataset.

The direct diffuse ratio (DDR) is defined as the ratio between direct normal and downward diffuse irradiances. The surface DDR can be calculated by the ratio of (UV-) MFRSR's direct normal voltage and diffuse voltage since the numerator and the denominator of DDR use the same multiplier V_{LO} in the conversion of radiation from voltage. A radiative transfer model [MODTRAN (<http://modtran5.com/>, Anderson et al. 2009; Berk et al. 2006) or TUV (<https://www2.acom.ucar.edu/modeling/tropospheric-ultraviolet-and-visible-tuv-radiation-model>, Madronich 1993)] is used to create the look-up table of DDR with respect to SZA and AOD at the 368 nm channel. With the measured DDR and SZA and the look-up table mentioned above, the 368-nm-channel AOD on each cloud-free point ($AOD_{t,368,M}$) is inversely determined.

Alexandrov et al. (2002) pointed out that the optical depths inverted from DDR and those derived from direct beam do not match, but the discrepancy between them is stable. This means that if the inversely found AODs from DDRs are stable, the direct beam AODs are stable. Since AOD is the dominant contributor to the variation of TOD at 368 nm channel, it also means the direct beam TODs at 368 nm channel are stable. Therefore, the linear regression between

$AOD_{t,368,M}$ and m_t^{-1} on all cloud-free points in day d is performed. The slope of such linear regression ($Slp_{d,368}^{AOD}$) indicates the stability of TOD at 368 nm channel at day d . The collection of

$Slp_{d,368}^{AOD}$ in the same deployment period is Slp_{368}^{AOD} . A close-to-zero value of $Slp_{d,368}^{AOD}$ indicates the cloud-free points in the day have very close $AOD_{t,368,M}$, the TOD stability requirement of the

Langley Analysis is likely to be met, and $V_{LO,368,d}$ given by the Langley Analysis is likely to be accurate.

The original time series $V_{LO,368}$ and the corresponding Slp_{368}^{AOD} are obtained by applying the procedure described above in the same deployment period day by day. $V_{LO,368}$ may show large uncertainty due to the possibility of monotonic TOD variation in cloud-free points. A moving average smoothing with the weight ($W_{d,368}$) derived from $Slp_{d,368}^{AOD}$ is implemented to obtain $V_{LO,368}^{sm}$ (the smooth time series of $V_{LO,368}$). The moving window size is two months in this study. One way of transforming $Slp_{d,368}^{AOD}$ into $W_{d,368}$ of range [0, 1] is expressed as

$$W_{d,368} = 1 - \frac{\ln |Slp_{d,368}^{AOD}| - \min(\ln |Slp_{368}^{AOD}|)}{\max(\ln |Slp_{368}^{AOD}|) - \min(\ln |Slp_{368}^{AOD}|)} \quad (3.2)$$

where, $\ln(*)$ is the natural logarithm of the input and $|*|$ is the absolute value of the input.

The idea of evaluating the accuracy of Langley Analysis with the assistance of MODTRAN in one day is presented in Figure 3.3.

The uncertainty of $V_{LO,368}^{sm}$ ($\Delta_{368}^{V_{LO}}$) is estimated by the following equation:

$$\Delta_{368}^{V_{LO}} = \frac{\sigma((V_{LO,368} - V_{LO,368}^{sm}) \cdot W_{368})}{\mu(V_{LO,368}^{sm})} \quad (3.3)$$

where, W_{368} is the collection of $W_{d,368}$ at 368 nm channel. The numerator of Eq. (3.3) is the standard deviation of the W_{368} weighted residuals between the original time series of $V_{LO,368}$ and the corresponding $V_{LO,368}^{sm}$; and the denominator of Eq. (3.3) is the mean value of $V_{LO,368}^{sm}$.

Rearranging Eq. (3.1) at 368 nm channel, the total optical depth at 368 channel is calculated by:

$$TOD_{t,368} = \frac{\ln V_{LO,368,d}^{sm} - \ln V_{t,368}}{m_t} \quad (3.4)$$

where, $V_{LO,368,d}^{sm}$ is $V_{LO,368}^{sm}$ in day d . With a given uncertainty $\Delta_{368}^{V_{LO}}$, Eq. (3.4) is modified to estimate the upper and lower limit of $TOD_{t,368}$ at time t ($TOD_{t,368}^{\pm}$):

$$\begin{aligned} TOD_{t,368}^{\pm} &= \frac{\ln\left(\left(1 \pm \Delta_{368}^{V_{LO}}\right) \cdot V_{LO,368,d}^{sm}\right) - \ln V_{t,368}}{m_t} \\ &= TOD_{t,368} + \frac{\ln\left(1 \pm \Delta_{368}^{V_{LO}}\right)}{m_t} \end{aligned} \quad (3.5)$$

From Eq. (3.5), the uncertainty of $TOD_{t,368}$ at time t ($\Delta_{t,368}^{TOD}$) is:

$$\begin{aligned} \Delta_{t,368}^{TOD} &= \frac{\ln\left(1 + \Delta_{368}^{V_{LO}}\right) - \ln\left(1 - \Delta_{368}^{V_{LO}}\right)}{2m_t} \\ &= \frac{\Delta_{368}^{TOD+}}{m_t} \end{aligned} \quad (3.6)$$

where, Δ_{368}^{TOD+} is the upper limit of $\Delta_{t,368}^{TOD}$:

$$\Delta_{368}^{TOD+} = \frac{\ln\left(1 + \Delta_{368}^{V_{LO}}\right) - \ln\left(1 - \Delta_{368}^{V_{LO}}\right)}{2} \quad (3.7)$$

Other channels

For channels other than the 368 nm channel, especially channels lower than 325 nm, both AOD and OZOD contribute to the variation of TOD significantly. It is possible to create a similar DDR lookup table with respect to SZA, AOD and OZOD, although it may be time consuming. However, the inverse search of AOD and OZOD from the measured DDR and SZA is ambiguous. Because it is possible that the same DDR at the same SZA can be achieved by many combinations of AOD and OZOD. Therefore, the quality of $V_{LO,\lambda}$ other than the AOD

dominated channels (e.g. 368 nm channel) cannot be evaluated by the assistance of MODTRAN without additional information.

The spectral dependence of optical properties has been found in many literatures.

For Rayleigh extinction, Bodhaine et al. (1999) developed an equation in the class of “ratio of polynomials” to calculate ROD as a function of wavelength and surface pressure. If surface pressures are available, ROD may be removed from TOD to emphasize the variation in AOD and OZOD.

The spectral dependence of aerosol extinction properties has been widely utilized. Taylor et al. (2008) imposes correlations between the retrieval parameters with an exponential function of wavelength in the retrieval of AOD in UV channels via the optimal estimation technique. Forgan (1994) hypothesized in the “General Method” that the aerosol extinction efficiency (Q_{ext}) as a function of wavelength (as well as the particle radius and the refraction index) is relatively stable over time. Alexandrov et al. (2002) uses the retrieved/optimized aerosol size parameters (i.e. the effective radius and variance) as Mie theory inputs to calculate the aerosol extinction ratios between MFRSR channels. Dubovik et al. (2000) states that aerosol optical thickness can be strongly wavelength dependent, which can be characterized by the Ångström parameter α . Chen et al. (2012) utilized the Ångström law as one of the constraints in calibration of multiple visible channels in MFRSR simultaneously.

The ozone (absorption) cross section has strong and stable correlation between wavelengths with relatively small temperature dependence (Chehade et al. 2013). The (vertical) OZOD is a function of ozone cross section and total column ozone. Among the two, ozone cross sections at all wavelengths are relatively stable over time. Therefore, a stable OZOD in one channel over a short period indicates a stable total column ozone in that period; and a stable total

column ozone suggests a stable OZOD in other channels in the same time period. The channels have to be adjacent for the inference of OZOD stability from a lower ozone cross section channel (λ_l) to a higher ozone cross section channel (λ_h) in that for the same amount of variation in total column ozone, the magnitude of OZOD variation is higher in λ_h than in λ_l . The uncertainty of extending OZOD stability is the smallest between adjacent channels.

Since the variation of TOD is mainly controlled by the sum of OZOD and AOD in the UVB region, a stable TOD in one channel may result from a combination of varying ozone amounts and aerosol loadings. The change of AOD between wavelengths is usually smaller than that of OZOD in the UVB region, but the aerosol type change could cause quite large TOD uncertainty in target channel. If the TODs in two channels are both stable, it is more likely that ozone and aerosol are both stable as well. Therefore, in the UVB region, the high stability of TOD in two channels may further constrain the uncertainty in inferring the high stability of TOD in the third adjacent channel. In wavelengths where only AOD controls TOD variation, the high stability of TOD in one channel may be sufficient.

With the constraints of spectral dependence discussed above, one solution for calibrating channels other than the 368 nm channel is to use one or two well calibrated adjacent channel(s) as the reference channel(s) [RC(s)] to select the points that are most clustered within a small TOD range at each RC simultaneously. If the number of the most clustered points (MCP) in the RC(s) in the day is sufficient (e.g. more than 12), a standard Langley regression is performed on those points in the adjacent target channel (TC) and the $V_{LO,\lambda_{TC},d}$ for the day d is determined. By applying the procedure day by day, the time series of $V_{LO,\lambda_{TC}}$ is obtained. The following smoothing process on $V_{LO,\lambda_{TC}}$ produces the smooth and continuous time series of $V_{LO,\lambda_{TC}}^{sm}$. Once the

$\Delta_{\lambda_{TC}}^{TOD+}$ is determined, the target channel's calibration is finished and it can serve as a reference channel to calibrate its adjacent channels.

The idea for estimating the uncertainties at 368 nm channel [i.e. Eq. (3.3) to Eq. (3.7)] can be extended to other channels with slight modification.

Let $V_{LO,\lambda}$ and $V_{LO,\lambda}^{sm}$ be the time series of V_{LO} at channel λ before and after smoothing. The uncertainty of $V_{LO,\lambda}^{sm}$ ($\Delta_{\lambda}^{V_{LO}}$) is estimated by the following equation:

$$\Delta_{\lambda}^{V_{LO}} = \frac{\sigma(V_{LO,\lambda} - V_{LO,\lambda}^{sm})}{\mu(V_{LO,\lambda}^{sm})} \quad (3.8)$$

where, $\sigma(*)$ and $\mu(*)$ are the standard deviation and the mean of a given vector. The difference between $\Delta_{\lambda}^{V_{LO}}$ and $\Delta_{368}^{V_{LO}}$ is that Eq. (3.8) does not have the weight term (W_{368}) as in Eq. (3.3) due to the ambiguity in retrieving AOD and OZOD from DDR.

Rearranging Eq. (3.1) at channel λ , the total optical depth at channel λ is calculated by:

$$TOD_{t,\lambda} = \frac{\ln V_{LO,\lambda,d}^{sm} - \ln V_{t,\lambda}}{m_t} \quad (3.9)$$

where, $V_{LO,\lambda,d}^{sm}$ is $V_{LO,\lambda}^{sm}$ in day d .

Similar to Eq. (3.6), for a determined $\Delta_{\lambda}^{V_{LO}}$, the uncertainty of $TOD_{t,\lambda}$ at time t ($\Delta_{t,\lambda}^{TOD}$) is:

$$\begin{aligned} \Delta_{t,\lambda}^{TOD} &= \frac{\ln(1 + \Delta_{\lambda}^{V_{LO}}) - \ln(1 - \Delta_{\lambda}^{V_{LO}})}{2m_t} \\ &= \frac{\Delta_{\lambda}^{TOD+}}{m_t} \end{aligned} \quad (3.10)$$

where, Δ_{λ}^{TOD+} is the upper limit of $\Delta_{t,\lambda}^{TOD}$:

$$\Delta_{\lambda}^{TOD+} = \frac{\ln(1 + \Delta_{\lambda}^{V_{LO}}) - \ln(1 - \Delta_{\lambda}^{V_{LO}})}{2} \quad (3.11)$$

Pseudo code

The summary of the algorithm is presented in the pseudo code below. The algorithm is suitable for all narrow-band channels of UV-MFRSR and MFRSR (except for the 940 nm channel) in the same deployment period at the same site.

1. [Calib1] Calibrating the 368 nm channel:

Loop (dates, subscript: d) {

- a. Applying the cloud screening algorithm developed by Chen et al. (2014) on the measurement points $(m_t, V_{t,368})$ in day d .
 - b. Performing Langley Analysis (LA) on cloud-free points at 368 nm channel in day d and generating $V_{LO,368,d}$ for day d ;
 - c. Using the lookup table of DDR with respect to SZA and AOD at 368 nm channel created in MODTRAN to evaluate the quality ($Slp_{d,368}^{AOD}$) of $V_{LO,368,d}$;
- }
- d. Collecting $V_{LO,368}$ from $V_{LO,368,d}$ in all dates;
 - e. Collecting Slp_{368}^{AOD} from $Slp_{d,368}^{AOD}$ in all dates and transforming them into the weighting vector W_{368} with the range of [0, 1] [Eq. (3.2)];
 - f. Applying the (W_{368}) weighted moving average smoothing (window size: 61-day) on $V_{LO,368}$ to determine the smooth and continuous time series $V_{LO,368}^{sm}$ in all dates;
 - g. Estimating the uncertainty of $V_{LO,368}^{sm}$ [$\Delta_{368}^{V_{LO}}$, Eq. (3.3)] and the upper limit of the uncertainty of $TOD_{t,368}$ [Δ_{368}^{TOD+} , Eq. (3.7)].

2. [Calib2] Calibrating the target channel (TC or λ_{TC}) from one adjacent reference channel

(RC or λ_{RC}):

a. Setting the half of the allowed TOD range in search of the most clustered points

$$\text{in RC: } \gamma_{\lambda_{RC}} = 0.5 \times \Delta_{t, \lambda_{RC}}^{TOD} ;$$

Loop (dates, subscript: d) {

Loop (time, subscript: t) {

b. Calculating the total optical depth at RC at time t ($TOD_{t, \lambda_{RC}}$, 3-minute

interval) using Eq. (3.9) and the current day's $V_{LO, \lambda_{RC}, d}^{sm}$;

}

Loop (time, subscript: t) {

c. Finding the points set (P_t) in the day with their total optical depth at RC

in the range of $[TOD_{t, \lambda_{RC}} - \gamma_{\lambda_{RC}}, TOD_{t, \lambda_{RC}} + \gamma_{\lambda_{RC}}]$;

d. Recording the number of points of P_t in C_t ;

e. Optionally, Finding the airmass range (AMR_t) of P_t and updating C_t

with $C_t = C_t \times AMR_t$;

}

f. Finding the highest C_t and calling the corresponding points set (P_t) the most clustered points for day d : MCP ;

g. Performing Langley Analysis (LA) on MCP at the target channel and

generating $V_{LO, \lambda_{TC}, d}$ for day d ;

}

- h. Applying the moving average smoothing (window size: 61-day) on $V_{LO,\lambda_{TC}}$ to determine the smooth and continuous time series $V_{LO,\lambda_{TC}}^{sm}$ in all dates;
- i. Estimating the uncertainty of $V_{LO,\lambda_{TC}}^{sm}$ [$\Delta_{\lambda_{TC}}^{V_{LO}}$, Eq. (3.8)] and the upper limit of the uncertainty of $TOD_{t,\lambda_{TC}}$ [$\Delta_{\lambda_{TC}}^{TOD+}$, Eq. (3.11)].
3. [Calib3] Calibrating the target channel (TC or λ_{TC}) from two adjacent reference channels ([RC1 and RC2] or [λ_{RC1} and λ_{RC2}]):
- a. Setting the half of the allowed TOD range in search of most clustered points in RC1: $\gamma_{\lambda_{RC1}} = 0.5 \times \Delta_{t,\lambda_{RC1}}^{TOD}$ and in RC2: $\gamma_{\lambda_{RC2}} = 0.5 \times \Delta_{t,\lambda_{RC2}}^{TOD}$;
- Loop (dates, subscript: d) {
- Loop (time, subscript: t) {
- b. Calculating the two total optical depths at RC1 and RC2 at time t ($TOD_{t,\lambda_{RC1}}$ and $TOD_{t,\lambda_{RC2}}$) using Eq. (3.9) and the current day's $V_{LO,\lambda_{RC1},d}^{sm}$ and $V_{LO,\lambda_{RC2},d}^{sm}$;
- }
- Loop (time, subscript: t) {
- c. Finding the points set (P_t) in the day with their total optical depth at RC1 in the range of $[TOD_{t,\lambda_{RC1}} - \gamma_{\lambda_{RC1}}, TOD_{t,\lambda_{RC1}} + \gamma_{\lambda_{RC1}}]$ and their total optical depth at RC2 in the range of $[TOD_{t,\lambda_{RC2}} - \gamma_{\lambda_{RC2}}, TOD_{t,\lambda_{RC2}} + \gamma_{\lambda_{RC2}}]$, simultaneously;
- d. Recording the number of points of P_t in C_t ;

- e. Optionally, Finding the airmass range (AMR_t) of P_t and updating C_t with $C_t = C_t \times AMR_t$;
- }
- f. Finding the highest C_t and calling the corresponding points set (P_t) the most clustered points for day d : MCP ;
 - g. Performing Langley Analysis (LA) on MCP at the target channel and generating $V_{LO,\lambda_{TC},d}$ for day d ;
- }
- h. Applying the moving average smoothing (window size: 61-day) on $V_{LO,\lambda_{TC}}$ to determine the smooth and continuous time series $V_{LO,\lambda_{TC}}^{sm}$ in all dates;
 - i. Estimating the uncertainty of $V_{LO,\lambda_{TC}}^{sm}$ [$\Delta_{\lambda_{TC}}^{V_{LO}}$, Eq. (3.8)] and the upper limit of the uncertainty of $TOD_{t,\lambda_{TC}}$ [$\Delta_{\lambda_{TC}}^{TOD+}$, Eq. (3.11)].

In this study, the calibration procedure of all UV- and VIS-MFRSR narrow band channels at one site follows the sequence in Figure 3.4. At the beginning, the method “Calib1” described in the pseudo code with the assistance of the MODTRAN DDR lookup table is used to obtain the calibration coefficients ($V_{LO,368}^{sm}$) and the upper limit of TOD uncertainty (Δ_{368}^{TOD+}) at 368 nm channel. Using the 368 nm channel as the reference channel, the calibration coefficients and the upper limit of TOD uncertainty at 415 channel ($V_{LO,415}^{sm}$ and Δ_{415}^{TOD+}) are retrieved using the one reference channel method “Calib2” described in the pseudo code. So far, there are two channels calibrated with uncertainty estimates. The $V_{LO,\lambda}^{sm}$ and Δ_{λ}^{TOD+} at the rest channels are retrieved gradually using the method “Calib3” described in the pseudo code and calibration

coefficients and uncertainty estimates of two most adjacent channels that have already been calibrated ($V_{LO,\lambda_{RC1}}^{sm}$, $V_{LO,\lambda_{RC2}}^{sm}$, $\Delta_{\lambda_{RC1}}^{TOD+}$, and $\Delta_{\lambda_{RC2}}^{TOD+}$).

Results and Discussion

The new two-stage reference channel calibration algorithm was applied on the pair of UV-MFRSR and MFRSR at the UV-B program site FL02 at Homestead, Florida in the deployment period between Mar 14, 2013 and Dec 31, 2013. The original Langley Analysis results for the same site and time period were extracted from the UV-B program database. Figure 3.5 shows comparison of V_{LO} time series obtained from the original Langley Analysis and the new method at 8 (UV-) MFRSR channels. The original Langley V_{LO} (red points) have wider range than the new Langley V_{LO} (green points). There are obvious time gaps when the original Langley Analysis did not generate any V_{LO} (e.g. 34 days between Jul 2 and Aug 4 at 368 nm channel, 20 days between Jul 15 and Aug 4 at 300 nm channel, and 185 days between Jun 29 and Dec 31 at 870 nm channel). There are also time periods when the number of the original Langley V_{LO} is not sufficient to generate a reliable smooth time series (e.g. purple line, July to December at 610 nm channel). The smooth time series of the V_{LO} show large difference between the original and the new Langley methods at 300, 305 (not presented), and 870 nm channels.

Table 3.1 listed three statistics: the number of successful Langley Analysis days, the (weighted) standard deviation of the residual, and the mean relative difference, to quantitatively express the difference between the original and new Langley methods.

The standard deviation of the residual (rsd) is defined as

$$rsd = \sqrt{\frac{\sum_{i=1}^N (x_i - x_i^*)^2}{N-1}}, \quad (3.12)$$

and the weighted standard deviation of the residual (rsd_w) is defined as

$$rsd_w = \sqrt{\frac{\sum_{i=1}^N w_i (x_i - x_i^*)^2}{\frac{M-1}{M} \sum_{i=1}^N w_i}}, \quad (3.13)$$

where, N is the length of the input vector (X), x_i is the i th element of X , w_i is the corresponding weight of x_i , x_i^* is the corresponding element of the smoothed vector of X (X^*), M is number of nonzero elements in X . For example, at 415 nm channel, X is $V_{LO,415}$ and X^* is $V_{LO,415}^{sm}$; at 368 nm channel, w_i is calculated by Eq. (3.2).

The relative difference between two scalars x and y may be defined as $(x - y) / x$. The mean relative difference between two vectors (X and Y) may be calculated by the L^1 relative error norm:

$$\frac{1}{N} \sum_{i=1}^N \frac{\|x_i - y_i\|}{\|x_i\|}, \quad (3.14)$$

where, N is the length of X or Y , x_i is the i th element of X , y_i is the i th element of Y .

The No. (V_{LO}) in Table 3.1 shows that the new Langley method generated significantly more Langley V_{LO} (specifically, 1.73 to 6.86 times more or 48 to 129 more successful V_{LO} days) than the original Langley Analysis. On average, the new method generates V_{LO} every 2.6 days at 368 nm channel and every 2 day at other channels. In comparison, the original Langley Analysis generates V_{LO} every 4 to 13 days. More daily V_{LO} usually means less time gaps to be filled in the

smoothing process. As a result, it is seen in Figure 3.5 that the new method's smooth time series of V_{LO} (blue line) has less dramatic variation compared to the original Langley Analysis (purple line).

The standard deviation of V_{LO} residual in Table 3.1 shows that on average the new Langley method's daily V_{LO} is closer to its smooth value (specifically, 1.16 to 4.45 times closer) than the original Langley Analysis. In the smoothing process, V_{LO} far away from its running mean value is more likely to be excluded in the calculation of smooth time series. For example, the UV-B program currently uses two standard deviation as a threshold to exclude outliers and long V_{LO} gaps are common after the filtering. As a result, the time series of V_{LO} with higher residual standard deviation has fewer usable points to generate the smooth time series, making the smooth time series less constrained and bumpier.

The combination of more Langley V_{LO} and smaller standard deviation of V_{LO} residual means that the new Langley method generates more accurate and reliable time series of V_{LO} than the original Langley Analysis. However, the new method's performance improvement at the 368 nm channel is not as much as that at other channels. This suggests that the mechanisms behind the two calibration stages are quite different. The 368 nm channel is the starting channel for the new Langley method. There is no reference channel that can be used to find TOD stable points for Langley regression at the channel. It still rely on the cloud screening algorithm to select qualified regression points at the channel. The increase of No. (V_{LO}) from 66 to 114 is mainly due to the cloud screening algorithm developed by Chen et al. (2014) picking up more clear-sky points in short and/or transitional periods. Usually the survived points from the cloud screening algorithm have the lowest TOD values, but those points may not be the best points set for

Langley regression for two reasons: (1) those points may have systematic variation in TOD; and (2) those points may not reside in the most clustered TOD interval in the day. The MODTRAN DDR lookup table may detect the first problem (systematic TOD variation), assign a lower weight to V_{LO} violating the TOD stability assumption during the smoothing process, and improve the reliability of the smooth time series of V_{LO} . However, since there is no reference channel available for the 368 nm channel, the new method is not able to choose points in the most clustered TOD interval, missing some potential V_{LO} .

Table 3.1 also shows that the mean relative differences of the smooth V_{LO} time series between the two methods are less than 3% in the most channels except for in the 300 and 305 nm channels (i.e. 10.28% and 9.08%, respectively). This suggests that at least one of the two methods may have large systematic bias in V_{LO} . It is unclear why the large differences happened only on these two channels. The maximum relative differences of the smooth V_{LO} time series between the two methods are higher than 5% in most channels and higher than 15% in 300 and 305 nm channels.

Conclusions

The performance of original Langley Analysis method at most UV-B program sites is not as reliable as that at the Hawaii site. We attributed the variation in Langley Analysis performance to the monotonically changing total optical depths (TOD) in the cloud screened points. A new two-stage reference channel calibration method is developed for a pair of collocated UV-MFRSR and MFRSR. In the first stage, the 368 nm channel is calibrated by the Langley method with two main improvements. The first improvement is to use the cloud screening algorithm developed by

Chen et al. (2014) to include cloud-free points in short and/or transitional periods. The second improvement is to limit the influence of the Langley offset (V_{LO}) obtained from data points violating TOD stability assumption by the radiative transfer model (i.e. MODTRAN) simulation. MODTRAN is used to create the lookup table of the direct normal and diffuse horizontal ratio with respect to aerosol optical depth and solar zenith angle to evaluate the quality of V_{LO} by giving lower weights to those generated from points with monotonic variation in AOD at the 368 nm channel. With one or two calibrated channels as reference channel(s), the most stable points in the reference channel(s) were selected and Langley regression was applied on the same time points to generate V_{LO} in the adjacent un-calibrated channel. All stage-two (UV-) MFRSR channels (except for the 940 nm and unfiltered channels) were calibrated by gradually implementing this strategy. The test of this method on the UV-B program site at Homestead, Florida (FL02) showed that (1) The long-term trend of the original Langley V_{LO} is impacted by the monotonic changing AOD at the 368nm channel; and (2) more clustered and abundant V_{LO} at all channels are generated compared with the new Langley method.

Table 3.1 The statistics of V_{LO} (sun-earth distance normalized) between the original Langley Analysis (oLA) and the new method (tsrcLA) on 12 (UV-) MFRSR channels at the UV-B site FL02 during the time period between Mar. 14, 2013 and Dec. 31, 2013. The term “No. (V_{LO})” represents the number of successful Langley Analysis days. The acronym “RD” represents relative difference between two V_{LO} sources [Eq. (3.14)]. The 368 nm channel uses Eq. (3.13) to calculate the weighted standard deviation of V_{LO} residual (*), while other channels use Eq. (3.12) to calculate the standard deviation of V_{LO} residual.

Channel	V_{LO} source	No. (V_{LO})	Standard deviation of V_{LO} residual	Mean V_{LO} RD; % (Max V_{LO} RD; %)
300 nm	oLA	22	8041.19	10.28 (18.51)
	tsrcLA	151	4109.85	
305 nm	oLA	42	1629.87	9.08 (15.17)
	tsrcLA	160	701.24	
311 nm	oLA	39	410.83	2.81 (8.02)
	tsrcLA	145	126.79	
317 nm	oLA	77	111.40	1.96 (7.93)
	tsrcLA	146	37.85	
325 nm	oLA	62	163.27	2.31 (7.44)
	tsrcLA	144	36.68	
332 nm	oLA	56	150.49	2.67 (7.09)
	tsrcLA	148	37.32	
368 nm	oLA	66	119.34	1.95 (5.94)
	tsrcLA	114	102.06 *	
415 nm	oLA	26	35.75	0.97 (3.41)
	tsrcLA	155	23.71	
500 nm	oLA	42	115.81	0.90 (3.07)
	tsrcLA	148	46.82	
610 nm	oLA	49	25.58	1.38 (8.42)
	tsrcLA	159	11.11	
665 nm	oLA	60	43.40	0.89 (3.43)
	tsrcLA	165	13.07	
870 nm	oLA	58	97.40	1.77 (3.64)
	tsrcLA	159	26.68	

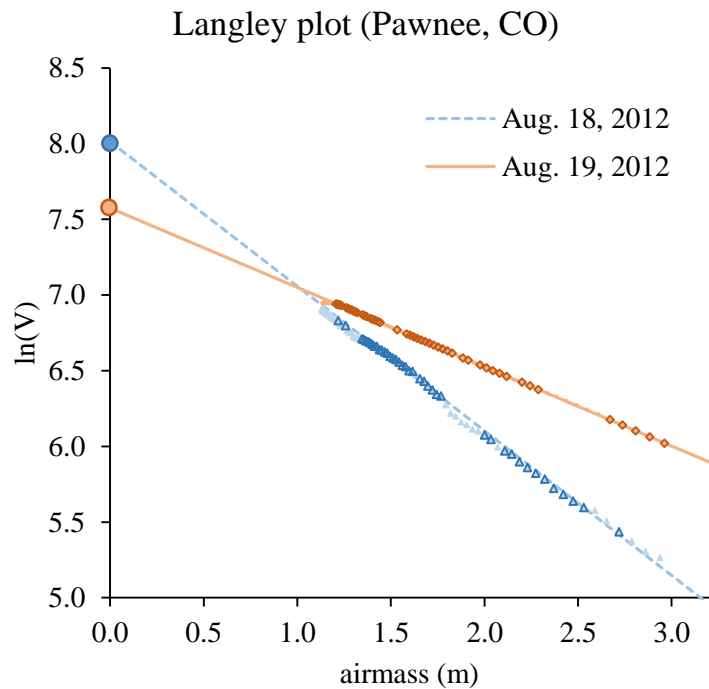


Figure 3.1 Langley plots at two adjacent days showing that systematic variation in TOD may significantly affects the accuracy of Langley V_{LO} (raw). The data are selected from the UV-B program CO2 site (Pawnee, Colorado) UV-MFRSR measurements at 368 nm channel on August 18 & 19, 2012.

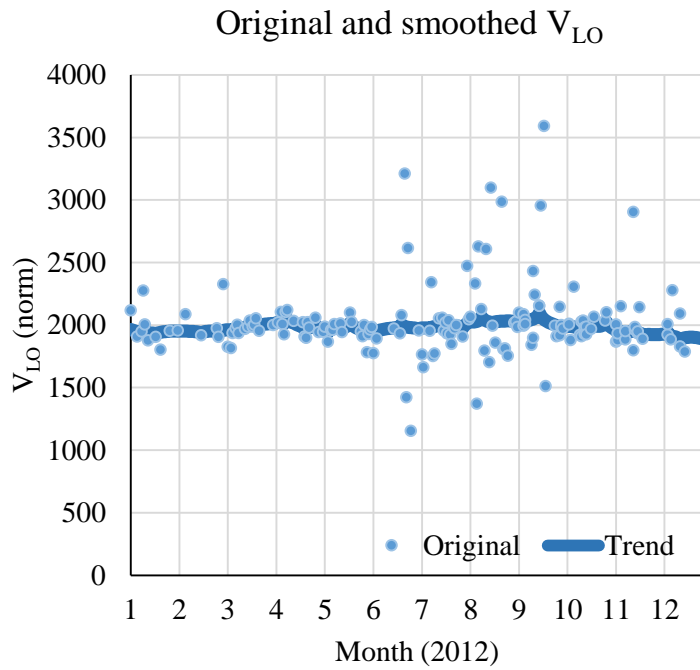


Figure 3.2 The time series of V_{LO} (sun-earth distance factor normalized) at the UV-B program CO2 site in 2012 showing relatively stable V_{LO} trend over time.

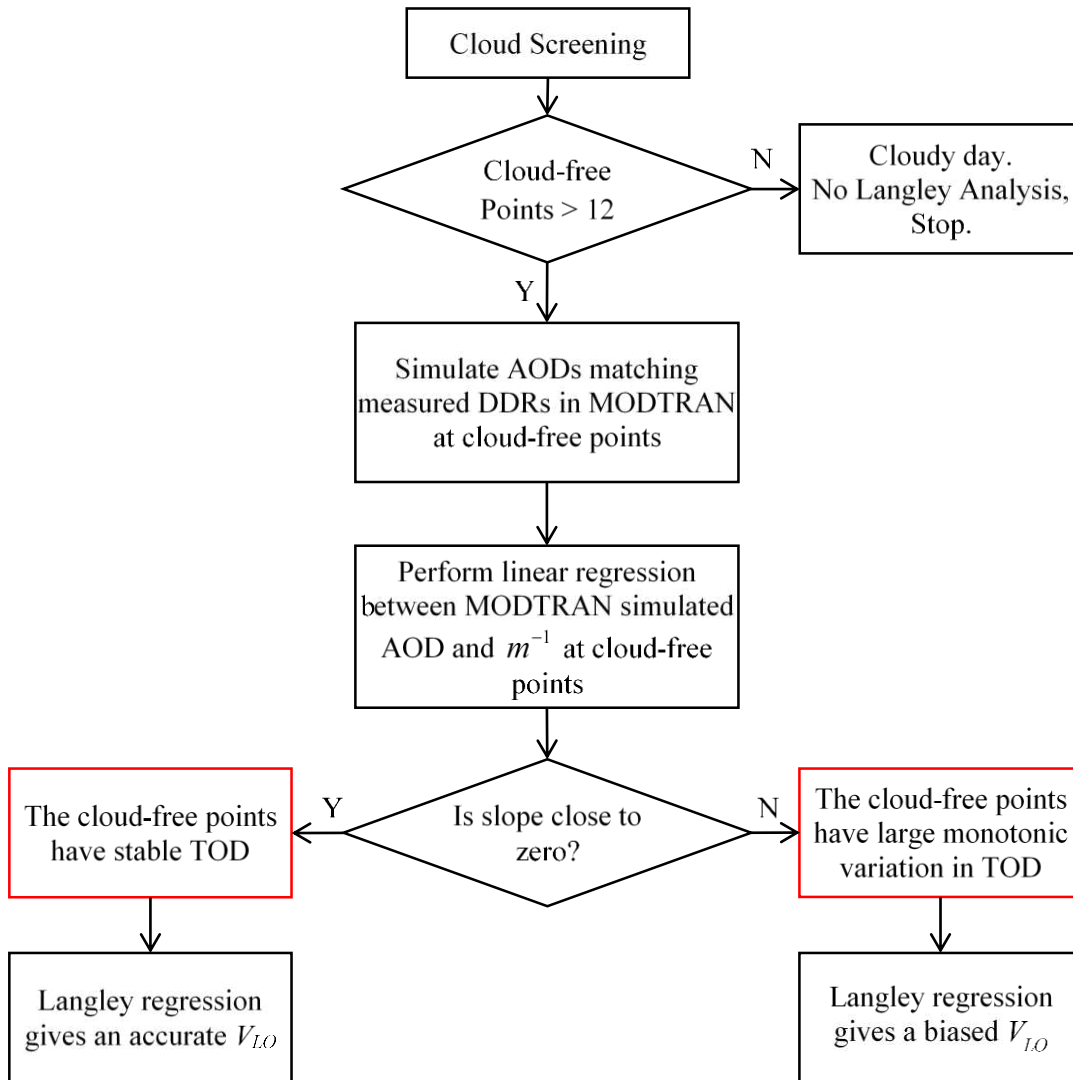


Figure 3.3 Schematic diagram of evaluation of the Langley V_{LO} accuracy at 368 channel with the assistance of the radiative transfer model MODTRAN.

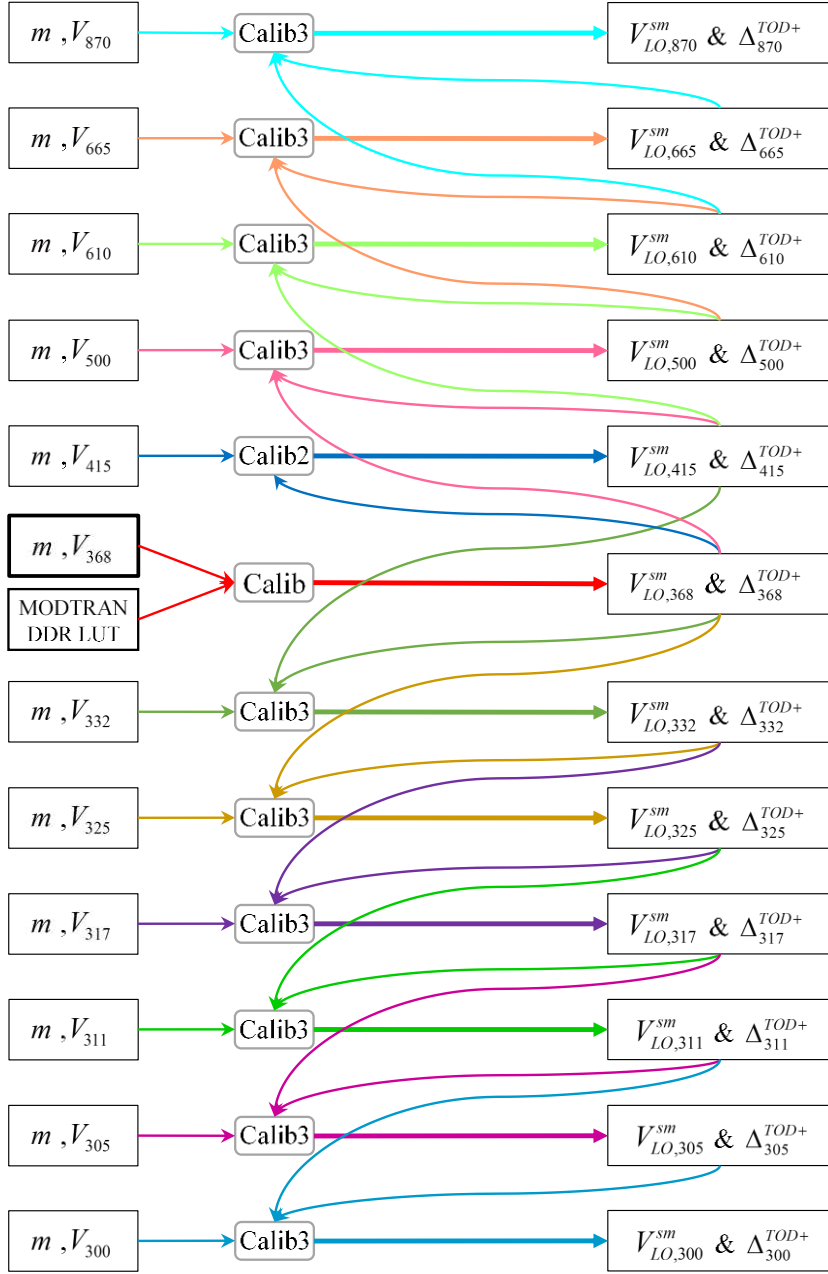


Figure 3.4 Illustration of the calibration sequence for a pair of collocated UV-MFRSR and MFRSR using the new two-stage algorithm. The phrase “MODTRAN DDR LUT” represents the direct-diffuse ratio lookup table created by the radiative transfer model MODTRAN. The details of creating the lookup table are described under the “The 368 nm channel” subsection in the “Method” section. The terms m and V_{λ} represent the measurements of air mass and cosine corrected voltage for a (UV-) MFRSR channel λ . The terms $V_{LO,\lambda}^{sm}$ and Δ_{λ}^{TOD+} represent the time series of smoothed V_{LO} and the corresponding estimated TOD uncertainty at channel λ . The phrases “Calib1”, “Calib2”, and “Calib3” represent the calibration procedures summarized in the “Pseudo code” section.

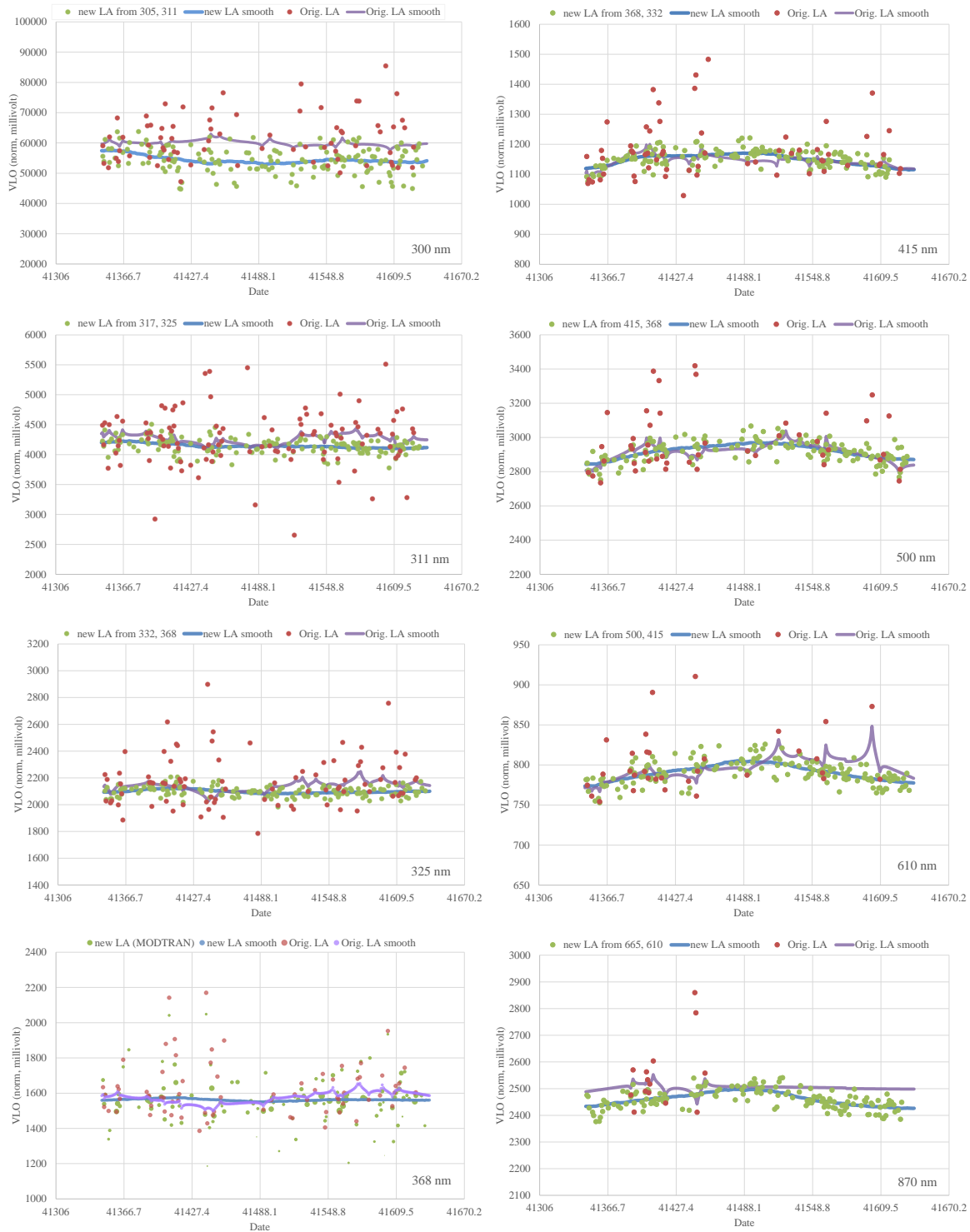


Figure 3.5 The original Langley V_{LO} time series (red), the new Langley V_{LO} time series (green), and their smooth time series (purple and blue lines) at 300, 311, 325, 368, 415, 500, 610, and 870 channels at the UV-B program FL02 site in 2013. The channel labels are presented at the right-bottom corner of each subplot. The V_{LO} is sun-earth distance normalized in unit millivolt.

REFERENCES

- Alexandrov M D, Lacis A A, Carlson B E, Cairns B (2002), Remote sensing of atmospheric aerosols and trace gases by means of multifilter rotating shadowband radiometer. Part I: Retrieval algorithm. *Journal of the Atmospheric Sciences* 59(3): 524-543. doi: 10.1175/1520-0469(2002)059<0524:RSOAAA>2.0.CO;2
- Anderson G P, Berk A, Acharya P K, Bernstein L S, Adler-Golden S M, Lee J, Muratov L (2009), Reformulated Atmospheric Band Model Method for Modeling Atmospheric Propagation at Arbitrarily Fine Spectral Resolution and Expanded Capabilities. U.S. Patent #7593835
- Berk A, Anderson G P, Acharya P K, Bernstein L S, Muratov L, Lee J, Fox M, Adler-Golden S M, Chetwynd J H, Hoke M L, Lockwood R B, Gardner J A, Cooley T W, Borel C C, Lewis P E, Shettle E P (2006), MODTRAN5: 2006 Update. *Proceeding SPIE, Algorithms and Technologies for Multispectral, Hyperspectral, and Ultraspectral Imagery XII*: 6233, 62331F. doi: 10.1117/12.665077
- Bigelow D S, Slusser J R, Beaubien A F, Gibson J H (1998), The USDA Ultraviolet Radiation Monitoring Program. *Bulletin of the American Meteorological Society*, 79(4): 601-615. doi: 10.1175/1520-0477(1998)079<0601:TUURMP>2.0.CO;2
- Bodhaine B A, Wood N B, Dutton E G, Slusser J R (1999), On Rayleigh optical depth calculations. *J. Atmos. Oceanic Technol.* 16(11): 1854–1861. doi: 10.1175/1520-0426(1999)016<1854:ORODC>2.0.CO;2
- Chehade W, Gür B, Spietz P, Gorshelev V, Serdyuchenko A, Burrows J P, Weber M (2013), Temperature dependent ozone absorption cross section spectra measured with the GOME-2 FM3 spectrometer and first application in satellite retrievals. *Atmospheric Measurement Techniques* 6: 1623-1632. doi:10.5194/amt-6-1623-2013
- Chen M, Davis J, Tang H, Gao Z, Gao W (2012), A multi-channel calibration method for multi-filter rotating shadow-band radiometer. *Proc. SPIE 8513, Remote Sensing and Modeling of Ecosystems for Sustainability IX*, 851305. doi:10.1117/12.929454
- Chen M, Davis J, Tang H, Ownby C, Gao W (2013), The calibration methods for Multi-Filter Rotating Shadowband Radiometer: A review. *Frontiers of Earth Science*, 7(3): 257–270. doi:10.1007/s11707-013-0368-9
- Chen M, Davis J, Gao W (2014), A New Cloud Screening Algorithm for Ground-Based Direct-Beam Solar Radiation. *Journal of Atmospheric and Oceanic Technology*, 31(12): 2951–2605. doi: 10.1175/JTECH-D-14-00095.1
- Dubovik O, Smirnov A, Holben B N, King M D, Kaufman Y J, Eck T F, Slutsker I (2000), Accuracy assessments of aerosol optical properties retrieved from Aerosol Robotic

- Network (AERONET) Sun and sky radiance measurements. *Journal of Geophysical Research* 105(D8): 9791-9806. doi:10.1029/2000JD900040
- Foereid B, Rivero M J, Primo O, Ortiz I (2011), Modelling photodegradation in the global carbon cycle. *Soil Biology & Biochemistry* 43(6): 1383-1386. doi: 10.1016/j.soilbio.2011.03.004
- Forgan B W (1994), General method for calibrating Sun photometers. *Applied Optics*, 33(21): 4841-4850. doi: 10.1364/AO.33.004841
- Gehrke C, Johanson U, Callaghan T V, Chadwick D, Robinson C H (1995), The Impact of Enhanced Ultraviolet-B Radiation on Litter Quality and Decomposition Processes in Vaccinium Leaves from the Subarctic. *Oikos*, 72(2): 213-222. doi: 10.2307/3546223
- Harrison L, Michalsky J (1994), Objective algorithms for the retrieval of optical depths from ground-based measurements. *Applied Optics*, 33(22): 5126-5132. doi: 10.1364/ao.33.005126
- Madronich S (1993), The atmosphere and UVB radiation at ground level. *Environmental UV Photobiology*. In A R Young et al. (Eds.), *Environmental UV photobiology* (pp. 1–39). Plenum Press, New York
- Mayer L M, Thornton K R, Schick L L, Jastrow J D, Harden J W (2012), Photodissolution of soil organic matter. *Geoderma*, 170: 314-321. doi: 10.1016/j.geoderma.2011.11.030
- Parton W, Silver W L, Burke I C, Grassens L, Harmon M E, Currie W S, King J Y, Adair E C, Brandt L A, Hart S C, Fath B (2007), Global-Scale Similarities in Nitrogen Release Patterns During Long-Term Decomposition. *Science*, 315(5810): 361–364. doi: 10.1126/science.1134853
- Reddy K R, Singh S K, Koti S, Kakani V G, Zhao D, Gao W, Reddy V R (2013), Quantifying the Effects of Corn Growth and Physiological Responses to Ultraviolet-B Radiation for Modeling. *Agronomy journal*, 105(5): 1367-1377. doi: 10.2134/agronj2013.0113
- Rozema J, Tosserams M, Nelissen H, van Heerwaarden L, Broekman R A, Flierman N (1997), Stratospheric ozone reduction and ecosystem processes: Enhanced UV-B radiation affects chemical quality and decomposition of leaves of the dune grassland species *calamagrostis epigeios*. *Plant Ecology*, 128(1-2): 285-294. doi: 10.1023/A:1009723210062
- Taylor T E, L'Ecuyer T S, Slusser J R, Stephens G L, Goering C D (2008), An operational retrieval algorithm for determining aerosol optical properties in the ultraviolet. *J. Geophys. Res.*, 113(D3): D03201. doi:10.1029/2007JD008661

APPENDIX 2.A TOD COMPARISON (DIRECT)

The quantity TOD_{D1} is defined as the difference between the target's TOD (TOD_{Tgt}) and one local point's TOD:

$$TOD_{D1} = TOD_{Tgt} - TOD_k \quad (3.15)$$

Where, k lies within the target's local window. Using Eq. (2.4) and Eq. (2.6) on point k , we get

$$TOD_{D1} = -\Delta m_k^{-1} \ln V_{LO} - m_{Tgt}^{-1} \ln V_{Tgt} + m_k^{-1} \ln V_k \quad (3.16)$$

In Eq. (3.16), Δm_k^{-1} is a non-zero value because every point (both the target and the local window points) has a unique airmass and V_{LO} is the unknown calibration parameter. Therefore, it is impossible to calculate directly.

Using a coarsely estimated V_{LO} to do the TOD comparison was found to be impractical. First, it is unknown how the responsivity of the instrument may change based on its previous behavior. It could be stable for years but it could also drop or increase quickly in a short period. Second, the TOD_t calculation using Beer's law [Eq. (2.2)] shows that the bias of the daily V_{LO} approximation is constant, while the airmass varies a lot in a day. As a result, the bias in TOD_t varies a lot in a day. The comparison of such TOD_t with varying magnitudes of bias will make it extremely complicated if not impossible to set a threshold for excluding cloudy points.

APPENDIX 2.B TOD COMPARISON (STANDARD AVERAGE)

The quantity TOD_{D2} is defined as the difference between the target's TOD (TOD_{Tgt}) and the standard average of any two local points' (A and B) TODs:

$$TOD_{D2} = TOD_{Tgt} - (TOD_A + TOD_B) / 2 \quad (3.17)$$

where, the points A and B lie within the target's local window. Using Eq. (2.4) and Eq. (2.6) on points A and B, we get

$$TOD_{D2} = -\frac{\Delta m_A^{-1} + \Delta m_B^{-1}}{2} \ln V_{LO} - m_{Tgt}^{-1} \ln V_{Tgt} + \frac{m_A^{-1} \ln V_A + m_B^{-1} \ln V_B}{2} \quad (3.18)$$

Eq. (3.18) contains the unknown calibration parameter (V_{LO}), which makes it impossible to calculate TOD_{D2} directly. Although it is possible that $\Delta m_A^{-1} + \Delta m_B^{-1}$ is or close to zero for some situations (when Δm_A^{-1} and Δm_B^{-1} have opposite signs and their absolute values are the same or close), normally it is not true (especially not true for the target in the early morning, late afternoon, and near solar noon, when most Δm_A^{-1} and Δm_B^{-1} have the same sign).

APPENDIX 2.C IMPORTANT MODTRAN PARAMETERS

To simulate the 368-nm-channel direct normal and the diffuse horizontal solar irradiance at FL02 on 26 September 2013, the following MODTRAN parameters are used. The parameters are for MODTRAN, version 5.3.

Card 1

MODEL = 1: Tropical Atmosphere

ITYPE = 3: Vertical or slant path to ground

IEMSCT = 4: Execute in spectral solar radiance mode with no thermal scatter

IMULT = 1: Execute with multiple scattering

Card 1A

DIS = T: Use DISSORT discrete ordinate multiple scattering algorithm

DISALB = T: Calculate spectral albedo and diffuse transmittance

NSTR = 8: Number of streams to be used by DISORT

O3STR = ' a0.2784': Column Ozone amount (ATM-cm), data source: EOS Aura OMI daily level 3 global 0.25° gridded data (http://gdata1.sci.gsfc.nasa.gov/daac-bin/G3/gui.cgi?instance_id=omi).

LSUNFL = T: Read a user-specified TOA solar irradiance data.

LBMNAM = T: Read the root name of the band model parameter data.

Card 1A1

DATA/SUN01SAO2010.dat: Data provided by Chance and Kurucz (2010).

Card 1A2

01_2009: The root name of 1.0 band model.

Card 2

IHAZE = 1: RURAL extinction

VIS = -0.103: Negative of the 550 nm vertical aerosol optical depth.

GNDALT = 0.000: Altitude of surface relative to sea level (km)

Card 3

H1ALT = 0.000: Initial altitude (km)

OBSZEN = 180.000: Initial zenith angle (degrees) as measured from H1ALT.

Card 3A1

IPARM = 2: Method of specifying solar geometry on Card 3A2.

IPH = 2: Select Mie-generated database of aerosol phase functions.

IDAY = 269: Day of Year (26 September 2013)

ISOURC = 0: Extraterrestrial source is the sun.

Card 3A2

PARM1: Azimuth angle, which varies at each observation.

PARM2: Solar zenith angle, which varies at each observation.

Card 4

V1 = 26789.: Initial frequency in wavenumber (cm^{-1}).

V2 = 27526.: Final frequency.

DV = 1: Frequency increment.

FWHM = 2: Slit function Full Width at Half Maximum.

FLAGS(7:7) = F: Write a spectral flux (.flx) file.

MLFLX = 1: Number of atmospheric levels for which spectral fluxes are output.

Literature Cited

Chance K, Kurucz R L (2010), An improved high-resolution solar reference spectrum for earth's atmosphere measurements in the ultraviolet, visible, and near infrared. *Journal of Quantitative Spectroscopy & Radiative Transfer*, 111(9): 1289-1295.
doi:10.1016/j.jqsrt.2010.01.036

Part II: Assessing ecological impacts of UV litter decomposition using DayCent

CHAPTER 4: ASSESSING ECOLOGICAL IMPACTS OF UV LITTER DECOMPOSITION USING DAYCENT

Introduction

The carbon (C) and nitrogen (N) balance between atmosphere and terrestrial biosphere is driven by two fundamental processes of production and decomposition (Zepp et al. 1998; Austin and Vivanco 2006; Adair et al. 2008; King et al. 2012). The physical and biological mechanisms behind the production are relatively well understood (King et al. 2012). It is known that mean annual precipitation, seasonal rain pattern, and interaction of precipitation and temperature are the key controlling parameters of net primary production (Austin 2011). However, the mechanisms behind the litter decomposition are not fully clear (Dirks et al. 2010; Austin 2011; King et al. 2012). Decomposition is the primary process by which C and N are cycled between plants, soil, and the atmosphere (Brandt et al. 2009). Decomposition releases N for plant production and microbial activity (Parton et al. 2007; Song et al. 2013). Decomposition of plant litter and soil organic matter releases CO₂ into atmosphere (~53-57 Pg C yr⁻¹, Harmon et al. 2011) at much higher rate than fossil fuel carbon emission (~7.8 Pg C yr⁻¹, IPCC 5th assessment report). The small changes in litter and soil decomposition rate could result in large variation in atmospheric CO₂ concentration (Adair et al. 2008; Bond-Lamberty and Thomson 2010).

Plant litter decomposition influences the formation of soil organic matter, the mineralization of organic nutrients, and the carbon balance in terrestrial ecosystems (Moorhead and Callaghan 1994; Austin and Ballaré 2010, Dirks et al 2010). In mesic ecosystem, the rate of litter decomposition is determined by litter chemistry especially lignin contents (phenolics) and lignin/nutrient ratios (Melillo et al. 1982; Mlambo and Mwenje 2010). Usually, litter with a low

C/N ratio and low lignin content decompose fast and, roots, which have more lignin, decompose slower (Zhao et al. 2014). This pattern is predicted by traditional decomposition models that focus on the roles of microbes on decomposition. These models use climate variables (precipitation and temperature) and litter quality variables (C/N, lignin/N) to predict litter mass loss rates (Gallo et al. 2009).

In semi-arid/xeric ecosystem, however, litter decomposition is faster than prediction of models which are only driven by climate and litter chemistry (Moorhead and Callaghan 1994; Austin and Vivanco 2006; Parton et al. 2007; Vanderbilt et al. 2008; Gallo et al. 2009; Brandt et al. 2010; King et al. 2012). Furthermore, decomposing surface litter does not immobilize nitrogen and the decomposition rate is unrelated to initial N contents in some arid ecosystems (Parton et al. 2007; Brandt et al. 2010). These patterns suggest that abiotic processes rather than microbial activity are the major drivers of decomposition in those ecosystems (Brandt et al. 2010). Field experiments indeed show that abiotic photodegradation has significant impacts on litter decay (e.g. mass loss rate, CO₂ emission, and litter chemistry) in arid desert (Day et al. 2007), in semi-arid grasslands and shrublands (Austin and Vivanco 2006; Rutledge et al. 2010) and in high latitude forest ecosystems (Moody et al. 2001). Day et al. (2007) concluded that UVB is responsible for 14%-22% total litter mass loss in arid and hot sites. Foereid et al. (2011) found that up to 14% NPP is photodegradable in dry and high radiation ecosystems. Gallo et al. (2006) concluded that UV radiation alone, or in combination with microbial activity, is as effective at decomposing litter in arid ecosystems as microbial activity alone in mesic ecosystems.

The mechanistic detail of photodegradation remains uncertain. It is reported that solar (UV) radiation may directly photolyze a molecule through fragmentation, intramolecular

rearrangement, or electron transfer (King et al. 2012; Lee et al. 2012) and indirectly photolyze a non-light-absorbing molecule by promoting the production of reactive intermediates (e.g. singlet oxygen and hydroxyl radical) created from some molecules (often triplet oxygen) receiving energy transferred from radiation absorbing photosensitizers (George et al. 2005; Messenger et al. 2009; Cory et al. 2010; Feng et al. 2011; King et al. 2012). However, uncertainties exist on the specific carbon compounds that are affected by photodegradation, with some evidence for higher loss rates for either cellulosic or lignin pools (Rozema et al. 1997; King et al. 2012). It is also reported that UVB radiation has four important indirect impacts on decomposition: (1) facilitating microbial decomposition by generation of labile material from photodegradation (Austin and Vivanco 2006; Gallo et al. 2006; Henry et al. 2008; Foereid et al. 2010; Andrady et al. 2011; Liu et al. 2014); (2) decelerating decomposition by reducing microbial population and respiration (Gehrke et al. 1995; Zepp et al. 1998; Moody et al. 1999, 2001; Hughes et al. 2003; Day et al. 2007; King et al. 2012; Lin and King 2014) and altering microbial community composition by selecting species that can tolerate extreme climate conditions, repair DNA efficiently or synthesize photo-protective pigments (Moorhead and Callaghan, 1994; Gehrke et al. 1995; Moody et al. 2001; Pancotto et al. 2003, 2005; Gallo et al. 2006); (3) facilitating microbial decomposition or leaching by breaking down cell wall and releasing fats and lipids (Vähätalo et al. 1998; Day et al. 2007; Lin and King 2014); (4) reducing extracellular enzyme activity (Gallo et al. 2006, 2009).

In this study, we examine the role to photodegradation in litter decomposition using the DayCent biogeochemical model with a photodecay submodel. Adair et al. (2015) developed and calibrated a three-C-pool decomposition model that simulates both biotic decomposition and photodegradation of litter. Their model selection results supported flows related to UV radiation

induced direct photolysis, facilitation effects, and microbial inhibition effects. In this study, the Adair et al. (2015) photodecay submodel was added to the DayCent biogeochemical model and used to simulate the semi-arid short-grass steppe ecosystem at three western U.S. sites. First, the model parameters were adjusted to match the observation of soil water content, plant growth pattern, actual evapotranspiration, and net ecosystem exchange at a calibration site. Second, the model was configured to simulate the LIDET decomposition experiment in 1990s for six common litter types at the three sites. A subset of the photodegradation related parameters were optimized for each species individually and across species by the global optimization algorithm that combined scatter search and nonlinear trust region optimization algorithms. Third, the relationship between photodegradation and initial litter chemistry (especially lignin content) was explored. The pattern found between litter's initial lignin content and its potential photodecomposition rate was implemented in the DayCent model. The related parameters were optimized at the calibration site. Fourth, the modified with the optimized parameters was validated at other two sites. Last, the long-term (i.e. 90 years) impacts of photodegradation on ecosystem processes such as plant productivity, C and N pools, N mineralization, and trace gases emission were explored.

Methods

Site and Data

LTER CPER

The DayCent model was calibrated with the measurements made at the United States Department of Agriculture - Agricultural Research Services (USDA-ARS) Central Plains Experimental Range (CPER) site (latitude: 40.816° N, longitude: 104.749° W, elevation:

1646m). The CPER site is located at the western edge of the Central Grate Plains with mean annual precipitation of 434 mm, mean annual air temperature of 9.31°C, and mean annual total solar radiation of 462.63 W/m² between 1990 and 1999. Much of the precipitation occurs from April to June (43%) (Parton et al. 2012). The vegetation at CPER is dominated by *Bouteloua gracilis* (C₄ grass) with a mixture of other C₄ and C₃ grasses, shrubs, forbs, and cacti (Parton et al. 2012). Long-term mean annual aboveground net primary productivity (ANPP) is 97 g (dry mass) m⁻² (Heisler-White et al. 2008), and mean leaf area index is low (<1, Brandt et al. 2007). The pastures were subjected to zero, moderate, and heavy grazing treatments with 0%, 40%, and 65% of annual forage production removed, respectively (Parton et al. 2012). Four types of measurements were made and averaged at daily time resolution at CPER site between 2001 and 2003. The measurements were net ecosystem exchange (NEE), actual evapotranspiration (AET), volumetric soil water content (VSWC), and aboveground live biomass. Both NEE and AET were measured or estimated using the Bowen ratio energy balance (BREB) system (Model 023/CO₂ Bowen ratio System, Campbell Scientific Inc., Logan, UT, USA) (Irmak et al. 2008; Parton et al. 2012). Volumetric soil water content for top 0-15 cm soil was measured using water content reflectometers (Model CS615, Campbell Scientific Inc., Logan, UT, USA) (Parton et al. 2012). Aboveground live biomass during growing season (i.e. late April to end of September) was measured in nine randomly selected one meter squared quadrants around the BREB towers (Parton et al. 2012).

Long-Term Intersite Decomposition Experiment (LIDET⁴) is a 10-year (1990-1999) study of litter decomposition and nutrient dynamics in response to substrate quality and

⁴ Harmon, M. 2013. LTER Intersite Fine Litter Decomposition Experiment (LIDET), 1990 to 2002. Long-Term Ecological Research. Forest Science Data Bank, Corvallis, OR. [Database]. Available: <http://andrewsforest.oregonstate.edu/data/abstract.cfm?dbcode=TD023>. Data were

macroclimate (Gholz et al. 2000; Parton et al. 2007). The experiment was conducted at 28 sites in North and Central America that reflected a wide variety of natural ecosystems and climates (LIDET 1995; Gholz et al. 2000). All 28 sites had nine common litters, fine roots from three species and leaf from six species covering a wide range of initial litter chemistry, and one ‘wildcard’ (LIDET 1995; Adair et al. 2008).

Three LIDET sites used were Central Plains Experimental Range in Colorado (CPER), and Sevilleta (SEV) and Jornada (JRN) in New Mexico. The sites are dry and receive high UV radiation, and surface litter decomposition at these sites were not well explained by macroclimate and litter quality (Parton et al. 2007; Adair et al. 2008). The LIDET CPER site was the same location as USDA-ARS CPER site that was used to calibrate the DayCent decomposition sub-model. The other two sites, SEV and JRN, were used to test the performance of the calibrated DayCent model. The annual aboveground net primary production for SEV and JRN sites were 83 and 130 g (dry mass)/m² (Peters et al. 2013). The climatic characteristic and ecosystem type for the three selected LIDET sites are summarized in Table 4.1.

The six common leaf litter species (ACSA, DRGL, PIRE, QUPR, THPL, and TRAE) were used to calibrate and validate the model performance in this study. The initial values of litter quality indices for these six species are listed in Table 4.2 (extracted from Adair et al. 2008).

provided by the HJ Andrews Experimental Forest research program, funded by the National Science Foundation's Long-Term Ecological Research Program (DEB 08-23380), US Forest Service Pacific Northwest Research Station, and Oregon State University.

DayCent Model

Original DayCent

DayCent (Parton et al. 1998; Del Grosso et al. 2001; Del Grosso et al. 2011) is a daily time step biogeochemical model that simulates exchanges of water, carbon and nutrients (nitrogen [N], potassium [p], and sulfur [S]) among the atmosphere, soil and plants as well as plant phenology and management events (e.g. fire, grazing, cultivation, and organic matter addition). The DayCent model inputs (Del Grosso et al. 2011) include daily weather data (e.g. minimum/maximum temperature, precipitation, and solar radiation), soil properties by layer (e.g. each layer's bulk density, field capacity, wilting point, texture, root fraction, and saturated hydraulic conductivity), site location and weather statistics, crop cultivar parameters (e.g. temperature and water stress functions, respiration, growth, and death rates, and production allocation among plant parts), and management information. The four primary submodels are plant production, soil carbon and nutrient dynamics, soil water and temperature dynamics, and trace gas fluxes (Del Grosso et al. 2001; Del Grosso et al. 2011). The DayCent model has been used extensively to simulate ecosystem dynamics for agricultural ecosystems (Del Grosso et al. 2005; Stehfest et al. 2007), grasslands and savannas (Parton et al. 2011; Parton et al. 2012) and forest systems (Savage et al. 2013) and has been tested using extensively observed data sets (e.g. nitrous oxide emission, crop yield, soil C and N [Del Grosso et al. 2008]).

Plant production (net primary productivity [NPP]) is a function of genetic potential, solar radiation, phenology, water and temperature stress, and nutrients availability (Del Grosso et al. 2008). The allocation of NPP among plant components (e.g. shoots and mature and juvenile roots for crop/grass) is controlled by vegetation type, phenology, and water/nutrient stress (Del Grosso et al. 2008). The death rate of plant parts is controlled by soil water, temperature, season,

and plant specific senescence parameters (Del Grosso et al. 2011). Soil carbon and nutrient dynamics are modeled using a daily version of the Century model (Parton et al. 1987, Parton et al. 1988) which simulates carbon and nutrient flows for the surface and soil organic matter pools (structural and metabolic litter, microbes, and slow and passive soil organic matter). The model simulates the transfer of C and nutrients from dead plant material to litter and soil organic matter (SOM) and the major controls on the flows include litter lignin content and the C/N ratio, temperature/water decomposition factors, and soil texture (Del Grosso et al. 2001). The nutrient pool is supplied by decomposition of SOM, N fixation, and external nutrient addition such as fertilization and N deposition (Del Grosso et al. 2001). APPENDIX 4.A summarized the C and N fluxes between litter and soil organic matter pools in DayCent.

The land surface sub-model of DayCent simulates water flow through the plant canopy, litter, and soil profile, as well as soil temperature (Parton et al. 1998; Del Grosso et al. 2011). Precipitation is first intercepted by vegetation and litter as a function of their biomass and evaporated at the potential evapotranspiration rate (PET) (Del Grosso et al. 2001). PET is estimated as a function of daily minimum and maximum temperature and top of the atmosphere solar radiation at the site. Water inputs (rain, melt snow, and irrigation) that are not intercepted infiltrate the soil or run off of the soil surface (Del Grosso et al. 2001). The model simulates the unsaturated bidirectional flow using Darcy's law (Parton et al. 1998) and saturated flows using a tipping bucket approach. The temperature sub-model calculates temperature at each soil layer as a function of daily minimum and maximum temperature, plant biomass, snow cover, soil moisture, soil texture, and day length (Del Grosso et al. 2001).

The N-gas sub-model of DayCent simulates soil N₂O, NO_x, and N₂ gas emissions from nitrification and denitrification (Del Grosso et al. 2000; Parton et al. 2001; Del Grosso et al.

2011). Nitrifying microbes oxidize NH_4^+ to NO_3^- and release N_2O and NO_x during the intermediate steps (Del Grosso et al. 2011). The rate of nitrification is controlled by soil NH_4^+ concentration, water content, temperature and pH (Parton et al. 2001). Denitrification is a biochemical process in which heterotrophic microbes reduce NO_3^- to NO_x , N_2O , and N_2 under anaerobic conditions (Del Grosso et al. 2001). Denitrification is controlled by labile C availability (e^- donor), soil NO_3^- concentration (e^- acceptor), and O_2 availability (competing e^- acceptor) (Del Grosso et al. 2000). The daily time step allows DayCent to simulate the trace gases fluxes through soils in response to short term water content variation (Del Grosso et al. 2001).

DayCent-Photosyn

The SIPNET (Simple Photosynthesis and Evapo-Transpiration) model (Braswell et al. 2005) is a simplified Farquhar plant photosynthesis and respiration model (Savage et al. 2013) and is incorporated to create the new DayCent version (DayCent-Photosyn or PhotoCent, Straube 2011). The major differences between PhotoCent and DayCent include the capability of simulating the global primary production (GPP) and the introduction of the carbon storage pool that is fueled by photosynthesis and supports the maintenance respiration, actual NPP and growth respiration. The calculation of actual NPP and growth respiration in PhotoCent follows the strategy used by DayCent, but the demanded C of the two processes is withdrawn from the carbon storage pool.

DayCent-UV

Traditional decomposition models fail to accurately predict the atypical linear pattern of aboveground litter mass loss in arid environment, suggesting that photodegradation should be considered in a decomposition model (Parton et al. 2007). Adair et al. (2015) thus extended a three-pool biotic decomposition model of surface litter (Adair et al. 2008) with three modifications related to solar radiation: (1) adding photodegradation fluxes from cellulosic (intermediate) and/or lignin (slow) pools to increase abiotic mass loss of litter; (2) allowing a fraction of those photodegradation fluxes to enter the labile pool to facilitate litter decomposition; and (3) slowing the labile pool's decomposition to simulate the inhibitive effect of solar radiation on microbial activity. The modifications were confronted with LIDET observations using a model selection technique based on the small sample size corrected Akaike's Information Criterion (AICc, Burnham and Anderson 2002). The results suggested that all three modifications improved prediction of all standard aboveground LIDET litter types when compared to the biotic decomposition model (Adair et al. 2015).

We used this conceptual framework and results from Adair et al. (2015) to develop a new surface litter decay model (DayCent-UV, Figure 4.1). DayCent-UV has the following flows and CO₂ loss paths added or modified: (1) the direct C loss as CO₂ due to photodecomposition of standing dead material; (2) the direct C loss as CO₂ during the breakdown of large compounds in surface structural; (3) the transfer of photodegraded C and N from surface structural to surface metabolic; (4) the decomposition rate of the surface metabolic is reduced by higher solar radiation via the metabolic decomposition reducer (*mdr*); and (5) the decomposition rates between the surface active and the surface slow are increased by higher solar radiation via the microbial turnover rate increaser (*mti*). The added flows (1) and (2) increase abiotic mass loss of

litter due to photodegradation. The added flow (3) facilitates litter decomposition by providing more labile materials. The modified flows (4) and (5) simulate the effects of solar radiation on microbial activity. The equations (APPENDIX 4.B) which describe the flows of carbon and nitrogen in new DayCent-UV (or PhotoCent-UV) litter decay model and the estimation of daily solar radiation from daily minimum and maximum temperatures (APPENDIX 4.C) are presented in the online material.

Simulation of LIDET experiment in DayCent

Surface litter decay in LIDET experiment was simulated in DayCent with surface organic matter pool. The surface pool was cleared at the beginning of the simulation, and 100 g of organic matter was added as surface organic matter with the C/N ratio and lignin fraction matching the leaf litter for the LIDET experiment (Bonan et al. 2013). All flows between the surface pool and soil pool were stopped. The quantities of C and N in the surface pool were tracked during the simulation as remaining C and N fractions of the initial organic matter. DayCent has four distinct pools within the surface organic matter pool: structural and metabolic pools that represent plant litter, and microbe and slow pools that represent decomposed organic matter (Figure 4.1). The organic matter representing litter bags was added to the structural and metabolic pools.

Since surface pools were used to represent litter bags, no new litter from standing dead and dead fine roots were allowed to enter any surface pools during the 10-year period. Similarly, the surface pools were not allowed to mix with soil organic matter pools. A full list of CPER parameters is presented in APPENDIX 4.E.

The fire at the beginning of the simulation cleared all live shoots, standing dead, and surface litter. To prevent standing dead from accumulating in the simulation, it was cleared at the end of each year.

Model Parameterization

Use of generalized parameters will likely lead to poor model performance and tuning input variables of the model is needed to better represent site-specific conditions (Del Grosso et al. 2011). Following the suggested order of model calibration (Del Grosso et al. 2011) and the available observed data, the input parameters related to the soil water content, plant growth pattern, UVB litter decay, evapotranspiration, and photosynthesis were adjusted. Plant production, photosynthesis, and soil water submodels were calibrated with observed daily net ecosystem carbon exchange (NEE), soil water (0-20 cm depth) and actual evapotranspiration rates, and seasonal changes in live biomass from 2001-2003 (Parton et al. 2012). UVB litter decay model was calibrated with LIDET litter decay observations from the Colorado site. LIDET observations from two sites in New Mexico (Sevilleta and Jornada) were used as an independent validation of the ability of the UVB litter decay model to simulate mass loss and nitrogen release from surface litter.

The observed SGS Colorado site soil texture and soil water data (Parton et al. 2012) were used to estimate the field capacity, wilting point and minimum water content for the different soil layers. The soil physical properties for each soil layer such as bulk density, saturated hydraulic conductivity, snow melt parameter, and live root fractions were also adjusted. The snow equivalent precipitation amount was adjusted (increased by 75%) in the winter to early spring period based on observed daily rain gauge and lysimeter data showing that the rain gauge

substantially underestimated water inputs for snow events. The scaling factor for potential evapotranspiration and the damping factor (a multiplier controls unsaturated water flux between adjacent soil layers) were reduced and the duration of each rain event were increased in order to better represent the observed daily soil water data and actual evapotranspiration data (2001-2003). Daily maximum and minimum air temperature and precipitation data (1969 to 2010) at the Colorado site were obtained from multiple sources (e.g. <http://hdl.handle.net/10217/82446>⁵; <http://www.ncdc.noaa.gov/cdo-web/>; <http://www.ars.usda.gov/Main/docs.htm?docid=11120>⁶; <http://www.wcc.nrcs.usda.gov/nwcc/site?sitenum=2017>⁷; Parton et al. 2012) with the highest quality possible. We used the SGS Colorado soil physical properties (field capacity, wilting point, bulk density etc.) and the observed site specific solar radiation and maximum and minimum air temperature and precipitation data from multiple sources [NCEP Reanalysis data (NARR)⁸; <http://www.ncdc.noaa.gov/cdo-web/>; <http://dx.doi.org/10.6073/pasta/abf2b27152d632ab2ab27c6c71a8a10a>⁹; <http://dx.doi.org/10.6073/pasta/669823a9c848c979d2888912a56678c3>¹⁰] for the Sevilleta and Jornada sites' computer runs.

⁵ Parton, W. J. SGS-LTER Standard Met Data: 1969-2010 Manually Collected Aboveground and Belowground Meteorological Data collected on the Central Plains Experimental Range, Nunn, Colorado, USA, ARS Study Number 4.

⁶ The data is provided by Rangeland Resources Research Unit, Agricultural Research Service, 8408 Hildreth Road, Cheyenne, WY 82009, Jack Morgan – Research Leader

⁷ National Water and Climate Center, Natural Resources Conservation Service, United States Department of Agriculture. Available online at <http://www.wcc.nrcs.usda.gov/>. Accessed [April/2015]

⁸ NCEP Reanalysis data provided by the NOAA/OAR/ESRL PSD, Boulder, Colorado, USA, from their Web site at <http://www.esrl.noaa.gov/psd/>

⁹ Jornada Basin LTER (2012-03-28): LTER Weather Station daily summary climate data. Jornada Basin LTER; Long Term Ecological Research Network.

¹⁰ Moore, Douglas I. Meteorology Data at the Sevilleta National Wildlife Refuge, New Mexico, (1987-). Long Term Ecological Research Network.

The main data sets we used to parameterize the plant growth submodel include the observed seasonal change in live leaf biomass (2001-2003), daily observed daytime and nighttime NEE data (2001-2003), and observed historical plant production data from the SGS site¹¹. The live biomass data and NEE data were used to parameterize the plant phenological controls on plant growth and maximum photosynthesis rate (e.g. reduced growth and photosynthesis rates at the end of the growing season). The live biomass data was used to parameterize the impact of soil water stress on plant growth (increased reduction in plant growth with relative water content less than 0.6). The 30-year observed plant production data suggested that the optimal growth temperature needed to be reduced and that the nitrogen inputs to the system needed to be increased. The net effect of the model parameter changes was to increase the impact of drought stress on plant growth, reduce the impact of nitrogen stress on plant growth, and replicate the observed seasonal live biomass pattern showing highest live biomass in June and a sharp decrease in live biomass in July. We also made a change to the equations which simulate enhanced soil organic matter decay rates following rainfall events during the growing season based on the observed NEE data sets.

The model uses daily temperature data to estimate the daily total solar radiation and applies a site specific monthly cloud and aerosol adjustment coefficient to get the total solar radiation estimate. The model used observed solar radiation data sets (NCEP Reanalysis data) to calibrate the twelve solar radiation monthly adjustment coefficients. The same calibration process was used for the CPER, Jornada and Sevilleta sites.

¹¹ Lauenroth, William K. SGS-LTER Standard Production Data: 1983-2008 Annual Aboveground Net Primary Production on the Central Plains Experimental Range, Nunn, Colorado, USA 1983-2008, ARS Study Number 6. Retrieved from <http://hdl.handle.net/10217/81141>

The LIDET mass and nitrogen remaining data from the six different surface litter decay results from the CPER site were used to parameterize UVB litter decay parameters. We used a model optimization program to calculate the optimal values of the parameters. It is a global optimization method that combines the scatter search framework (Laguna and Martí 2003) and gradient based non-linear trust region optimizer (Conn et al. 2000; Ugray et al. 2007). We defined a nondimensionalized objective function for the optimization method to evaluate the performance of DayCent parameters on fitting multiple types of observational variables (i.e. surface remaining C and N fractions). The same numerical optimization procedure was used to determine the parameters for the plant production submodel. The detailed design of the optimization method is found in the next subsection. The optimal value for the model parameters were not always used in the final model because the optimal value of the parameter may not make biological sense. The optimization process was quite useful for identifying the critical parameters which impact the fit to the observed data sets, however, we manually adjusted some of the optimal parameters values based general biological knowledge. The values for the model input parameters changed during model optimization process are found in online material (APPENDIX 4.D and APPENDIX 4.E) and the Century website. The Century website contains all of the information needed to run the DayCent model for Colorado, Jornada and Sevilleta sites.

Optimization Method

Scatter search is a flexible and effective framework to solve optimization problems. It was introduced by Glover (1977) as a heuristic for integer programming (Laguna and Martí, 2003). It can be characterized as an evolutionary method, however, unlike the Genetic Algorithm, scatter search emphasizes systematic development of reference set following certain

principles as opposed to the more extensive use of randomization (Ugray et al. 2007). It can deal with many types of problems, including continuous, binary variables and permutation vectors (Laguna and Martí, 2003). It has been successfully applied to hard optimization problems (Martí et al. 2006).

The template of the scatter search algorithm introduced by Glover (1998) is the main guidance for most of the scatter search implementation up to date (Laguna and Martí 2003). The template consists of the “five methods”: diversification generation method, improvement method, reference set update method, subset generation method, and solution combination method (Glover 2000; Laguna and Martí 2003; Martí et al. 2006; Naderi and Ruiz 2014).

For continuous problems, a simplified global optimization algorithm following the framework proposed by Ugray et al. (2007) was developed in this study. The algorithm takes advantage of scatter search method’s ability to locate approximated solutions while avoids the disadvantages of its weak ability to handle constraints and to achieve high accuracy by calling gradient-based trust-region algorithm provided by Intel Math Kernel Library (Conn et al. 2000; Ugray et al. 2007). A brief description of the trust-region algorithm is found in APPENDIX 4.F.

The optimization uses a nondimensionalized objective function (OF) to describe the relative difference between the model and the observation on multiple observational variables:

$$OF(P) = \sum_{j=1}^{N_v} \sum_{i=1}^{n_j} \left(\frac{x_j(i, P) - y_j(i)}{Y_j} \right)^2 \quad (4.1)$$

Where, P is the DayCent model parameters to be evaluated/optimized; N_v is the number of the variable types; $Y_j = \sqrt{\sum_{i=1}^{n_j} (y_j(i))^2}$; j is the subscript for observational type and i is the subscript of observations for an observational type; n_j is the number of observations of the type

j ; $x_j(i, P)$ and $y_j(i)$ are the i th modeled and observed values for observational variable type j , respectively.

The flowchart of the global optimization for DayCent parameters is presented in Figure 4.2.

Initialization

In the initialization, the size of Reference Set (RefSet or RS) is set to b ; RS is created as an empty set; the size of Pool is set to BS; the size of initial population is set to $10*b$; the stage 2 iterator k is set to 0; the Maximum stage 2 Iteration (MI) is set to 800. In this study, $b=10$, BS=20.

The stage 1

After initialization, the algorithm calls the “Generate Population” method, which uses the stratified-sampling procedure described in Laguna and Martí (2003) and online supplement to Ugray et al. (2007), to generate $10*b$ points (initial population) within the bounds. The two points at the lower and upper bounds, the middle point between them, and an additional user specified point may be added to the initial population.

The algorithm then evaluates the objective function values (OF)s at initial population points and sorts them by their OFs. The best $b/2$ points are added to RS. The Euclidean distances between the rest initial population points and RS are calculated. The $b/2$ points with the largest distances to RS are added to RS (Ugray et al. 2007). This evaluation process is time consuming for two reasons: (1) each DayCent call takes 2-5 minutes depending on CPU ability and the basic structure of DayCent is hard to be parallelized; and (2) for multiple sites problems, the time

required to calculate a single OF sequentially is simply the multiplication of the number of sites and 2-5 minutes. Therefore, multi-threading technique is utilized to reduce the total time spent in this process.

The gradient based non-linear optimizer, described in APPENDIX 4.F, is used as the “Improvement” method. The improved/optimized point is called the solution. The “Improvement” method is applied to the best point in RS. The best point in RS is replaced by its solution, and the corresponding OF is also updated (Ugray et al. 2007). The threshold (thr), below which the quality of a point is considered good enough to launch the “Improvement” method in the stage 2 iterations, is set to the solution’s OF (Ugray et al. 2007).

The stage 2 (main loop)

The stage 2 is an iterative process that aims at improving the quality of RS. In each iteration, the algorithm first finds new subsets of RS with the “Subset Generation” Method (Ugray et al. 2007). In this study, only new subsets consisting of the two-point pair that has not been examined since the beginning of the stage 2 are considered (Ugray et al. 2007). This requires the memory of all previously examined subsets.

For a given subset s , define x_1 and x_2 the two points in the pair, the three trial points (x_3 , x_4 , and x_5) for s are combined from x_1 and x_2 (“Combination Method”, online supplement to Ugray et al. 2007):

$$\begin{aligned}
 d &= (x_2 - x_1) / 2 \\
 x_3 &= x_1 - d \\
 x_4 &= x_1 + d \\
 x_5 &= x_2 + d
 \end{aligned}
 \tag{4.2}$$

If any trial points are outside of bounds, the dimensions violate the upper bounds are projected to the upper bounds and the dimensions violate the lower bounds are projected to the lower bounds (Ugray et al. 2007). Applying the “Combination Method” to all subsets, we get the collection of trial points for the current iteration. The Pool is used to temporarily store the trial points and their OFs at the current iteration and is initialized as an empty set at the beginning of each stage 2 iteration.

The trial points are grouped into batches. Each batch contain BS trial points except for the last batch, which may have 1 to BS trial points. The OFs for trial points in each batch are evaluated in parallel. The trial points and their OFs are inserted into the Pool. The stage 2 counter k is incremented by the current batch size.

At least one trial point in the current batch should pass the two merit functions (filters or tests) to trigger the “Improvement” method. The first one is called the distance filter, which insures the to-be-improved trial point is not too close to any previously found local solutions (Ugray et al. 2007). This filter assumes there is a spherical attraction basin around every previous local solution point. The radii of an attraction basin is defined by the Euclidean distance between the solution and the corresponding starting point. The trial point passes the distance filter if its Euclidean distance to any solution is larger than $0.75 * \text{radii}$. This filter requires the memory of previous “Improvement” information, including the starting points and the corresponding solutions. The second one is called the merit filter, which insures that the to-be-improved trial point is of high quality (Ugray et al. 2007). The trial point passes the merit filter if its objective function value is lower than the current threshold (initialized in the stage 1).

If the best trial point in the current batch passes the two tests, the “Improvement” method is applied to the point. The point in Pool is replaced by its solution and moved to RS (Ugray et

al. 2007). The threshold value is updated with the solution's OF. Repeat the process until no trial point in the current batch passes the two tests.

Then, the threshold value (thr) is updated with the following formula (Ugray et al. 2007):

$$thr = thr + 0.2 * (1 + abs(thr)) \quad (4.3)$$

After all trial points in the current stage 2 iteration have been processed, a combined set ($RS \cup Pool$) is created. It is possible that most good points in the combined set are resided in a small region due to the noisy shape of objective function. To avoid this, it is optional to remove the points in the combined set with close OFs (e.g. within 1% range) and close distances (e.g. within 3% range) (Ugray et al. 2007). RS is updated with the best b points in the combined set ($RS \cup Pool$).

If no new element(s) found for RS in the current stage 2 iteration and $k \leq MI$, the algorithm replace the worst $b/2$ points in RS with $b/2$ most diverse points from the "Generate Population" method described in the stage 1 (Ugray et al. 2007). Their OFs are evaluated in parallel and stored in RS.

The stage 2 iteration finishes when $k > MI$ and the final RS ordered by OF are reported as the candidates for the global optimum.

Results

Model performance on ecosystem variables

Before validating the UV decomposition module in DayCent model, the model was calibrated with four observed ecological variables (net ecosystem carbon exchange, volumetric soil water, actual evapotranspiration and aboveground live biomass) at CPER site in 2001-2003. The adjustment of model parameters has been described in a previous subsection. Generally, the

modeled and observed volumetric soil water content [Figure 4.3(a)] in the first 0-20cm (vswc) layer agreed well ($R^2 = 0.4849$) in the 3-year period (i.e. 2001-2003). For model and observation, the maximum and minimum vswc were both around 0.17 and 0.03 in the summer period. Both model and observation showed the pattern of each vswc spike matching a corresponding rain event. Most modeled vswc spikes dropped faster than observation. The modeled vswc in winter periods was higher than observation when there were snow events. The average span of observed vswc spikes after snow events was greater than one month, while that of modeled vswc spikes was less than half a month. The observations of vswc during the winter when soil temperatures are below freezing are not very accurate and thus should not be used to test the model performance from December to March when soil temperatures are frequent below 0 °C.

The observed aboveground live biomass is calculated as the average under three grazing intensities (Parton et al. 2012). Generally, the modeled and observed aboveground live biomass agreed well ($R^2 = 0.4984$) in the 3-year period. The modeled peak live biomass was low (≤ 20 g/m²) in the dry year (i.e. 2002) and was much higher (> 120 g/m²) in the subsequent wet year (i.e. 2003) as shown in observation. Both model and observation showed a two-stage intra-annual growth pattern: the fast spring – early summer growth stage and the significantly slower late summer – autumn growth stage. Model and observation showed different patterns of the transition between the two stages. The model used a single event on day 200 to simulate the transition and the transition was sudden. The observation showed a gradual decrease of live biomass in the transitional period (i.e. one month period in late Jun to July). Because of the grazing events, the model showed the additional low-frequency and low-magnitude fluctuation of live biomass during the entire growing season.

The general patterns of modeled and observed actual evapotranspiration (AET) agreed well ($R^2 = 0.4409$) in the 3-year period. The AETs were both low (i.e. around zero) in winter periods. In summer periods, the peak AETs were both in the range of 0.3 to 0.6 cm H₂O in wet years (i.e. 2001 and 2003) and in the range of 0.0 to 0.3 cm H₂O in the dry year (i.e. 2002). Unlike in the wet years, both modeled and observed AET was not gradually increasing in the spring period in the dry year. Both of them showed elevated AET in response to big rain events, but the modeled AET dropped faster and stabilized at lower values than the observed after big rain events.

The modeled and observed net ecosystem exchange (NEE) had a less agreement ($R^2 = 0.2301$) in the 3-year period compared to the other three ecological variables. In the plot (Figure 4.3), a positive NEE value represents the net C intake from the atmosphere, meaning photosynthesis is stronger than the sum of all respirations and photodegradation; the negative NEE value represents the net C release from the ecosystem and has the opposite meaning. Generally, the observed NEE had a larger daily variation than the modeled NEE. The observed NEE also had more days with more negative values especially during the growing season. The modeled NEE was mostly zero with some negative peaks in the dry year (i.e. 2002). In contrast, the observed NEE was mostly slightly positive in that year. There were still some modeled NEE patterns matching the observation well. For example, both the model and observation showed that NEE is positive during the early growing season with the magnitude in the range of 2 to 5 g/m². Both the model and observation showed close-to-zero NEE values in winter periods and negative spikes occurred after big rain events.

UVB Model verification and validation

The performance of the DayCent-UV model was examined by comparing model results to the observed carbon and nitrogen fraction remaining vs time for the six common litter species in the 10-year LIDET experiment (i.e. 1990-1999) at the Colorado calibration site (Figure 4.4). A scatter diagram of the simulated DayCent-UV model vs data as a function of plant species is shown in Figure 4.5. The observed time series of remaining carbon fraction shows that some of the species follow a more exponential pattern of carbon loss (ACSA and DRGL), while the other species display a more linear pattern for carbon release vs time. There are considerable species differences in the carbon loss rates with DRGL and TRAE losing the most carbon and a general pattern of less carbon loss with increasing lignin content of the litter (THPL had the highest lignin content and the lowest carbon loss). The comparison of the observed vs simulated carbon remaining vs time suggests the DayCent-UV model consistently overestimate the decomposition rate in the early stage (i.e. first 3 years). The scatter diagram of observed and DayCent-UV model simulated carbon remaining for all of the species (Figure 4.5) shows that the model tends to underestimate carbon remaining for observed carbon remaining greater than 0.5 and overestimate carbon remaining for observed carbon remaining less than 0.3. The model performance of the modified DayCent-UV varied by litter species. The model results show that the DayCent-UV model has the best performance on species THPL [0.1289 (RMSE for C), 0.1656 (RMSE for N)] followed by ACSA (0.0953, 0.2741), QUPR (0.1191, 0.1863), TRAE (0.1649, 0.3157), PIRE (0.1643, 0.2571), and DRGL (0.1365, 0.3176). There is no obvious correlation between the model performance and litter's initial C/N ratios and lignin content.

Comparison of the observed carbon and nitrogen remaining vs time data (Figure 4.4) shows that the observed nitrogen data has larger differences in the litter species and large

unexplained changes in the observed N remaining vs time (e.g. N remaining for PIRE goes from 0.65 in 1994 to 1.1 in 1995 and then decreases to 0.5 1996). Clearly, the observed nitrogen data is much more variable, uncertain and difficult to predict using the model. Observed N remaining data show a general pattern of decreased N remaining with increasing time for most species, however, N remaining data for TRAE is greater than one (up to 1.4) 5 years after the beginning of the experiment. The DayCent-UV model simulates the observed pattern of N losses increasing with time and the overall RMSE values for the model vs data comparison is higher for nitrogen remaining compared to carbon remaining (RMSE = 0.1567 for nitrogen vs 0.1159 for carbon). The DayCent-UV model tends to underestimate the fraction of N remaining for DRGL and ACSA and overestimate the fraction of N remaining for PIRE and TRAE (see Figure 4.4 and Figure 4.5). Clearly, the DayCent-UV model is unable to predict some of the observed species differences in the N remaining, however, there was no overall bias in modeled remaining N fraction.

The DayCent-UV model (optimized using the Colorado site data) simulated model results were compared with the observed carbon and nitrogen remaining data from the Sevilleta and Jornada sites as an independent validation test. Site-specific parameters, such as site's location, soil profile, solar radiation and weather data, were adjusted to reflect the environment at the testing sites. Comparison of the DayCent-UV model vs observed carbon and nitrogen remaining for the different plant species at the Sevilleta and Jornada sites (Figure 4.6) show that the model did a good job simulating the litter carbon remaining for the different species [RMSE(across-species two-site average C) = 0.1206]. These results are similar to the modeled carbon remaining vs the observed data at the Colorado site [RMSE(CPER) = 0.1159] and still show the simulated bias at the Colorado site that overestimates carbon loss for observed carbon remaining values >

0.5 and underestimates carbon loss for observed carbon remaining < 0.3. The results for nitrogen remaining had much higher RMSE compared to the carbon remaining data (across-species two-site average RMSE = 0.2110 for N vs 0.1206 for C) consistent with the observed pattern for the Colorado site (parameterization/calibration site). The RMSE of the DayCent-UV model for carbon and nitrogen at the parameterization and verification sites are similar [RMSE for C: 0.1195 (Sevilleta) and 0.1191 (Jornada); RMSE for N: 0.0419 (Sevilleta) and 0.2073 (Jornada)]. The results also show that the model consistently overestimates nitrogen release for DRGL and underestimated N release for PIRE and TRAE species. This pattern is generally consistent with the observed data for the Colorado site. Both the calibration and validation data sets show that when all of the litter species are considered, the model is not biased, however the model does not simulate some of the observed species specific difference in N release.

One of the important improvement to the Adair et al. (2015) UVB model was to add the impact of the plant lignin content on the maximum photo decay parameter (maxphoto). Analysis of the results showed that the impact of radiation on photodecay decreased with increasing lignin content of the litter. The equation we used to represent the impact of lignin is shown in the online material (APPENDIX 4.B) and including the impact of lignin content on photo decay increased the fit of the DayCent-UV model to the observed carbon release date (RMSE for remaining carbon decreased from 0.1509 without the lignin impact to 0.1159 using the lignin content equation). We also optimized the value of maxphoto to get the best fit for individual plant species and evaluated the performance change from using the original DayCent-UV model with individually optimized maxphoto coefficients to using the modified DayCent-UV model with two maxphoto coefficients (see Table 4.3). The results show that the litter specific optimized maxphoto values can be significantly different for some species (ACSA and QUPR) and that the

modified DayCent-UV model's RMSEs for carbon and nitrogen at all species are not significantly increased even though the number of maxphoto coefficients is greatly reduced (i.e. from 6 to 2).

Effects of UV module on spatial and temporal C and N patterns at 3 LIDET sites

The model results compare the performance of the DayCent-UV model with the original DayCent-Photosyn model (photo_off), evaluate how well the DayCent-UV model simulate the observed differences in carbon and nitrogen remaining for the Sevilleta and Jornada, and Colorado sites, and look at the ecosystem impact of including UV radiation at the Colorado site. The performance of two DayCent versions, the modified DayCent-UV and the DayCent-Photosyn (photo_off), was compared with the observed across species average remaining C and N data from the LIDET experiment at the Colorado site (Figure 4.7). The observation showed a linear decrease in carbon for the first 6 years of the experiment and greatly reduced decomposition rates in the last 4 years. The observation showed balanced N mineralization and immobilization in the first 2 years and net N release in the rest period. Both DayCent versions release C with exponential patterns. Compared with the photo_off DayCent, the modified DayCent-UV model showed slightly slower C decomposition rate in the early stage but showed over 10% more C loss in the later stage. The modified DayCent-UV model showed a persistent net N release in the entire 10-year period with the final N remaining fraction at around 0.55, while the photo_off DayCent showed slight net N immobilization in most time periods except for in 1991 and 1992, in which period net N release was simulated. The modified DayCent-UV model matched the LIDET observation better than the photo_off DayCent for both C and N in most time periods and had much higher N loss compared to the photo_off DayCent.

Figure 4.8 shows the comparison of the DayCent-UV simulated species averaged C and N remaining vs time with the corresponding LIDET observation for the Colorado, Sevilleta and Jornada sites. Observed C remaining points at three sites are more clustered than N and nitrogen remaining is higher than the carbon remaining. The DayCent-UV model also shows this pattern. The observation shows more linear pattern of C remaining vs time in the first 6 years while the DayCent-UV model shows more exponential C pattern in the entire period. Both observation and model show linear pattern of N remaining vs time. The model predicts faster C decomposition rates in the first 3 years than the observation, but fits the observation points for both C and N in the later years. The DayCent-UV model shows small but distinguishable difference at three sites on both C and N remaining over time with the highest C and N loss in the JRN site. The annual solar radiation at Colorado site (462.63 W/m^2) is lower than both at Sevilleta site (520.59 W/m^2) and at Jornada site (526.10 W/m^2). As expected, Colorado site generally shows the lowest C decomposition rate followed by Sevilleta and Jornada sites, although the observed data points are noisy and somewhat intertwined. This pattern for N release is clearer. The DayCent-UV model manifests the same pattern for both C and N after 3-4 years. But at the early stage (i.e. the first 3-4 years), the model shows more variable C and N decomposition rates between sites. The model clearly overestimates C loss during the first three years for all sites.

Ecological impacts of photodegradation

Photodecay directly changes the C and N dynamics in surface pools. These changes may indirectly influence other ecosystem processes. To present the ecological impacts of photodegradation, the 90-year (1900-1989) average of the modeled ecological variables were calculated for model runs with (i.e. “photo_on”) and without (“photo_off”) the photodecay

module (Table 4.4). The results show that including photo decay causes increases in above and belowground plant production, surface litter net N mineralization, and litter N, while soil C and N, soil net N mineralization and surface litter C all decrease. The model results also show minimal changes (less than 1%) in biotic decomposition rates, and trace gas flux results (data not shown in the table). The biggest impact of including photodecay are to increase surface litter N mineralization rates by 25%, and surface litter N pools (8%), while soil C and N levels and mineral soil net N mineralization rates are decreased. The decreases in mineral soil C and N are a result of the amount of surface litter moving into the mineral soil layer (greater losses of surface litter and standing dead to the atmosphere due to photooxidation). The simulated large increases in surface litter N mineralization are consistent with the results in Figure 4.7 showing that including photooxidation greatly enhanced the N release for surface litter consistent with the observed LIDET litter N release data.

Discussion

Generally, the DayCent-UV model fits the major patterns in observed first 20cm soil water content, aboveground live biomass, and actual evapotranspiration well with their R^2 between 0.44 and 0.50 (Figure 4.3). However, the model performance is not as good on fitting the observed net ecosystem exchange (NEE, $R^2 = 0.23$). If we align modeled and observed NEE with precipitation data in the growing season, it is seen that the model underestimates some CO_2 pulses (negative NEE) right after big rain events. The mechanisms (Ma et al. 2012; Moyano et al. 2013) behind these respiration pulses (or “Birch Effect”) include: (1) re-hydrating dormant microbes; (2) causing the death of microbial biomass and releases intra-cellular osmolytes accumulated during the dry period; (3) breaking down soil micro-aggregates and exposes the

protected organic matters; (4) causing the microbial cell lysis, releasing cytoplasmic solutes, and uncoupling enzymatic activity from cellular respiration; and (5) releasing the quickly decomposable molecules via photodegradation and/or extra-cellular enzymes decomposition accumulated during dry periods. The DayCent-UV model assumes that soil carbon decay rates are increased (3 time normal values) following rainfall events in order to represent the pulse rainfall effect on heterotrophic respiration. The underestimated CO₂ pulses following rainfall events suggest that the model needs to include a fast labile pools that decomposes rapidly following the rainfall events since the size of the CO₂ pulses is similar for each rainfall event during the growing season independent of the time since rainfall (Parton et al. 2012).

Generally, the DayCent-UV model fits the observed remaining C vs time pattern well for both individual species and across species averages [Figure 4.4, Figure 4.7(a), and Figure 4.8(a)]. The DayCent-UV model overestimates the C release in the first three years but shows good matches in the last four years of simulating the LIDET experiment. In the middle stage (i.e. 4-6 years), the DayCent-UV model has lower carbon decomposition rates, and shows a more exponential pattern of the remaining carbon fraction compared with the observed linear pattern. The current DayCent-UV model only considers instant photodegradation and the amount of C released is proportional to the solar radiation intensity and size of the litter structural pool. As a result, materials are photodegraded faster in the earlier stage and slower in the middle and later stages. The discrepancy between model and observation suggests that the cumulative effect of solar exposure should be considered in the early and middle stages. The cumulative effect has been suggested by other studies. For example, Foereid et al. (2010) concluded that the increasing litter degradability is a more important mechanism for photodegradation than direct light-

induced mass loss. King et al. (2012) further concluded that the significance of this facilitation effect heavily depends on length of exposure.

Compared to remaining carbon results, the DayCent-UV model showed larger discrepancy on remaining N, however it was able to predict the observed general pattern of N release with time (Figure 4.7 – averaged over species N release at CPER). The model performance on simulating individual species' nitrogen pattern is worse [Figure 4.5(b) and Figure 4.6(b)]. Some species such as PIRE and TRAE release N slower than observation, while some species such DRGL release N faster than observation in the entire experiment. In the current DayCent-UV model the relative C/N ratios between source and target pools and mineral N pools determines N flows between litter pools. Since *mdr* and *mti* influence the microbial pool size, the current DayCent-UV model has already indirectly incorporated the UV inhibition effects on microbial N immobilization (Henry et al. 2008; Smith et al. 2009; Lin and King 2014) and the UV facilitation effects by providing more microbial decomposable N compounds (Foereid et al. 2010). The only direct change for N in litter pools is when photodegradation releases C as CO₂ from surface structural, and the associated N flows into surface metabolic. The poorer performance on remaining N vs time for individual species indicates that the current model does not have enough mechanisms to represent species specific litter N dynamic in arid environment. It is important to note that the observed litter N release data is much more variable (Figure 4.4 shows large temporal changes in N release). There have been studies exploring some other potential mechanisms for N in high solar (UV) radiation environment. Some studies suggested that C-use efficiency may be reduced to allow net N release (Hewins et al. 2008; Brandt et al. 2010). Some studies suggested that direct N photo-dissolution or photodegradation may occur (Brandt et al. 2007; Mayer et al. 2012).

The DayCent-UV model matches the observed C remaining slightly better than the DayCent-Photosyn model (photo-off) in the early stage (i.e. 1-3 years) but matches much better in the later stage (i.e. 5-10 years) [Figure 4.7(a)]. Even though the two models show similar performance in the early stage, the mechanisms and the C distribution among the four surface litter pools are quite different. The DayCent-UV version has photodegradation that reduces surface structural and part of it flows into surface metabolic. The UV inhibition effect reduces the surface active pool and indirectly reduces the consumption of surface metabolic. The UV facilitation effect increases the CO₂ loss during the turnover between surface active and slow pools. As a result, we see that the DayCent-UV version shows significantly larger surface metabolic pool but significantly smaller surface active and slightly smaller surface structural and slow pools than the DayCent-Photosyn version (data not presented). The cumulated CO₂ loss from surface slow and the continuous photodegradation of surface structural cause lower surface litter C remaining in the DayCent-UV version.

The performance of DayCent-UV on N remaining is much better than that of DayCent-Photosyn especially in the later stage [Figure 4.7(b)]. The final remaining N fractions from DayCent-UV, DayCent-Photosyn, and observation are approximately 0.55, 0.90, and 0.45, respectively. The DayCent-UV generally simulated the persistent net N release found in observation due to the newly introduced N flow from surface structural to surface metabolic that reduces the intensity of N immobilization from extraneous sources.

There is a negative relationship between litter's initial lignin fraction (Table 4.2, column 6) and the individually optimized photodecay rate (Table 4.3, column 2, maxphoto). This suggested that lignin is not the chemical compound that is responsible for UV degradation. Some field studies did not observe increased lignin loss (Lin and King 2014) or did not find the change

of lignin (Brandt et al. 2007) under UV exposure. The photodegradation flows in DayCent-UV are imposed on standing dead and surface structural pools. Both pools have lignin and cellulose in common. Therefore, we speculate that cellulose is the major chemical compound for UV degradation. Some studies reported that cellulose and/or hemicellulose are responsible for litter mass loss under UV exposure (Rozema et al. 1997; Brandt et al. 2007; Brandt et al. 2010). Alternatively, we speculate that photodegradation breaks down encrusting lignin and exposes protected cellulose for biological decomposition (Henry et al. 2008; Austin and Ballaré, 2010; Brandt et al. 2010; Frouz et al. 2011).

DayCent-UV equilibrium model runs for the Colorado (CPER) site were used to evaluate the ecosystem impact of the adding photodegradation into the DayCent model. The results showed that aboveground and belowground plant production, surface net N mineralization, and surface litter N pool were increased by adding photodegradation, while surface litter C, soil net N mineralization and mineral soil C and N decreased (see Table 4.4). Photodegradation of standing dead and surface structural promotes direct C loss from the two pools, enhances the cellulose accessibility to microbial decomposition, and increases the amount of labile material entering the surface metabolic pool. The decline in mineral soil C and N and surface litter C is because more surface C is lost as CO₂ and less C and N is mixed from surface litter into the soil. Photodegradation greatly increases N mineralization from surface structural to surface metabolic and increases the total surface N pool because N stays in the litter during the photodecay flow. This also increases the net N mineralization in the surface pools because microbes need less extraneous mineral N to decompose high C/N ratio materials. Soil net N mineralization decreased because of the reduced input of C and N from surface litter layer into the mineral soil layer. The large increase in surface net N mineralization (+25%) more than compensates for the

slight reduction (-2.84 %) in soil N mineralization, and the total soil and surface net N mineralization slight increases.

Conclusions

The calibrated DayCent-UV model fitted the major patterns in observed first 20-cm soil water content, aboveground live biomass, and actual evapotranspiration (R^2 between 0.44 and 0.50) but missed some CO₂ spikes after heavy rain events in the observed net ecosystem exchange ($R^2 = 0.23$). Generally, the optimized DayCent-UV model fitted the observed remaining carbon vs time pattern well for both individual species and across species averages at three (semi-)arid LIDET sites and predicted the observed general pattern of nitrogen release with time. However, the model showed larger discrepancy on remaining nitrogen vs time for individual species, suggesting that some mechanisms of photodegradation on nitrogen dynamics may be missing. The slight overestimation of carbon release in the early stage (i.e. years 1-3) and the underestimation in the later stage suggested that the cumulative effect of solar exposure should be considered. The DayCent-UV model fitted the LIDET remaining carbon and nitrogen observation much better than the DayCent-Photosyn model (without the UV decomposition module) especially in the later stage. The negative relationship between litter's initial lignin fraction and the individually optimized photodecay rate suggested that cellulose rather than lignin may be the chemical compound that is responsible for UV degradation. The DayCent-UV equilibrium model runs showed that UV decomposition increased aboveground and belowground plant production, surface net N mineralization, and surface litter N pool, while decreased surface litter C, soil net N mineralization and mineral soil C and N.

Table 4.1 Climatic characteristic and ecosystem type for the three selected LIDET sites (Adair et al. 2008; Gholz et al. 2000). All climatic variables were averages of the 10-year LIDET study period (1990-1999). CDI_{LT} is the Lloyd & Taylor (1994) climate decomposition index. The terms “Lat.,” “Lon.,” and “Elev.” are the abbreviation of latitude, longitude, and elevation. The terms “MAT”, “MAP”, and “SR” stand for mean annual temperature, precipitation, and solar radiation. DEFAC is a complex climatic factor related to decomposition in the CENTURY model.

Site	Lat. (°)	Lon. (°)	Elev. (m)	MAT (°C)	MAP (mm)	SR W/m ²	AET (mm)	DEF AC	CDI_{LT}	Ecosystem Type
Central Plains Experimental Range (CPER)	40.82	104.77	1650	8.60	440	462.6	430	0.19	0.243	Dry Grassland
Sevilleta National Wildlife Refuge (SEV)	34.33	106.67	1572	13.17	255	520.6	252	0.10	0.136	Shrubland /Desert
Jornada Experimental Range (JRN)	32.50	106.75	1410	17.15	298	526.1	292	0.13	0.216	Shrubland /Desert

Table 4.2 Initial values of litter quality indices for the six common leaf litter species in the LIDET experiment (extracted from Adair et al. 2008)

Species	Litter type	Abbreviation	Water soluble extractives (%)	Cellulose (%)	Lignin (%)	C/N
Sugar Maple (<i>Acer saccharum</i>)	Broadleaf	ACSA	47.68	27.33	15.87	61.83
Drypetes (<i>Drypetes Glauca</i>)	Broadleaf	DRGL	40.23	39.82	10.91	24.25
Red Pine (<i>Pinus resinosa</i>)	Conifer	PIRE	20.60	44.58	19.18	92.72
Chestnut Oak (<i>Quercus prinus</i>)	Broadleaf	QUPR	27.22	39.38	23.51	50.55
Western Redcedar (<i>Thuja plicata</i>)	Conifer	THPL	22.31	35.92	26.67	83.12
Wheat (<i>Triticum aestivum</i>)	Gramminoid	TRAE	6.72	73.15	16.21	133.32

Table 4.3 The maxphoto values for the six litter species at Colorado (CPER) site were obtained by optimizing individual species using the original DayCent-UV model (column 2) and by optimizing across species using the modified DayCent-UV model (column 3). The RMSEs of carbon and nitrogen for each case are reported in parentheses.

Species	optimized on individual species (with original DayCent-UV model)	optimized across species (with modified DayCent-UV model)
ACSA	0.34672 (0.0952, 0.2717)	0.94693 (0.0953, 0.2741)
DRGL	0.97826 (0.1449, 0.3379)	1.31681 (0.1365, 0.3176)
PIRE	0.89735 (0.1735, 0.2295)	0.70043 (0.1643, 0.2571)
QUPR	0.64025 (0.1136, 0.1955)	0.37730 (0.1191, 0.1863)
THPL	0.00000 (0.1156, 0.1667)	0.14161 (0.1289, 0.1656)
TRAE	1.14962 (0.1703, 0.2794)	0.92173 (0.1649, 0.3157)

Table 4.4 List of 90-year average ecological variables (related to plant productivity, N mineralization, and surface and soil C and N pools) with and without photodecay.

	variables	photo_off	photo_on	%difference (on-off)/off x100%
Plant productivity	agcacc	48.733	49.28866	+1.140
	bgcjacc + bgcmacc	51.041	51.7886	+1.465
Surface net N mineralization	strmnr(1,1) + metmnr(1,1) + s1mnr(1,1) + s2mnr(1,1)	0.66921	0.83672	+25.031
Soil net N mineralization	strmnr(2,1) + metmnr(2,1) + s1mnr(2,1) + s2mnr(2,1) + s3mnr(1)	3.65661	3.552774	-2.840
Surface litter C pools	strcis(1,*) + metcis(1,*) + som1ci(1,*) + som2ci(1,*)	58.16837 + 22.37561 + 17.05395 + 16.38691 = 113.9848	20.66096 + 58.75235 + 4.02944 + 12.03130 = 95.47404	-16.240
Surface litter N pools	struce(1,1) + metabe(1,1) + som1e(1,1) + som2e(1,1)	0.29084 + 0.80096 + 1.09700 + 0.89816 = 3.08697	0.10331 + 2.30206 + 0.25246 + 0.65774 = 3.31556	+7.405
Surface biological decay rate	aagdefac	0.220543	0.220977	+0.197
Soil C pools	strcis(2,*) + metcis(2,*) + som1ci(2,*) + som2ci(2,*) + som3ci(*)	139.8343 + 12.8246 + 19.8004 + 346.1737 + 574.4206 = 1093.054	142.5519 + 13.01168 + 19.28496 + 310.4573 + 554.0435 = 1039.349	-4.913
Soil N pools	struce(2,1) + metabe(2,1) + som1e(2,1) + som2e(2,1) + som3e(1)	0.69917 + 1.03310 + 1.27231 + 15.84862 + 45.47730 = 64.3305	0.71276+ 1.05232 + 1.241061 + 13.96899 + 44.33035 = 61.30547	-4.702

Note: The term “photo_off” refers to the DayCent-Photosyn model. The term “photo_on” refers to the modified DayCent-UV model. If there are two asterisks in the parenthesis, the first one is related to the pool position: 1 denotes surface pools and 2 denotes soil pools. The right-most asterisk (*) in strcis(*,*) and other surface and soil pools may have two values: 1 represents unlabeled C and 2 represents labeled C. The variables “agcacc”, “bgcjacc”, and “bgcmacc” are annual accumulators. The variables "strcis(*,*)", "metcis(*,*)", "som1ci(*,*)", "som2ci(*,*)", "som3ci(*)" are pool sizes (state variables). The variables “strmnr(*,1)”, “metmnr(*,1)”, “s1mnr(*,1)”, “s2mnr(*,1)”, and “s3mnr(1)” are monthly rates.

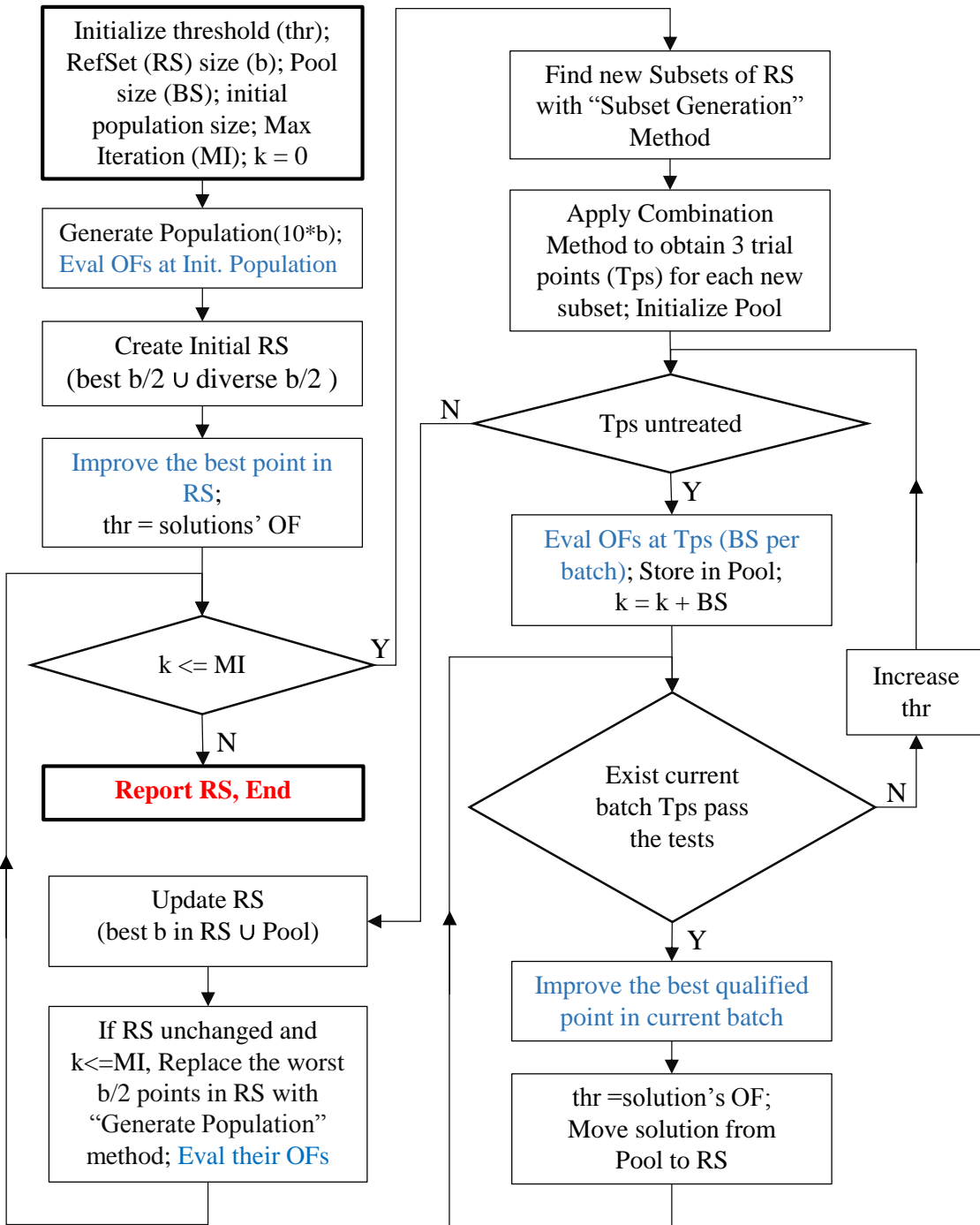


Figure 4.2 Flowchart of the modified scatter search algorithm for global optimization (derived from Ugray et al. 2007). The operations/procedures that use multi-threading technique to speed up the process are highlighted in blue color. The common feature of these operations is the time consuming evaluation of Objective Function (OF).

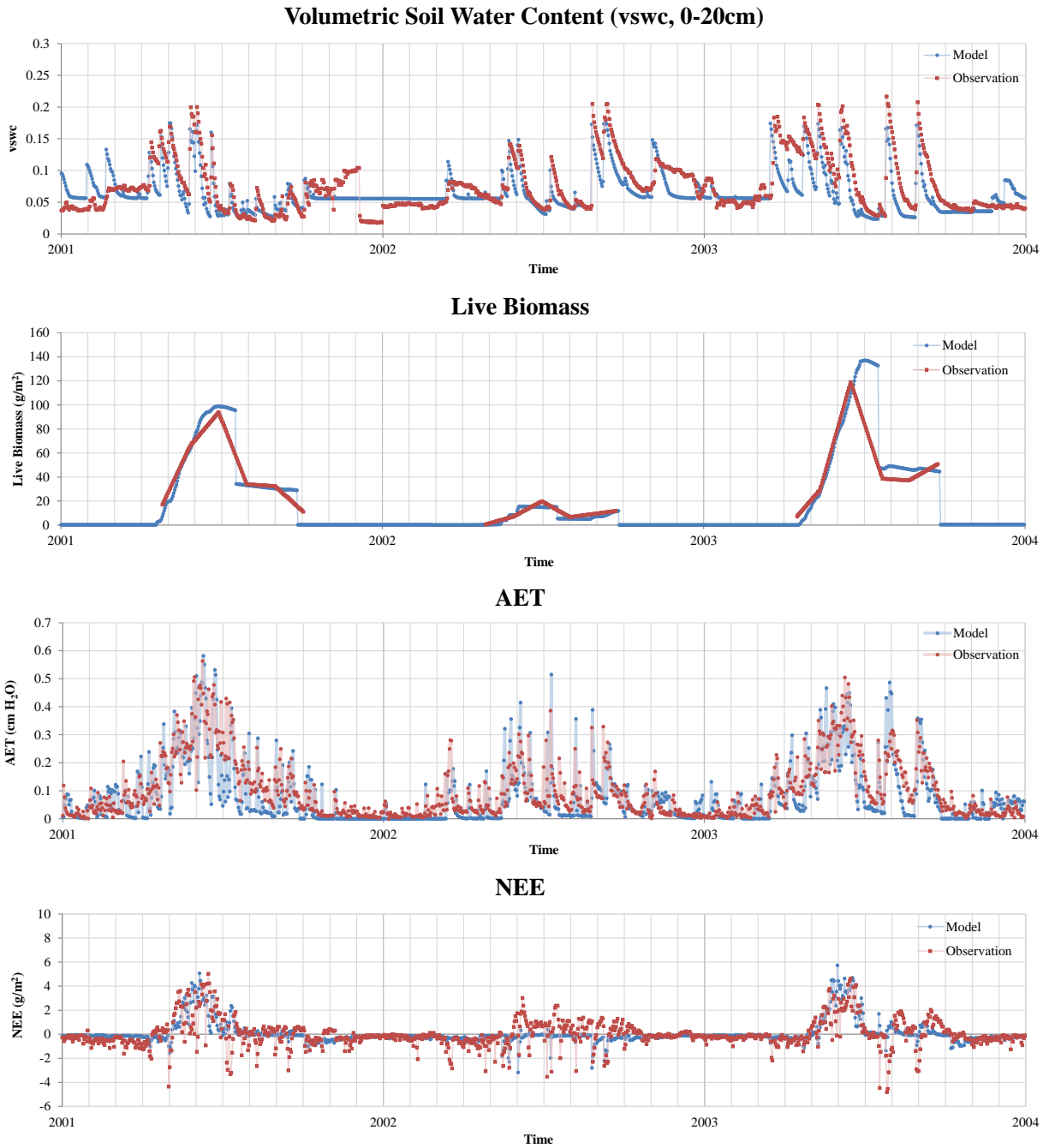


Figure 4.3 The time series of four modeled and observed ecological variables [volumetric soil water content in 0-20 cm soil (vswc), aboveground live biomass, actual evapotranspiration (AET), net ecosystem exchange (NEE)] at CPER (Colorado) site in 2001-2003.

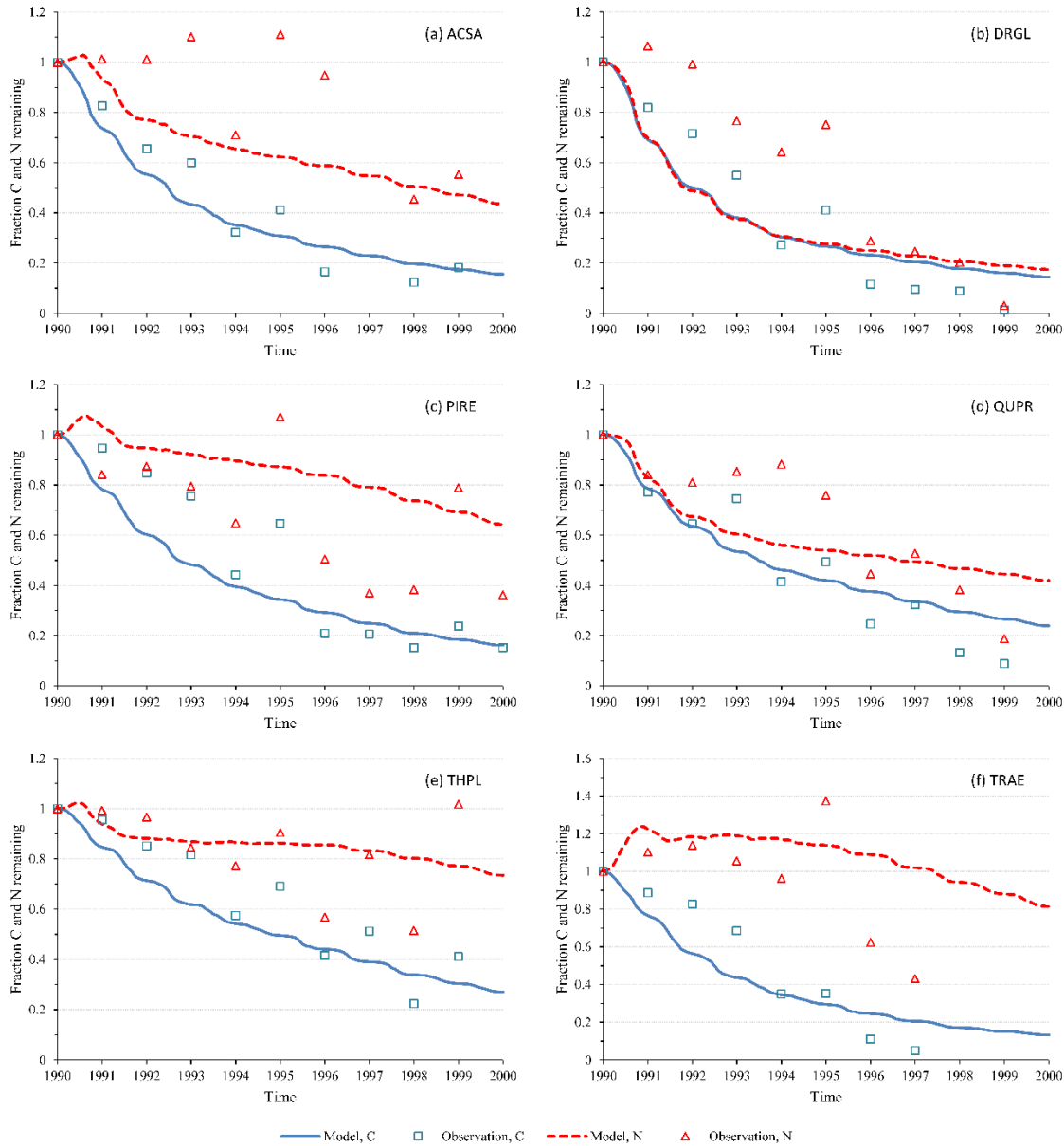


Figure 4.4 The time series of remaining C & N (fraction) in litter bags for six litter species (i.e. ACSA, DRGL, PIRE, QUPR, THPL, and TRAE) from the modified DayCent-UV model (solid lines for C and dashed lines for N) and from the annual observation of LIDET experiment (squares for C and triangles for N) at Colorado (CPER) site.

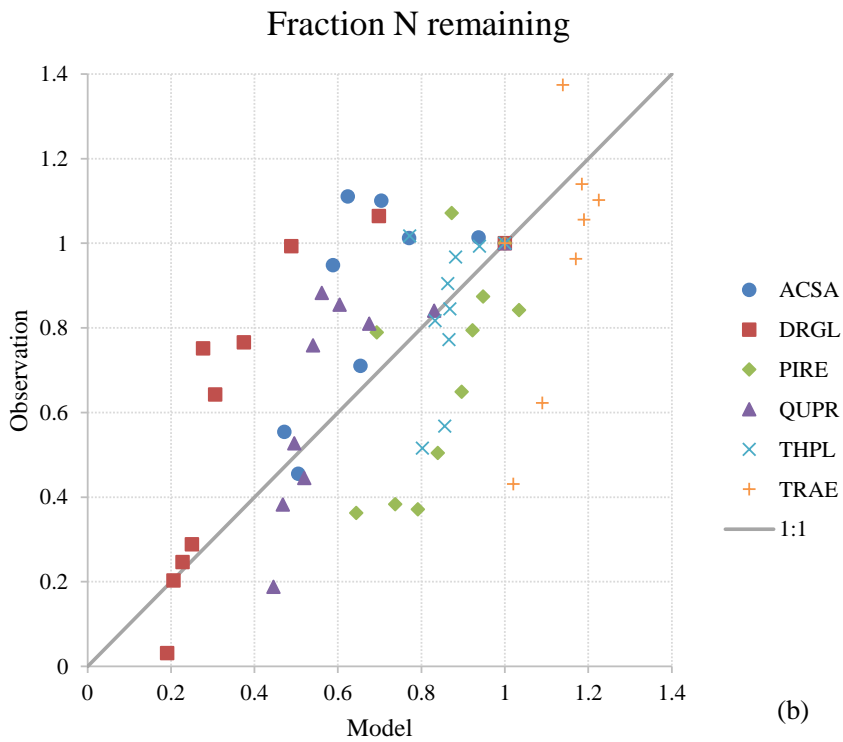
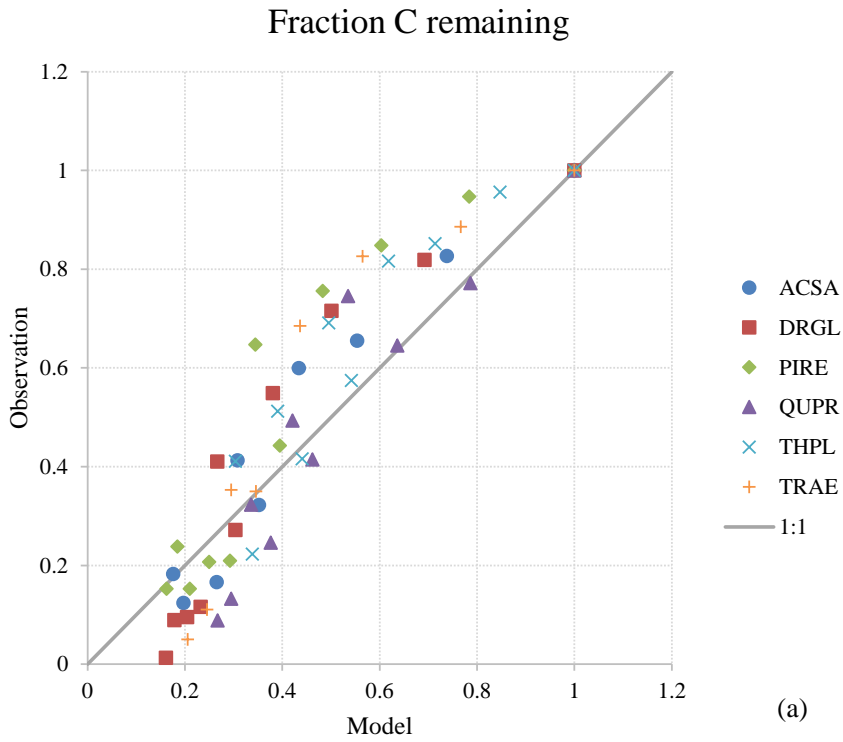


Figure 4.5 1:1 scatter plots of annual remaining C (a) and N (b) fraction between the modified DayCent-UV model and LIDET observation at six leaf litter species at Colorado (CPER) site.

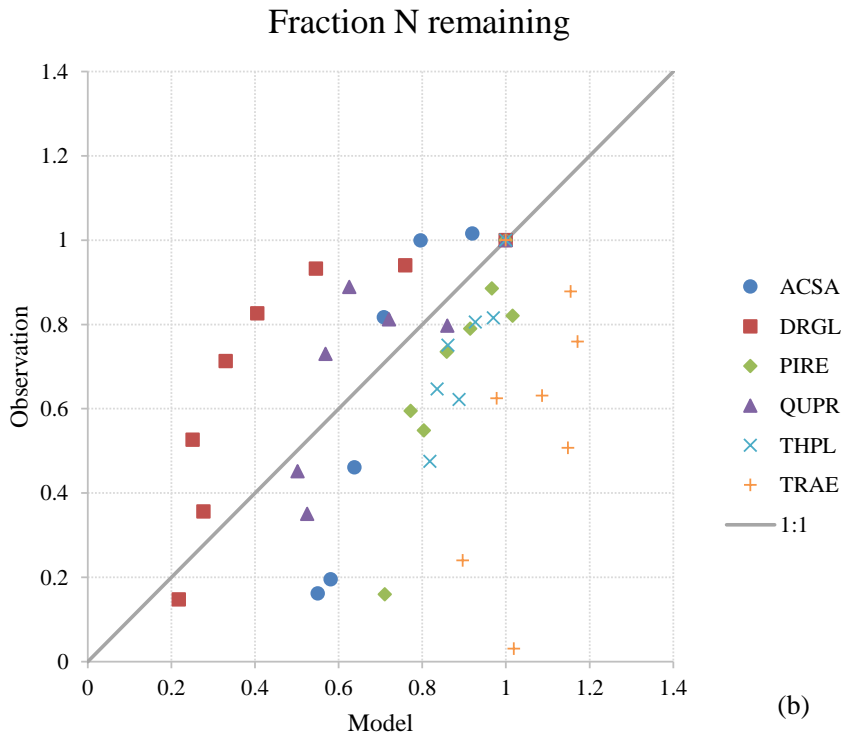
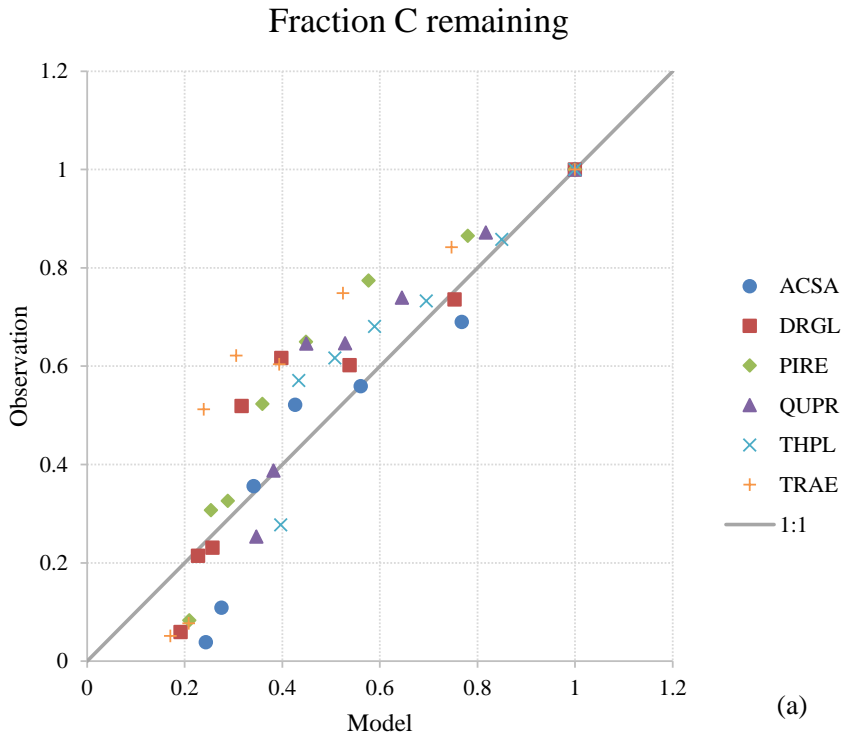
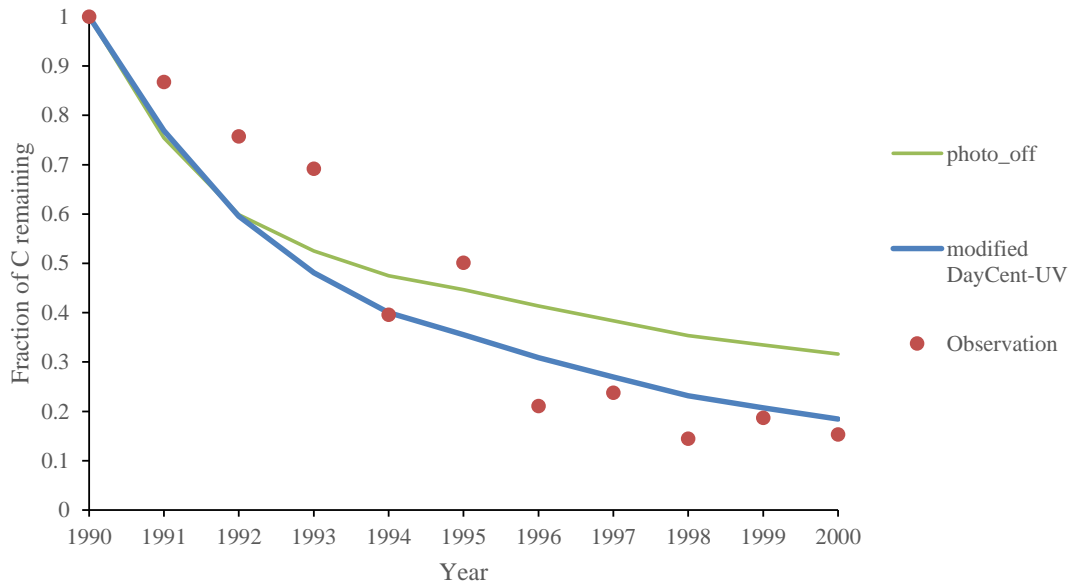


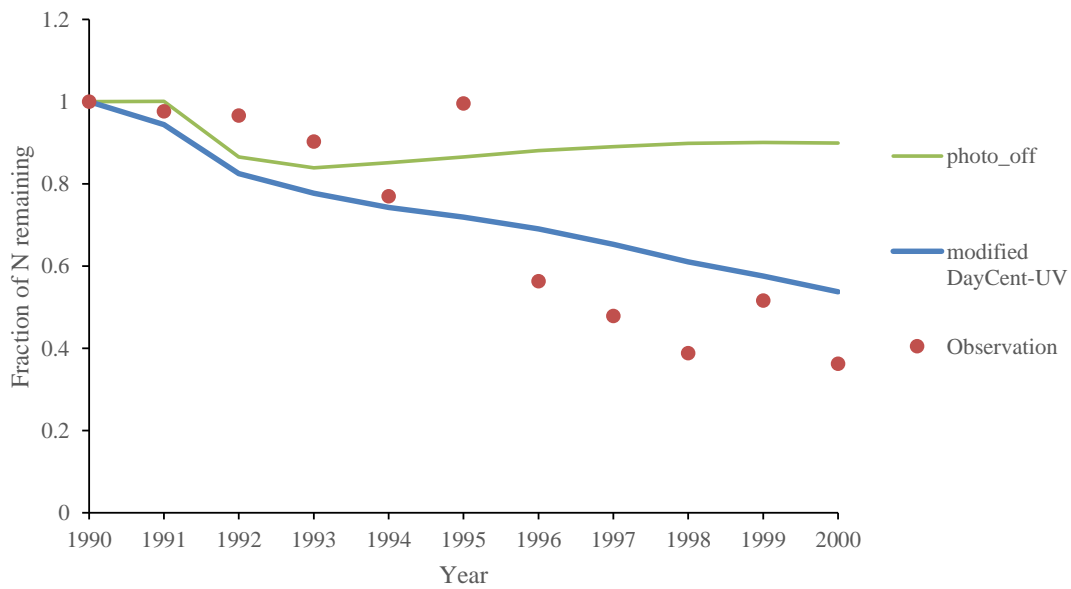
Figure 4.6 1:1 scatter plots of sites [Sevillaeta (SEV) and Jornada (JRN)] averaged annual remaining C (a) and N (b) fraction between the modified DayCent-UV model and LIDET observation at six leaf litter species.

Performance comparison of two DayCent versions (C)



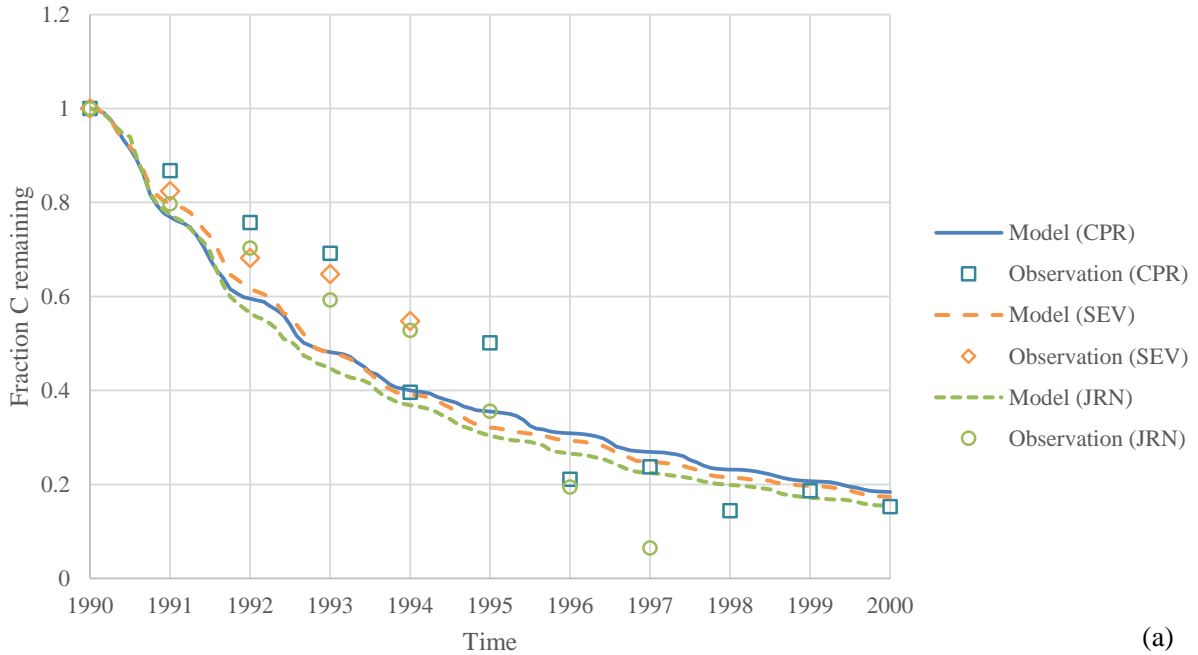
(a)

Performance comparison of two DayCent versions (N)

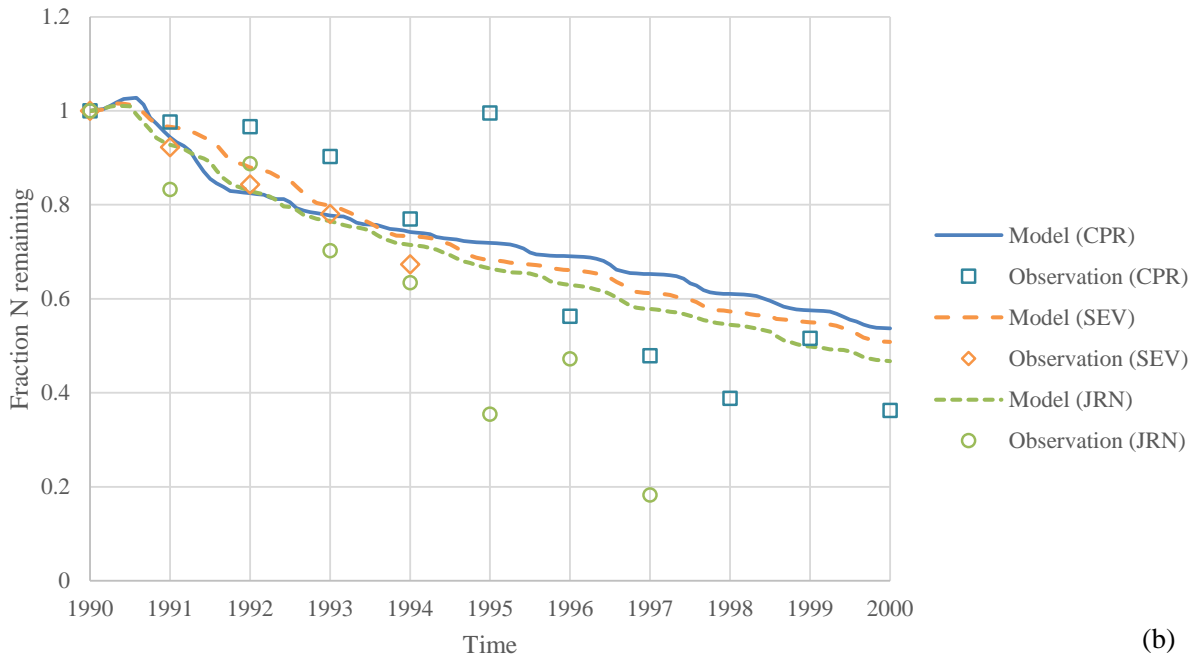


(b)

Figure 4.7 The across species average of remaining C (a) and N (b) at the Colorado (CPER) site from LIDET observations and DayCent models with (modified DayCent-UV) and without (DayCent-Photosyn or photo_off) UV decomposition modules.



(a)



(b)

Figure 4.8 The across species averages of remaining C fraction (a) and remaining N fraction (b) at three LIDET sites [Colorado (CPR), Sevilleta (SEV) and Jornada (JRN)] from modified DayCent-UV model (lines) and LIDET experiment observation (symbols).

REFERENCES

- Adair E C, Parton W J, Del Grosso S J, Silver W L, Harmon M E, Hall S A, Burke I C, Hart S C (2008), Simple three-pool model accurately describes patterns of long-term litter decomposition in diverse climates. *Global Change Biology*, 14: 2636–2660. doi: 10.1111/j.1365-2486.2008.01674.x
- Adair E C, Parton W J, King J Y, Brandt L, Harmon M E (2015), Accounting for photodegradation dramatically improves prediction of carbon and nitrogen losses in arid systems. (In prep.)
- Andrady A L, Hamid H, Torikai A (2011), Effects of solar UV and climate change on materials. *Photochemical & Photobiological Sciences*, 10(2): 292-300. doi: 10.1039/C0PP90038A
- Austin A T (2011), Has water limited our imagination for aridland biogeochemistry? *Trends in Ecology and Evolution*, 26(5): 229-235. doi: 10.1016/j.tree.2011.02.003
- Austin A T, Vivanco L (2006), Plant litter decomposition in a semi-arid ecosystem controlled by photodegradation. *Nature*, 442(7102): 555-558. doi: 10.1038/nature05038
- Austin A, Ballaré C (2010), Dual role of lignin in plant litter decomposition in terrestrial ecosystems. *Proceedings of the National Academy of Sciences of the United States of America*, 107(10): 4618-4622. doi: 10.1073/pnas.0909396107
- Bonan G B, Hartman M D, Parton W J, Wieder W R (2013), Evaluating litter decomposition in earth system models with long-term litterbag experiments: an example using the Community Land Model version 4 (CLM4). *Global Change Biology*, 19: 957–974. doi: 10.1111/gcb.12031
- Bond-Lamberty B, Thomson A M (2010), Temperature-associated increases in the global soil respiration record, *Nature*, 464(7288): 579-582. doi:10.1038/nature08930
- Brandt L A, Bohnet C, King J Y (2009), Photochemically induced carbon dioxide production as a mechanism for carbon loss from plant litter in arid ecosystems. *Journal of Geophysical Research*, 114: G02004. doi: 10.1029/2008JG000772
- Brandt L A, King, J Y, Hobbie S E, Milchunas D G, Sinsabaugh R L (2010), The Role of Photodegradation in Surface Litter Decomposition Across a Grassland Ecosystem Precipitation Gradient. *Ecosystems*, 13(5): 765-781. doi: 10.1007/S10021-010-9353-2
- Brandt L A, King, J Y, Milchunas D G (2007), Effects of ultraviolet radiation on litter decomposition depend on precipitation and litter chemistry in a shortgrass steppe ecosystem. *Global Change Biology*, 13(10): 2193-2205. doi: 10.1111/j.1365-2486.2007.01428.x

- Braswell B H, Sacks W J, Linder E, Schimel D S (2005), Estimating diurnal to annual ecosystem parameters by synthesis of a carbon flux model with eddy covariance net ecosystem exchange observations. *Global Change Biology*, 11(2): 335-355. doi: 10.1111/j.1365-2486.2005.00897.x
- Burnham K P, Anderson D R (2002), *Model selection and multimodel inference: A practical information-theoretic approach* (2nd ed.). New York: Springer
- Cory R M, McNeill K, Cotner J P, Amado A, Purcell J M, Marshall A G (2010), Singlet Oxygen in the Coupled Photochemical and Biochemical Oxidation of Dissolved Organic Matter. *Environmental Science & Technology*, 44(10): 3683-3689. DOI: 10.1021/es902989y
- Day T A, Zhang E T, Ruhland C T (2007), Exposure to solar UV-B radiation accelerates mass and lignin loss of *Larrea tridentata* litter in the Sonoran Desert. *Plant Ecology*, 193(2): 185-194. doi: 10.1007/s11258-006-9257-6
- Del Grosso S J, Halvorson A D, Parton W J (2008), Testing DAYCENT model simulations of corn yields and nitrous oxide emissions in irrigated tillage systems in Colorado. *Journal of Environmental Quality*, 37(4): 1383-1389. doi: 10.2134/jeq2007.0292
- Del Grosso S J, Mosier A R, Parton W J, Ojima D S (2005), DAYCENT model analysis of past and contemporary soil N₂O and net greenhouse gas flux for major crops in the USA. *Soil and Tillage Research*, 83(1): 9-24. doi: 10.1016/j.still.2005.02.007
- Del Grosso S J, Parton W J, Keough C A, Reyes-Fox M (2011). Special Features of the DayCent Modeling Package and Additional Procedures for Parameterization, Calibration, Validation, and Applications. In L. R. Ahuja, L. Ma (Eds.), *Methods of Introducing System Models into Agricultural Research* (pp. 155-176). Madison, WI: American Society of Agronomy
- Del Grosso S J, Parton W J, Mosier A R, Hartman M D, Brenner J, Ojima D S, Schimel, D S (2001). Simulated interaction of carbon dynamics and nitrogen trace gas fluxes using the DAYCENT model. In M. Schaffer et al. (Eds.), *Modeling carbon and nitrogen dynamics for soil management* (pp. 303-332). Boca Raton, FL: CRC Press. doi: 10.1201/9781420032635.ch8
- Del Grosso S J, Parton W J, Mosier A R, Ojima D S, Kulmala A E, Phongpan S (2000), General model for N₂O and N₂ gas emissions from soils due to denitrification. *Global Biogeochem. Cycles*, 14(4): 1045–1060. doi: 10.1029/1999GB001225
- Dirks I, Navon Y, Kanas D, Dumbur R, Grünzweig J M (2010), Atmospheric water vapor as driver of litter decomposition in Mediterranean shrubland and grassland during rainless seasons. *Global Change Biology*, 16(10): 2799-2812. doi: 10.1111/j.1365-2486.2010.02172.x
- Feng X, Hills K M, Simpson A J, Whalen J K, Simpson M J (2011), the role of biodegradation and photo-oxidation in the transformation of terrigenous organic matter. *Organic Geochemistry*, 42(3): 262-274. doi: 10.1016/j.orggeochem.2011.01.002

- Foereid B, Bellarby J, Meier-Augenstein W, Kemp H (2010), Does light exposure make plant litter more degradable? *Plant and Soil*, 333(1-2): 275-285. doi: 10.1007/s11104-010-0342-1
- Foereid B, Rivero M J, Primo O, Ortiz I (2011), Modelling photodegradation in the global carbon cycle. *Soil Biology & Biochemistry*, 43(6): 1383-1386. doi: 10.1016/j.soilbio.2011.03.004
- Frouz J, Cajthaml T, Mudrak O (2011), The effect of lignin photodegradation on decomposability of *Calamagrostis epigeios* grass litter. *Biodegradation*, 22(6): 1247-1254. doi: 10.1007/s10532-011-9479-8
- Gallo M E, Porrás-Alfaro A, Odenbach K J, Sinsabaugh R L (2009), Photoacceleration of plant litter decomposition in an arid environment. *Soil Biology & Biochemistry*, 41(7): 1433-1441. doi: 10.1016/j.soilbio.2009.03.025
- Gallo M E, Sinsabaugh R L, Cabaniss S E (2006), The role of ultraviolet radiation in litter decomposition in arid ecosystems. *Applied Soil Ecology*, 34(1): 82-91. doi: 10.1016/j.apsoil.2005.12.006
- Gehrke C, Johanson U, Callaghan T V, Chadwick D, Robinson C H (1995), The Impact of Enhanced Ultraviolet-B Radiation on Litter Quality and Decomposition Processes in *Vaccinium* Leaves from the Subarctic. *Oikos*, 72(2): 213-222. doi: 10.2307/3546223
- George B, Suttie E, Merlin A, Deglise X (2005), Photodegradation and photostabilisation of wood – the state of the art. *Polymer Degradation and Stability*, 88(2): 268-274. doi: 10.1016/j.polymdegradstab.2004.10.018
- Gholz H L, Wedin D A, Smitherman S M, Harmon M E, Parton W J (2000), Long-term dynamics of pine and hardwood litter in contrasting environments: toward a global model of decomposition. *Global Change Biology*, 6(7): 751–765. doi: 10.1046/j.1365-2486.2000.00349.x
- Glover F (1977), Heuristics for Integer Programming Using Surrogate Constraints. *Decision Sciences*, 8(1): 156–166. doi: 10.1111/j.1540-5915.1977.tb01074.x
- Glover F (1998), A Template for Scatter Search and Path Relinking. In J K Hao, E Lutton, E Ronald, M Schoenauer and D Snyers (Eds.), *Artificial Evolution*, Lecture Notes in Computer Science, 1363 (pp. 13-54). Springer
- Glover F, Lagunai M, Martí R (2000), Fundamentals of scatter search and path relinking. *Control and Cybernetics*, 29(3): 653-684
- Harmon M E, Bond-Lamberty B, Tang J, Vargas R (2011), Heterotrophic respiration in disturbed forests: A review with examples from North America. *J. Geophys. Res.*, 116: G00K04. doi:10.1029/2010JG001495

- Heisler-White J L, Knapp A K, Kelly E F (2008), Increasing precipitation event size increases aboveground net primary productivity in a semi-arid grassland. *OECOLOGIA*, 158(1): 129-140. doi: 10.1007/s00442-008-1116-9
- Henry H A L, Brizgys K, Field C B (2008), Litter decomposition in a california annual grassland: Interactions between photodegradation and litter layer thickness. *Ecosystems*, 11(4): 545-554. doi: 10.1007/s10021-008-9141-4
- Hewins D B, Archer S R, Okin G S, McCulley R L, Throop H L (2013), Soil-Litter Mixing Accelerates Decomposition in a Chihuahuan Desert Grassland. *Ecosystems*, 16(2): 183-195. doi: 10.1007/s10021-012-9604-5
- Hobbie S E (2005), Contrasting effects of substrate and fertilizer nitrogen on the early stages of litter decomposition. *Ecosystems*, 8(6): 644-656. doi: 10.1007/s10021-003-0110-7
- Hughes K A, Lawley B, Newsham K K (2003), Solar UV-B radiation inhibits the growth of antarctic terrestrial fungi. *Applied and Environmental Microbiology*, 69(3): 1488-1491. doi: 10.1128/AEM.69.3.1488-1491.2003
- Irmak S, Istanbuluoglu E, Irmak A (2008), An Evaluation of Evapotranspiration Model Complexity against Performance in Comparison with Bowen Ratio Energy Balance Measurements. *Transactions of the ASABE*, 51(4): 1295-1310
- King J Y, Brandt L A, Adair E C (2012), Shedding light on plant litter decomposition: Advances, implications and new directions in understanding the role of photodegradation. *Biogeochemistry*, 111(1-3): 57-81. doi: 10.1007/s10533-012-9737-9
- Laguna M, Martí R (2002), The OptQuest callable library. In S Voss, D Woodruff (Eds.), *Optimization Software Class Libraries*, (pp. 193–218). Boston: Kluwer Academic Publishers
- Laguna M, Martí R (2003), *Scatter search: Methodology and implementations in C*. Boston: Kluwer Academic Publishers
- Lee H, Rahn T, Throop H (2012), An accounting of C-based trace gas release during abiotic plant litter degradation. *Global Change Biology*, 18(3): 1185–1195. doi: 10.1111/j.1365-2486.2011.02579.x
- Lin Y, King J Y (2014), Effects of UV Exposure and Litter Position on Decomposition in a California Grassland. *Ecosystems*, 17(1): 158-168. doi: 10.1007/s10021-013-9712-x
- Liu S, Hu R, Cai G, Lin S, Zhao J, Li Y (2014), The role of UV-B radiation and precipitation on straw decomposition and topsoil C turnover. *Soil Biology & Biochemistry*, 77: 197–202. doi: 10.1016/j.soilbio.2014.06.009
- Lloyd J, Taylor J A (1994), On the Temperature Dependence of Soil Respiration. *Functional Ecology*, 8(3): 315-323

- Long-Term Intersite Decomposition Experiment Team (LIDET) (1995), Meeting the Challenge of Long-Term, Broad-Scale Ecological Experiments. Publication No. 19. LTER Network Office: Seattle, WA
- Ma S Y, Baldocchi D D, Hatala J A, Detto M, Yuste J C (2012), Are rain-induced ecosystem respiration pulses enhanced by legacies of antecedent photodegradation in semi-arid environments? *Agricultural and Forest Meteorology*, 154: 203-213. doi: 10.1016/j.agrformet.2011.11.007
- Martí R, Laguna M, Glover F (2006), Principles of scatter search, *European Journal of Operational Research*, 169(2): 359-372. doi:10.1016/j.ejor.2004.08.004
- Mayer L M, Thornton K R, Schick L L, Jastrow J D, Harden J W (2012), Photodissolution of soil organic matter. *Geoderma*, 170: 314-321. doi: 10.1016/j.geoderma.2011.11.030
- Messenger D J, Mcleod A R, Fry S C (2009), The role of ultraviolet radiation, photosensitizers, reactive oxygen species and ester groups in mechanisms of methane formation from pectin. *Plant, Cell & Environment*, 32(1): 1–9. doi: 10.1111/j.1365-3040.2008.01892.x
- Mlambo D, Mwenje E (2010), Influence of *Colophospermum mopane* canopy cover on litter decomposition and nutrient dynamics in a semi-arid African savannah. *African Journal of Ecology*, 48(4): 1021-1029. doi: 10.1111/j.1365-2028.2010.01208.x
- Moody S A, Paul N D, Bjorn L O, Callaghan T V, Lee J A, Manetas Y, Rozema J, Gwynn-Jones D, Johanson U, Kyparissis A, Oudejans A M C (2001), The direct effects of UV-B radiation on *Betula pubescens* litter decomposing at four European field sites. *Plant Ecology*, 154,(1-2): 27-36. doi: 10.1023/A:1012965610170
- Moorhead D L, Callaghan T (1994), Effects of increasing ultraviolet B radiation on decomposition and soil organic matter dynamics: a synthesis and modelling study. *Biology and Fertility of Soils*, 18(1): 19-26. doi: 10.1007/BF00336439
- Moyano F E, Manzoni S, Chenu C (2013), Responses of soil heterotrophic respiration to moisture availability: An exploration of processes and models. *Soil Biology & Biochemistry*, 59: 72-85. doi: 10.1016/j.soilbio.2013.01.002
- Naderi B, Ruiz R (2014), A scatter search algorithm for the distributed permutation flowshop scheduling problem. *European Journal of Operational Research*, 239(2): 323-334. doi: 10.1016/j.ejor.2014.05.024
- Pancotto V A, Sala O E, Cabello M, López N I, Robson T M, Ballaré C L, Caldwell M M, Scopel A L (2003), Solar UV-B decreases decomposition in herbaceous plant litter in Tierra del Fuego, Argentina: potential role of an altered decomposer community. *Global Change Biology*, 9(10): 1465–1474. doi: 10.1046/j.1365-2486.2003.00667.x
- Pancotto V A, Sala O E, Robson T M, Caldwell M M, Scopel A L (2005), Direct and indirect effects of solar ultraviolet-B radiation on long-term decomposition. *Global Change Biology*. 11(11): 1982-1989. doi: 10.1111/j.1365-2486.2005.01027.x

- Parton W J, Holland E A, Del Grosso S J, Hartman M D, Martin R E, Mosier A R, Ojima D S, Schimel D S (2001), Generalized model for NO_x and N₂O emissions from soils. *Journal of Geophysical Research*, 106(D15): 17403–17419. doi:10.1029/2001JD900101
- Parton W J, Schimel D S, Cole C V, Ojima D S (1987), Analysis of factors controlling soil organic levels of grasslands in the Great Plains. *Soil Science Society of America Journal*, 51(5): 1173-1179. doi:10.2136/sssaj1987.03615995005100050015x
- Parton W J, Scholes R J, Day K, Carter J O, Kelly R (2011), CENTURY-SAVANNA Model for Tree-Grass Ecosystems. In M J Hill, N P Hanan (Eds.), *Ecosystem function in Savannas: Measurement and modeling at landscape to global scale* (pp. 443-446). Boca Raton, CRC Press
- Parton W J, Stewart J W B, Cole C V (1988), Dynamics of C, N, P and S in grassland soils - a model. *Biogeochemistry*, 5(1): 109-131. doi: 10.1007/BF02180320
- Parton W, Morgan J, Smith D, Del Grosso S, Prihodko L, Lecain D, Kelly R, Lutz S (2012), Impact of precipitation dynamics on net ecosystem productivity. *Global Change Biology*, 18(3): 915-927. doi: 10.1111/j.1365-2486.2011.02611.x
- Parton W, Silver W L, Burke I C, Grassens L, Harmon M E, Currie W S, King J Y, Adair E C, Brandt L A, Hart S C, Fasth B (2007), Global-Scale Similarities in Nitrogen Release Patterns During Long-Term Decomposition. *Science*, 315(5810): 361–364. doi: 10.1126/science.1134853
- Peters D P C, Laney C M, Lugo A E, Collins L C, Driscoll C T, Groffman P M, Grove J M, Knapp A K, Kratz T K, Ohman M D, Waide R B, Yao J (2013), Long-Term Trends in Ecological Systems: A Basis for Understanding Responses to Global Change. U.S. Department of Agriculture, Technical Bulletin Number 1931
- Rozema J, Tosserams M, Nelissen H, van Heerwaarden L, Broekman R A, Flierman N (1997), Stratospheric ozone reduction and ecosystem processes: Enhanced UV-B radiation affects chemical quality and decomposition of leaves of the dune grassland species *calamagrostis epigeios*. *Plant Ecology*, 128(1-2): 285-294. doi: 10.1023/A:1009723210062
- Rutledge S, Campbell D I, Baldocchi D, Schipper L A (2010), Photodegradation leads to increased carbon dioxide losses from terrestrial organic matter. *Global Change Biology*, 16(11): 3065–3074. doi: 10.1111/j.1365-2486.2009.02149.x
- Savage K E, Parton W J, Davidson E A, Trumbore S E, Frey S D (2013), Long-term changes in forest carbon under temperature and nitrogen amendments in a temperate northern hardwood forest. *Global Change Biology*, 19(8): 2389–2400. doi: 10.1111/gcb.12224
- Smith W K, Gao W, Steltzer H, Wallenstein M D, Tree R (2010), Moisture availability influences the effect of ultraviolet-B radiation on leaf litter decomposition. *Global Change Biology*, 16: 484–495. doi: 10.1111/j.1365-2486.2009.01973.x

- Song X, Zhang H, Jiang H, Donaldson L A, Wang H (2013), Influence of elevated UV-B radiation on leaf litter chemistry and subsequent decomposition in humid subtropical China. *Journal of Soils and Sediments*, 13(5): 846-853. doi: 10.1007/s11368-013-0661-y
- Stehfest E, Heistermann M, Priess J A, Ojima D S, Alcamo J (2007), Simulation of global crop production with the ecosystem model DayCent. *Ecological Modelling*, 209(2-4): 203-219. doi: 10.1016/j.ecolmodel.2007.06.028
- Straube J R (2011), Integration of variable photosynthetic capacity into a biogeochemical model. Master's Thesis. Colorado State University, Fort Collins, CO. Retrieved from <http://hdl.handle.net/10217/70831>
- Swift M J, Heal O W, Anderson J M (1979), *Decomposition in terrestrial ecosystems*. Berkeley: University of California Press
- Ugray Z, Lasdon L, Plummer J, Glover F, Kelly J, Martí R (2007), Scatter Search and Local NLP Solvers: A Multistart Framework for Global Optimization. *INFORMS Journal On Computing*, 19(3): 328-340. doi:10.1287/ijoc.1060.0175
- Vähätalo A, Søndergaard M, Schlüter L, Markager S (1998), Impact of solar radiation on the decomposition of detrital leaves of eelgrass *Zostera marina*. *Marine Ecology Progress Series*, 170: 107-117. doi: 10.3354/meps170107
- Vanderbilt K L, White C S, Hopkins O, Craig J A (2008), Aboveground decomposition in and environments: Results of a long-term study in central New Mexico. *Journal of Arid Environments*, 72(5): 696-709. doi:10.1016/j.jaridenv.2007.10.010
- Zepp R G, Callaghan T V, Erickson D J (1998), Effects of enhanced solar ultraviolet radiation on biogeochemical cycles. *Journal of Photochemistry and Photobiology B: Biology*, 46(1-3): 69-82. doi: 10.1016/S1011-1344(98)00186-9
- Zhao H, Huang G, Ma J, Li Y, Tang L (2014), Decomposition of aboveground and root litter for three desert herbs: mass loss and dynamics of mineral nutrients. *Biology and Fertility of Soils*, 50(5): 745-753. doi: 10.1007/s00374-013-0892-5

APPENDIX 4.A MECHANISM OF C AND N FLUXES BETWEEN LITTER AND SOIL
ORGANIC POOLS IN DAYCENT

Bonan et al. (2013) summarized the C and N fluxes between discrete litter and soil organic matter pools.

The total C flux out of a source pool ($F_{S,o}^C$) is expressed as

$$F_{S,o}^C = C_S \times Br_S \times Er_S \quad (4.4)$$

where, C_S is the amount of C in the source pool S ; Br_S (set in the fix.100 by user) is the constant base loss rate for pool S ; and Er_S is the adjustment coefficient for abiotic factors, which include temperature, moisture, and soil pH. The total C flow into a receiver pool from the source pool S ($F_{R,i}^C$) is expressed as

$$F_{R,i}^C = F_{S,o}^C \times (1 - Mr_S) \times f_{S \rightarrow R} \quad (4.5)$$

where, Mr_S is the C loss rate due to microbial respiration; and $f_{S \rightarrow R}$ is the proportion of source pool C that flows to the receiver pool R . For source pools containing both lignin and cellulose (i.e. standing dead and surface structural), $f_{S \rightarrow R}$ is a function of lignin content or lignin/N ratio.

The N fluxes are associated with the corresponding C fluxes and diagnosed from the C/N ratios of the source and receiver pools.

The total N flux out of a source pool ($F_{S,o}^N$) is expressed as

$$F_{S,o}^N = F_{S,o}^C \times (N/C)_S \quad (4.6)$$

where, $(N/C)_S$ is the N/C ratio of the source pool S . The total N flux into a receiver pool R from the source pool S ($F_{R,i}^N$) is expressed as

$$F_{R,i}^N = F_{R,i}^C \times (N/C)_R \quad (4.7)$$

where, $(N/C)_R$ is the N/C ratio of the receiver pool R . When the input N is more than the receiver pool's demand (i.e. the source C/N ratio lower than the receiver C/N ratio), the excess is mineralized by respiration. When the input N is less than the receiver pool's demand (i.e. the source C/N ratio higher than the receiver C/N ratio), the deficiency is immobilized from exogenous N in the environment. DayCent treats the mineral N in the top soil layer as the source of exogenous N. The immobilization is always allowed unless there is no top soil mineral N left (Bonan et al. 2013). DayCent uses the mineral N in the top soil layer at the time and a set of piecewise linear functions to determine the C/N ratio in the receiver pools at that time.

Literature Cited

Bonan G B, Hartman M D, Parton W J, Wieder W R (2013), Evaluating litter decomposition in earth system models with long-term litterbag experiments: an example using the Community Land Model version 4 (CLM4). *Global Change Biology*, 19: 957–974. doi: 10.1111/gcb.12031

APPENDIX 4.B DAYCENT-UV EQUATIONS

In DayCent-UV, the C of photodegradable materials (i.e. lignin and cellulose) in litter is partly photodegraded ($F_{Photo}^{C,LT}$) and removed from its original pool (Adair et al. 2015):

$$F_{Photo}^{C,LT} = (SR_{soil} \cdot c_{Abs}^{LT}) \cdot p \quad (4.8)$$

where, the capital letter C refers to carbon. The string LT refers to standing dead or surface structural litter. The string $Photo$ refers to photodegradation. p is the maximum daily photodecay rate [$\text{maxphoto}, \mu g (C) / KJ (SR_{soil})$]. Adair et al. 2015 reported that both standing dead and structural have the same $p = 1.6 [\mu g (C) / KJ (SR_{soil})]$. In this study, p is a function of litter's initial lignin fraction $p = p_0 + f_{Lignin}^{Initial} \times p_1$, where p_0 ($\text{maxphoto_intercept}$) is the maximum daily photodecay rate when the lignin fraction equal to zero, $f_{Lignin}^{Initial}$ is the litter's initial lignin fraction, and p_1 (maxphoto_slp) is the change of maximum photodecay rate per unit initial lignin fraction. If the calculated p is less than zero, p is set to zero. SR_{soil} is the daily soil surface solar radiation (KJ). c_{Abs}^{LT} is the litter absorption coefficient. DayCent-UV assumes that the higher the litter biomass, the more light is intercepted by litter. If the litter refers to standing dead, then it is the absorption coefficient of standing dead: c_{Abs}^{SD} . If the litter refers to surface structural, then it is the absorption coefficient of surface structural: c_{Abs}^{SFS} . The calculation of c_{Abs}^{SD} and c_{Abs}^{SFS} follows a similar piece-wise linear function,

$$\begin{aligned}
c_{Abs}^{SD} &= \begin{cases} \frac{Biom^{SD}}{Biom_{full_abs}} & , Biom^{SD} < Biom_{full_abs} \\ 1 & , Biom^{SD} \geq Biom_{full_abs} \end{cases} \\
c_{Abs}^{SFS} &= \begin{cases} \frac{Biom^{SFS}}{Biom_{full_abs}} & , Biom^{SFS} < Biom_{full_abs} \\ 1 & , Biom^{SFS} \geq Biom_{full_abs} \end{cases}
\end{aligned} \tag{4.9}$$

where, $Biom^{SD}$ and $Biom^{SFS}$ are the biomass of standing dead and surface structural, respectively.

$Biom_{full_abs}$ is the minimum biomass that fully absorbs solar radiation. If litter biomass is greater than $Biom_{full_abs}$, then all solar radiation is intercepted. The model assumes the excess litter is no longer exposed to light on soil surface and photodegradation plateaus (Adair et al. 2015).

DayCent-UV currently sets $Biom_{full_abs} = 200g$.

A fraction (f or $f_{photoco2}$) of the photodegraded C ($F_{Photo}^{C,LT}$) is lost as CO_2 ($F_{Photo}^{CO_2,LT}$),

$$F_{Photo}^{CO_2,LT} = F_{Photo}^{C,LT} \cdot f \tag{4.10}$$

where, Adair et al. 2015 reported that the value of $f_{photoco2}$ is 0.48. Unlike the CO_2 loss due to respiration, there is no N loss associated with $F_{Photo}^{CO_2,LT}$.

The remaining photodegraded C from surface structural flows into surface metabolic (Adair et al. 2015). Since there is no metabolic standing dead pool, the remaining photodegraded C from standing dead flows back to standing dead (Adair et al. 2015). The associated N flows are still determined using the DayCent strategies summarized by Bonan et al. (2013).

In DayCent-UV, the decomposition rate of the surface metabolic is still the product of its current pool size ($C_{Metabolic}$), its base decomposition rate ($Br_{Metabolic}$), and traditional abiotic factors ($Er_{Metabolic}$) such as T , θ , and pH , but is reduced by higher solar radiation via the metabolic decomposition reducer (mdr):

$$F_{Metabolic,o}^C = C_{Metabolic} \times Br_{Metabolic} \times Er_{Metabolic} \times mdr \quad (4.11)$$

where, mdr is a piecewise linear function as a function of soil surface solar radiation (SR_{soil}),

$$mdr = \begin{cases} 1.0 & , SR_{soil} \leq 0 \\ 0.2 & , SR_{soil} > 3 \times 10^4 \\ b + \left| \frac{b-a}{x_2 - x_1} \right| \cdot (x_2 - SR_{soil}) & , SR_{soil} \in (0, 3 \times 10^4] \end{cases} \quad (4.12)$$

where, $b=0.2$, $a=1.0$, $x_2=3 \times 10^4$, and $x_1=0.0$ are constant parameters. The parameters a and b are unitless fractions. The parameters x_2 and x_1 are in unit KJ (solar radiation, daily). This function decreases microbial decomposition from a maximum when $SR_{soil} = 0$ to a minimum $F_{Metabolic,o}^C$ when SR_{soil} is high (Adair et al. 2015). The respiration rate of the flow is between 0.4 and 0.55.

The rest C in the flow still goes into the surface SOM1. The associated N flow is still determined using the DayCent strategies summarized by Bonan et al. (2013).

In DayCent-UV, the turnover rates of surface active and the surface slow are increased by higher solar radiation (as a microbial inhibitor) (Adair et al. 2015). The mechanism is implemented via the microbial turnover rate increaser (mti). mti is a piecewise linear function as a function of the soil surface solar radiation (SR_{soil}):

$$mti = \begin{cases} 1.0 & , SR_{soil} \leq 0 \\ 5.0 & , SR_{soil} > 3 \times 10^4 \\ c + \frac{d-c}{x_4 - x_3} \times (SR_{soil} - x_3) & , SR_{soil} \in (0, 3 \times 10^4] \end{cases} \quad (4.13)$$

where, $c=1.0$, $d=5.0$, $x_4=3 \times 10^4$, and $x_3=0.0$ are constant parameters. The parameters c and d are unitless fractions. The parameters x_4 and x_3 are in unit KJ (solar radiation, daily). This function increases microbial turnover and N release from a minimum at $SR_{soil} = 0$ to a maximum at high SR_{soil} (Adair et al. 2015).

Literature Cited

- Adair E C, Parton W J, King J Y, Brandt L, Harmon M E (2015), Accounting for photodegradation dramatically improves prediction of carbon and nitrogen losses in arid systems. (In prep.)
- Bonan G B, Hartman M D, Parton W J, Wieder W R (2013), Evaluating litter decomposition in earth system models with long-term litterbag experiments: an example using the Community Land Model version 4 (CLM4). *Global Change Biology*, 19: 957–974. doi: 10.1111/gcb.12031

APPENDIX 4.C ESTIMATION OF (CANOPY LEVEL) SOLAR RADIATION FROM DAILY MAXIMUM AND MINIMUM TEMPERATURES

The solar radiation is an important weather parameter in DayCent. In the water-flow submodel, solar radiation is used in calculation of snow melt. In the photosynthesis submodel, total solar radiation is used to estimate the photosynthetically active radiation (PAR) and PAR is used as a light effect to calculate the potential photosynthesis. The potential photosynthesis is a function of AMAX, four AMAX scalars, and effects of temperature, vapor pressure deficit, and light. In the production submodel, solar radiation is used in calculation of potential total production of crops or trees. In the decomposition submodel (of the UV version of Daycent), solar radiation induces direct CO₂ loss from surface litter and impacts the sizes and flows of surface pools.

DayCent adopts the solar radiation estimation codes from the SIPNET model. The algorithm is a reformulation of the Bristow-Campbell model, which uses daily temperature, humidity, and precipitation in daily solar radiation estimation (Thornton and Running, 1999; Bristow and Campbell, 1984).

The daily total solar radiation on canopy top (*srad*) is the sum of the daily diffuse horizontal solar radiation (*srad2*), the daily direct solar radiation (*srad1*), and the snow pack influence factor (*snowc*):

$$srad = srad2 + srad1 + snowc \quad (4.14)$$

where, *snowc* is a linear function of snow water and its value is within [0, 100]; *srad2* and *srad1* are calculated by

$$\begin{aligned}
srad2 &= SR_{pot}^{Horiz} \times T_{t,max} \times T_{f,max} \times P_{dif} \times f_{sky} \\
srad1 &= SR_{pot}^{slp} \times T_{t,max} \times T_{f,max} \times (1 - P_{dif})
\end{aligned}
\tag{4.15}$$

where, $T_{t,max}$ is the daily maximum transmittance corrected for vapor pressure; $T_{f,max}$ is the correction factor of $T_{t,max}$ as a function of daily temperature range (ΔT) and precipitation. P_{dif} is the fraction of the diffuse component in total solar radiation. f_{sky} is the parameter that adjusts the diffuse component when the site surface is not horizontal. For a horizontal site, $f_{sky} = 1$. SR_{pot}^{Horiz} is the daily potential solar radiation on the horizontal surface at the top of atmosphere. SR_{pot}^{slp} is the daily potential solar radiation on the tilted surface at the top of atmosphere.

The three daily variables $T_{t,max}$, SR_{pot}^{Horiz} and SR_{pot}^{slp} are calculated using accumulated variables at every time step (600 seconds) during daytime.

At each time step ii , three important instantaneous variables are calculated:

- (a) the instantaneous total solar radiation on the horizontal surface at the top of atmosphere ($SR_{ii}^{Horiz,TOA}$) is calculated from solar constant (1368 W/m^2), day of year, and solar zenith angle;
- (b) the instantaneous total solar radiation on the tilted surface at the top of atmosphere ($SR_{ii}^{Slp,TOA}$) is calculated from solar constant, day of year, solar zenith angle, slope, and aspect; and
- (c) the instantaneous maximum transmittance at the site (T_{ii}) is 0.87 corrected by site elevation and solar zenith angle; the instantaneous maximum solar radiation reaching the horizontal surface at the top of canopy ($SR_{ii}^{Horiz,GRD,pot}$) are the product of $SR_{ii}^{Horiz,TOA}$ and T_{ii} .

The accumulated $SR_{ii}^{Horiz,TOA}$, $SR_{ii}^{Slp,TOA}$, and $SR_{ii}^{Horiz,GRD,pot}$ in the day are $SR^{Horiz,TOA}$, $SR^{Slp,TOA}$, and $SR^{Horiz,GRD,pot}$, respectively.

The daily maximum transmittance $T_{t,max}$ is calculated by

$$T_{t,\max} = SR^{Horiz,GRD,pot} / SR^{Horiz,TOA} \quad (4.16)$$

The daily potential solar radiation on the horizontal surface at the top of atmosphere (SR_{pot}^{Horiz}) is calculated by

$$SR_{pot}^{Horiz} = SR^{Horiz,TOA} / dayl \quad (4.17)$$

where, *dayl* is the daytime length of the given day in seconds.

The daily potential solar radiation on the tilted surface at the top of atmosphere (SR_{pot}^{slp}) is calculated by

$$SR_{pot}^{slp} = SR^{Slp,TOA} / dayl \quad (4.18)$$

Literature Cited

Bristow K L, Campbell G S (1984), On the relationship between incoming solar radiation and daily maximum and minimum temperature. *Agricultural and Forest Meteorology*, 31(2): 159-166. doi: 10.1016/0168-1923(84)90017-0

Thornton P E, Running S W (1999), An improved algorithm for estimating incident daily solar radiation from measurements of temperature, humidity, and precipitation. *Agricultural and Forest Meteorology*, 93(4): 211-228. doi: 10.1016/S0168-1923(98)00126-9

APPENDIX 4.D LIST OF IMPORTANT CHANGES TO DAYCENT INPUT PARAMETERS

(CPER)

category	Var. Name	Default Value	Adjusted Value	Meaning
Solar Radiation	[sitepar.in]			
	sradadj(1)	0.42	1.39	Solar radiation monthly adjustment coefficients (January)
	sradadj(2)	0.5	1.33	Solar radiation monthly adjustment coefficients (February)
	sradadj(3)	0.53	1.24	Solar radiation monthly adjustment coefficients (March)
	sradadj(4)	0.57	1.22	Solar radiation monthly adjustment coefficients (April)
	sradadj(5)	0.62	1.25	Solar radiation monthly adjustment coefficients (May)
	sradadj(6)	0.69	1.28	Solar radiation monthly adjustment coefficients (June)
	sradadj(7)	0.71	1.28	Solar radiation monthly adjustment coefficients (July)
	sradadj(8)	0.66	1.27	Solar radiation monthly adjustment coefficients (August)
	sradadj(9)	0.58	1.28	Solar radiation monthly adjustment coefficients (September)
	sradadj(10)	0.52	1.31	Solar radiation monthly adjustment coefficients (October)
	sradadj(11)	0.46	1.38	Solar radiation monthly adjustment coefficients (November)
sradadj(12)	0.45	1.39	Solar radiation monthly adjustment coefficients (December)	
soil water content	[soils.in]			
	Col. 4 L1	0.25	0.16	Field Capacity for soil layer 1 (0-2 cm)
	Col. 4 L2	0.25	0.17	Field Capacity for soil layer 2 (2-5 cm)
	Col. 4 L3	0.21	0.18	Field Capacity for soil layer 3 (5-10 cm)
	Col. 4 L4	0.21	0.18	Field Capacity for soil layer 4 (10-20 cm)
	Col. 4 L5	0.21	0.16	Field Capacity for soil layer 5 (20-30 cm)
	Col. 4 L6	0.21	0.16	Field Capacity for soil layer 6 (30-45 cm)
	Col. 4 L7	0.21	0.16	Field Capacity for soil layer 7 (45-60 cm)
	Col. 4 L8	0.21	0.16	Field Capacity for soil layer 8 (60-75 cm)
	Col. 4 L9	0.21	0.16	Field Capacity for soil layer 9 (75-90 cm)
	Col. 4 L10	0.21	0.16	Field Capacity for soil layer 10 (90-105 cm)
	Col. 4 L11	0.21	0.16	Field Capacity for soil layer 11 (105-120 cm)
	Col. 5 L1	0.08	0.04	Wilting point for soil layer 1 (0-2 cm)
	Col. 5 L2	0.08	0.04	Wilting point for soil layer 2 (2-5 cm)
	Col. 5 L3	0.06	0.04	Wilting point for soil layer 3 (5-10 cm)
	Col. 5 L4	0.06	0.04	Wilting point for soil layer 4 (10-20 cm)
	Col. 5 L5	0.06	0.04	Wilting point for soil layer 5 (20-30 cm)
	Col. 5 L6	0.05	0.04	Wilting point for soil layer 6 (30-45 cm)
	Col. 5 L7	0.07	0.04	Wilting point for soil layer 7 (45-60 cm)
	Col. 5 L8	0.05	0.04	Wilting point for soil layer 8 (60-75 cm)
	Col. 5 L9	0.05	0.04	Wilting point for soil layer 9 (75-90 cm)
	Col. 5 L10	0.05	0.04	Wilting point for soil layer 10 (90-105 cm)
	Col. 5 L11	0.05	0.04	Wilting point for soil layer 11 (105-120 cm)
	Col. 7 L1	0.08	0.01	Fraction of roots in soil layer 1 (0-2 cm)
	Col. 7 L2	0.12	0.02	Fraction of roots in soil layer 2 (2-5 cm)
	Col. 7 L3	0.23	0.10	Fraction of roots in soil layer 3 (5-10 cm)
	Col. 7 L4	0.23	0.23	Fraction of roots in soil layer 4 (10-20 cm)
	Col. 7 L5	0.24	0.24	Fraction of roots in soil layer 5 (20-30 cm)
	Col. 7 L6	0.17	0.17	Fraction of roots in soil layer 6 (30-45 cm)
	Col. 7 L7	0.06	0.06	Fraction of roots in soil layer 7 (45-60 cm)
	Col. 7 L8	0.05	0.05	Fraction of roots in soil layer 8 (60-75 cm)
	Col. 7 L9	0.05	0.05	Fraction of roots in soil layer 9 (75-90 cm)
	Col. 7 L10	0.03	0.03	Fraction of roots in soil layer 10 (90-105 cm)
Col. 7 L11	0.02	0.02	Fraction of roots in soil layer 11 (105-120 cm)	
Col. 11 L1	0.06	0.03	Minimum volumetric soil water content for soil layer 1 (0-2 cm)	

	Col. 11 L2	0.04	0.02	Minimum volumetric soil water content for soil layer 2 (2-5 cm)
	Col. 11 L3	0.03	0.02	Minimum volumetric soil water content for soil layer 3 (5-10 cm)
	Col. 11 L4	0.03	0.01	Minimum volumetric soil water content for soil layer 4 (10-20 cm)
	Col. 11 L5	0.00	0.00	Minimum volumetric soil water content for soil layer 5 (20-30 cm)
	Col. 11 L6	0.00	0.00	Minimum volumetric soil water content for soil layer 6 (30-45 cm)
	Col. 11 L7	0.00	0.00	Minimum volumetric soil water content for soil layer 7 (45-60 cm)
	Col. 11 L8	0.00	0.00	Minimum volumetric soil water content for soil layer 8 (60-75 cm)
	Col. 11 L9	0.00	0.00	Minimum volumetric soil water content for soil layer 9 (75-90 cm)
	Col. 11 L10	0.00	0.00	Minimum volumetric soil water content for soil layer 10 (90-105 cm)
	Col. 11 L11	0.00	0.00	Minimum volumetric soil water content for soil layer 11 (105-120 cm)
	[fix.100]			
	tmelt(2)	0.0026	0.0300	ratio between degrees above the minimum and cm of snow that will melt
AET	[sitepar.in]			
	dmpflux	8e-6	1e-6	damping factor for soil water flux
	hours_rain	10	20	duration [hours] of each rain event
	[fix.100]			
	fwloss(4)	0.7	0.8	scaling factor for potential evapotranspiration
Live Biomass	[graz.100]			
	flgrem	0.10	0.05	fraction of live shoots removed by grazing
	[crop.100]			
	curgdys	120.0	70.0	number of days unrestricted growth in a grass/crop system
	clsgres	0.5	0.8	late season growth restriction factor
	fsdeth(1)	0.20	0.04	maximum monthly shoot death rate at very dry soil conditions
	fsdeth(2)	0.70	0.99	fraction of shoots which die during senescence month
	prdx(1)	1.0	0.3	coefficient for calculating potential production [NPP] as a function of solar radiation at canopy level
	wscoeff(1,1)	0.45	0.60	the relative water content at which the water stress factor for growth equals 0.5
	wscoeff(1,2)	9.0	25.0	the slope term for water stress function for growth
	claypg	6	7	number of soil layers used to determine water and mineral nutrients that are available for crop/grass growth
	[sgs.100]			
	epnfa(1)	0.05	0.45	the intercept term for determining the effect of annual precipitation on atmospheric N fixation
	epnfa(2)	0.0048	0.0060	the slope term for determining the effect of annual precipitation on atmospheric N fixation
	[cult.sch]			
cultra(1)	0.99	0.64	fraction of aboveground live transferred to standing dead	
NEE	[crop.100]			
	amax(1)	50.0	20.0	maximum photosynthesis rate without any stress (nmol CO ₂ / g leaf/ sec)
	amaxscalar2(1)	1.0	1.4	the 2 nd amax multiplier
	amaxscalar3(1)	1.0	1.0	the 3 rd amax multiplier
	amaxscalar4(1)	1.0	0.0	the 4 th amax multiplier
	growthdays2(1)	25	60	number of days after germination to start using amaxscalar2(1)
	growthdays3(1)	65	150	number of days after germination to start using amaxscalar3(1)
	growthdays4(1)	105	175	number of days after germination to start using amaxscalar4(1)
	basefolrespfrac(1)	0.1	0.6	basal foliage respiration rate, as percentage of maximum net photosynthesis rate
	ckmrspmx(1)	0.1524	0.0762	maximum fraction of aboveground live C that goes to maintenance respiration for crops
	ckmrspmx(2)	0.2320	0.8000	maximum fraction of juvenile live fine root C that goes to maintenance respiration for crops
	ckmrspmx(3)	0.0728	0.3000	maximum fraction of mature live fine root C that goes to maintenance respiration for crops
ps2mrsp(1)	0.50	0.25	fraction of photosynthesis that goes to maintenance respiration	
Others	[fix.100]			
	varat21(1,1)	15.0	20.0	maximum C/N ratio for material entering surface SOM2

	pmco2(1)	0.55	0.40	fraction of C flow from surface metabolic during decomposition that is lost as CO ₂
	pmco2(2)	0.55	0.40	fraction of C flow from soil metabolic during decomposition that is lost as CO ₂
	ps1co2(1)	0.45	0.70	the multiplier regulating the amount of CO ₂ loss when surface structural decomposes to surface som1
	ps1co2(2)	0.55	0.60	the multiplier regulating the amount of CO ₂ loss when soil structural decomposes to soil som1
	[crop.100]			
	cfrtcn(1)	0.7	0.6	maximum fraction of C allocated to roots under maximum nutrient stress
	cfrtcn(2)	0.4	0.3	minimum fraction of C allocated to roots under no nutrient stress
	cfrtcw(1)	0.7	0.6	maximum fraction of C allocated to roots under maximum water stress
	cfrtcw(2)	0.4	0.3	minimum fraction of C allocated to roots under no water stress
	rdrj	0.7	0.3	maximum juvenile fine root death rate at very dry soil conditions
	rdrm	0.056	0.090	maximum mature fine root death rate at very dry soil conditions
	rdsrfc	0.14	0.00	the fraction of dead fine roots transferred into the surface litter pools
	cmix	0.25	3.00	rate of mixing surface SOM2 and soil SOM2

APPENDIX 4.E PARAMETER LIST OF SHORTGRASS STEPPE (CPER) IN CROP.100

Name	Value	Name	Value	Name	Value	Name	Value
PRDX(1)	0.3	PRBMN(2,2)	0	DEL13C	27	WSCOEFF(1,2)	25
PPDF(1)	27	PRBMN(3,2)	0	CO2IPR	1.1	PS2MRSP(1)	0.25
PPDF(2)	45	PRBMX(1,1)	50	CO2ITR	0.65	SFAVAIL(1)	0.15
PPDF(3)	1	PRBMX(2,1)	420	CO2ICE(1,1,1)	1.3	AMAX(1)	20
PPDF(4)	2.5	PRBMX(3,1)	420	CO2ICE(1,1,2)	1	AMAXFRAC(1)	0.75
BIOFLG	1	PRBMX(1,2)	0	CO2ICE(1,1,3)	1	AMAXSCALAR1(1)	1
BIOK5	60	PRBMX(2,2)	0	CO2ICE(1,2,1)	1.3	AMAXSCALAR2(1)	1.4
PLTMRF	1	PRBMX(3,2)	0	CO2ICE(1,2,2)	1	AMAXSCALAR3(1)	1
FULCAN	100	FLIGNI(1,1)	0.02	CO2ICE(1,2,3)	1	AMAXSCALAR4(1)	0
FRTCINDX	1	FLIGNI(2,1)	0.0012	CO2IRS	1	ATTENUATION(1)	0.57999
FRTC(1)	0.7	FLIGNI(1,2)	0.26	CKMRSPMX(1)	0.07621	BASEFOLRESPFRAC(1)	0.6
FRTC(2)	0.3	FLIGNI(2,2)	-0.0015	CKMRSPMX(2)	0.8	CFRACLEAF(1)	0.45
FRTC(3)	90	FLIGNI(1,3)	0.26	CKMRSPMX(3)	0.3	DVPDEXP(1)	-0.48
FRTC(4)	0.2	FLIGNI(2,3)	-0.0015	CMRSPNPP(1)	0	DVPDSLOPE(1)	2.457
FRTC(5)	0.1	HIMAX	0	CMRSPNPP(2)	0	GROWTHDAYS1(1)	1
CFRTC(1)	0.6	HIWSF	0	CMRSPNPP(3)	2	GROWTHDAYS2(1)	60
CFRTC(2)	0.3	HIMON(1)	0	CMRSPNPP(4)	0.25	GROWTHDAYS3(1)	150
CFRTCW(1)	0.6	HIMON(2)	0	CMRSPNPP(5)	6	GROWTHDAYS4(1)	175
CFRTCW(2)	0.3	EFRGRN(1)	0.5	CMRSPNPP(6)	4	HALFSATPAR(1)	17.28
BIOMAX	200	EFRGRN(2)	0.5	CGRESP(1)	0.23	LEAFCSJWT(1)	270
PRAMN(1,1)	20	EFRGRN(3)	0.5	CGRESP(2)	0.23	PSNTMIN(1)	4
PRAMN(2,1)	390	VLOSSP	0.04	CGRESP(3)	0.23	PSNTOPT(1)	24
PRAMN(3,1)	340	FSDETH(1)	0.04	NO3PREF(1)	0.5		
PRAMN(1,2)	60	FSDETH(2)	0.99	CLAYPG	7		
PRAMN(2,2)	390	FSDETH(3)	0.2	CMIX	3		
PRAMN(3,2)	340	FSDETH(4)	150	TMPGERM	10		
PRAMX(1,1)	30	FALLRT	0.2	DDBASE	1500		
PRAMX(2,1)	440	RDRJ	0.3	TMPKILL	7		
PRAMX(3,1)	440	RDRM	0.09	BASETEMP(1)	10		
PRAMX(1,2)	80	RDSRFC	0	BASETEMP(2)	30		
PRAMX(2,2)	440	RTDTMP	2	MNDDHRV	100		
PRAMX(3,2)	440	CRPRTF(1)	0.3	MXDDHRV	200		
PRBMN(1,1)	40	CRPRTF(2)	0	CURGDYS	70		
PRBMN(2,1)	390	CRPRTF(3)	0	CLSGRES	0.8		
PRBMN(3,1)	340	MRTFRAC	0.05	CMXTURN	0.12		
PRBMN(1,2)	0	SNFXMX(1)	0	WSCOEFF(1,1)	0.6		

APPENDIX 4.F A BRIEF DESCRIPTION OF THE LOCAL OPTIMIZER USED IN THE OPTIMIZATION

The gradient based non-linear optimizer for this study is provided by Intel Math Kernel Library. It uses the trust-region algorithm and its implementation is based on Intel's internal modification of the algorithm described in Conn et al. (2000).

The trust region algorithm (Conn et al. 2000) uses an iterative optimization strategy. In each iteration k , the algorithm defines the trust region that covers all points within the radius of Δ_k from the current trial point x_k . Then, it constructs a quadratic model function m_k to simulate the objective function centered at x_k :

$$m_k(p) = f(x_k) + \nabla f(x_k)^T p + \frac{1}{2} p^T B_k p \quad (4.19)$$

where, f is the objective function, ∇f is the gradient of f , B_k is some symmetric matrix and p is a step from x_k . Then, the algorithm solves the following sub-problem of m_k to get the p_k that reduces the objective function most within the current trust region radius Δ_k :

$$\min_{p \in \mathbb{R}^n} m_k(p) = f(x_k) + \nabla f(x_k)^T p + \frac{1}{2} p^T B_k p \quad s.t. \|p\| \leq \Delta_k \quad (4.20)$$

If Δ_k is small enough, m_k always represents the objective function well. In such case, the solution of Eq. (4.20), p_k , is guaranteed to be of high quality and moving along it leads to a better trial point. But p_k is small at each iteration, it will take many iterations to get to the optimum. If Δ_k is too large, m_k may represent the objective function poorly and there is no guarantee that the solution of Eq. (4.20), p_k , leads to a better trial point. Therefore, it is

necessary to evaluate the quality of the model m_k at its solution p_k at each iteration. The algorithm uses the ratio (ρ_k) to determine the quality of m_k at iteration k :

$$\rho_k = \frac{f(x_k) - f(x_k + p_k)}{m_k(0) - m_k(p_k)} \quad (4.21)$$

A value of ρ_k close to 1 (e.g. $\rho_k > 0.75$) means that the current model m_k represents the objective function f around x_k well. It suggests Δ_{k+1} should be expanded (e.g. $\Delta_{k+1} = 2\Delta_k$) to allow a more efficient optimization and the trial point should be updated ($x_{k+1} = x_k + p_k$). On the other hand, a value of ρ_k far away from 1 (e.g. $\rho_k \leq 0.25$) means that m_k does not agree with f well. It suggests Δ_{k+1} should be reduced to get a more reliable step (e.g. $\Delta_{k+1} = 1/2\Delta_k$) and the trial point should not be updated ($x_{k+1} = x_k$). An intermediate value of ρ_k (e.g. $0.25 < \rho_k \leq 0.75$) means that the performance of m_k is merely acceptable. It suggests Δ_{k+1} keeps the same as Δ_k and the trial point should be updated ($x_{k+1} = x_k + p_k$).

Nocedal and Wright (2006) gives four methods/strategies for solving Eq. (4.20). Three of them, the dogleg method (Powell, 1970), the two-dimensional subspace minimization (Byrd et al., 1988), and the Steihaug strategy (Steihaug, 1983), provide approximate solutions. The last one, Moré and Sorensen (1983), finds a “nearly exact” solution. The approximate solutions are less costly to be found since they require fewer matrix factorizations than the exact solution. They all achieve reduction no less than the Cauchy point, which is a point between x_k and the edge of the current trust region along the opposite of the current gradient direction $-\nabla f(x_k)$.

There is a section in Chapter 10 in Conn et al. (2000) that discusses the extension of the standard trust region to handle problems of the objective function with dynamic accuracy. It is not clear whether Intel’s implementation has considered this extension in its current version.

However, the trust region algorithm is relatively robust even if the objective function contains noise (Carter, 1993).

If there are discrete variables to be optimized, it is not guaranteed that treating them like real variables and rounding the solutions to the nearest integers gives the optimal result. This kind of problem (e.g. an integer programming problem) should be solved with a certain discrete optimization algorithm (Nocedal and Wright, 2006).

In general, the problem the Intel non-linear optimizer solves is stated as follows¹²:

$$\min_{x \in R^n} \|Q(x)\|_2^2 = \min_{x \in R^n} \|o - q(x)\|_2^2 \quad (4.22)$$

Where, $\|Q(x)\|_2^2$ is the objective function [f in Eq. (4.19)]; $q: R^n \rightarrow R^m$ represents the model (e.g. the DayCent-UV model); m is the dimension of the model outputs and n is the number of model variables, $m \geq n$; $o \in R^m$ are the observed values at x ; $x \in R^n$ are the model variables and $l_i \leq x_i \leq u_i, i = 1, \dots, n$.

The solver stops (and returns the current trial point) when one of the following criteria is met¹³: (1) The allowed maximum number of iterations has been reached; (2) the trust region Δ is smaller than a given threshold; (3) $\|Q(x)\|_2$ is smaller than a given threshold; (4) Jacobi matrix ($J(x)$) is singular; (5) the step p_k is smaller than a given threshold; or (6)

$\|Q(x)\|_2 - \|Q(x) - J(x)p_k\|_2$ is smaller than a given threshold. Note that Jacobi matrix, $J(x)$, is an m by n matrix and contains the gradients of each $Q(x)$ at x .

¹² <https://software.intel.com/en-us/node/522089#4EA75446-AA99-423C-B497-00D86E1CDEFE>

¹³ <https://software.intel.com/en-us/node/522092#2C032A38-A85C-4468-86F4-BA2B486D02D6>

The solver only gives local optimal solution; however, if the initial point is close to the global optimum, its local optimal solution is very likely to be near the global optimum.

Literature Cited

- Byrd R H, Schnabel R B, Schultz G A (1988), Approximate solution of the trust regions problem by minimization over two-dimensional subspaces. *Mathematical Programming*, 40(3): 247–263
- Carter R G (1993), Numerical experience with a class of algorithms for nonlinear optimization using inexact function and gradient information. *SIAM Journal on Scientific and Statistical Computing*, 14(2): 368–388
- Conn A R, Gould N I M, Toint Ph L (2000), *Trust-Region Methods*. SIAM/MPS Series on Optimization, SIAM, Philadelphia
- Moré J J, Sorensen D C (1983), Computing a trust region step. *SIAM Journal on Scientific and Statistical Computing*, 4(3): 553–572
- Nocedal J, Wright S J (2006), *Numerical optimization*. 2nd ed. New York: Springer
- Powell M J D (1970), A Hybrid Method for Nonlinear Equations (Chap 6) and A Fortran Subroutine for Solving systems of Nonlinear Algebraic Equations (Chap 7). In P Rabinowitz (Ed.), *Numerical Methods for Nonlinear Algebraic Equations* (pp. 87–161). London: Gordon and Breach Science Publishers
- Steihaug T (1983), The conjugate gradient method and trust regions in large scale optimization. *SIAM Journal on Numerical Analysis*, 20: 626–637

CONCLUSIONS

Incorporating a solar UV decomposition mechanism into biogeochemical models is important for exploring the model's ecological impacts in semi-arid ecosystems. Accurate ground solar radiation is critical for retrieving atmospheric properties, validating satellite products and simulating ecosystem processes. The dissertation is separated into two parts, both focused on the improvement of the performance of the DayCent model.

The primary objective of the first part is to improve the accuracy and reliability of the current main calibration method for (UV) Multi-Filter Rotating Shadowband Radiometer (MFRSR) observations.

The USDA UVMRP has adopted the in-situ calibration method due to the high cost of providing continuous laboratory lamp calibrations. In reviewing the literature regarding in-situ calibration methods of MFRSR measurements as described in chapter 1, I found that (1) In-situ calibration methods requiring collocated measurements in addition to MFRSR voltages and solar geometries (such as aerosol optical depth or total-sky-imaging) are not applicable to most sites for the U.S. Department of Agriculture UV-B Monitoring and Research Program (the UV-B program); (2) the strategy of limiting the cloud screening algorithm to examination of the voltages measured in short local time intervals is the main reason for the poor performance of the original algorithm and no alternative algorithms are applicable for voltage data; and (3) Generally, in-situ calibration methods rely on stability assumptions of some atmospheric properties (such as total optical depth, aerosol extinction efficiency, and precipitable water vapor) over time, which are not always valid. Both points (2) and (3) result in dispersed

responsivity coefficients with large time gaps and lower quality of radiation and derived products.

A new cloud screening algorithm for narrowband direct-beam UV MFRSR measurements is developed in chapter 2. The mathematical basis of this algorithm is Beer's law. Voltage measurements are reorganized to a converted coordinate system that emphasizes the relative magnitude of the measurements' total optical depth (TOD). Using a special weighting design, we are able to compare any time target measurement' TOD with the weighted average TOD of any other pair points in any time or airmass range on the day when the calibration coefficient (V_{LO}) for the day is unknown. Through iteration of this process, cloudy points are gradually excluded and the cloud-free points set is eventually determined. The performance of the new cloud screening method was verified with the model simulation. The Langley voltage offsets (V_{LO} s) obtained from cloud-free points identified by the new cloud screening were compared to those obtained using the original Langley program. The newly identified cloud-free points showed nearly same aerosol optical depth as those in the extended clear-sky periods in the testing case, suggesting the points in the transitional region and short intervals were also clear-sky points. The results at the relatively clear site at Mauna Loa Observatory, HI showed that values of V_{LO} s from partly cloudy days were not biased in comparison to those from sunny days. The results at the cloudy site at Homestead, FL showed that 56% more V_{LO} s were identified with the new cloud screening method than with the original Langley program. This is an especially valuable result as calibration at some sites is challenging for extended cloudy periods especially in wintertime. All these results demonstrated that the new cloud screening algorithm is more capable of screening cloudy points while retaining clear-sky points than the original method which has been used over the entire history of the UVMRP.

In chapter 3, a new two-stage reference spectral channel calibration method is developed for pairs of collocated UV-MFRSR and MFRSR instruments. The new method is improved from the original Langley method. Its main advantage is that the assumption of participating points for Langley regression having stable TOD values is ensured without additional measurements. In stage 1, special channels where aerosol is the only contributor to TOD variation (e.g. 368-nm channel) were selected. Next, a lookup table of the direct normal and diffuse horizontal ratio with respect to aerosol optical depth and solar zenith angle at the special channel created using the radiative transfer model (MODTRAN). The quality of V_{LO} s was established by giving lower weights to those generated from points with monotonic variation in aerosol optical depth (AOD). In stage 2, the most stable points in 1 or 2 reference channel(s) were selected and Langley regression was applied on the same time points to generate V_{LO} s in the adjacent un-calibrated channel(s). The test of this method on the UV-B program site at Homestead, Florida (FL02) showed that (1) The long-term trend of the original Langley V_{LO} s is impacted by the monotonic changing AOD at the 368nm channel; (2) more clustered and abundant V_{LO} s at all channels are generated compared using the new Langley method; and (3) the new method showed over 10% mean difference of V_{LO} s compared to the original Langley method at 300-nm and 305-nm channels.

In the first part, I identified the two major problems of the current calibration method for (UV-) MFRSR and provided the corresponding solutions. The results showed that the new cloud screening algorithm and the new calibration method together improved the accuracy and reduced the uncertainty of calibration. These findings suggest that the new calibration method should be validated at more sites that feature collocated radiation, aerosol, and ozone measurements.

The primary objective of the second part (chapter 4) is to modify and validate the UV decomposition module in the DayCent biogeochemical model and to explore the potential long-term impacts of UV decomposition on ecosystem processes in (semi-)arid ecosystems, such as plant production, carbon and nitrogen storage in litter and soil, and trace gas emissions.

First, the DayCent-UV model parameters were adjusted to match ecosystem parameters at a calibration site. Second, the model was configured to simulate the LIDET decomposition experiment in 1990s for six common litter types at the three semi-arid sites. A subset of the photodegradation related parameters were optimized for each species individually and across species by the global optimization algorithm that combined scatter search and nonlinear trust region optimization algorithms. Third, the relationship between photodegradation and initial litter chemistry (especially lignin content) was explored and the pattern found between litter's initial lignin content and its potential photodecomposition rate was implemented in the DayCent-UV model. The results showed that the calibrated DayCent-UV model fitted the major patterns in observed first 20-cm soil water content, aboveground live biomass, and actual evapotranspiration (R^2 between 0.44 and 0.50) but missed some CO_2 spikes after heavy rain events in the observed net ecosystem exchange ($R^2 = 0.23$). Generally, the optimized DayCent-UV model fitted the observed remaining carbon vs time pattern well for both individual species and across species averages at three (semi-)arid LIDET sites and predicted the observed general pattern of nitrogen release with time. However, the model showed larger discrepancy on remaining nitrogen vs time for individual species, suggesting that some mechanisms of photodegradation on nitrogen dynamics may be missing. The slight overestimation of carbon release in the early stage (i.e. the first few years) and the underestimation in the later stage suggested that the cumulative effect of solar exposure should be considered. The DayCent-UV

model fitted the LIDET remaining carbon and nitrogen observation much better than the DayCent-Photosyn model (no UV decomposition module) especially in the later stage. The negative relationship between litter's initial lignin fraction and the individually optimized photodecay rate suggested that cellulose rather than lignin may be the chemical compound that is responsible for UV degradation. The DayCent-UV equilibrium model runs showed that UV decomposition increased aboveground and belowground plant production, surface net nitrogen mineralization, and surface litter nitrogen pool, while decreased surface litter carbon, soil net nitrogen mineralization and mineral soil carbon and nitrogen. In addition, UV decomposition showed minimal impacts (i.e. less than 1% change) on trace gases emission and biotic decomposition rates.

In the future, the parameterization of surface UV radiation from total solar radiation as well as other meteorological data should be incorporated into the DayCent-UV model. The effect of cumulative UV radiation exposure on photodegradation should be implemented in DayCent-UV model.